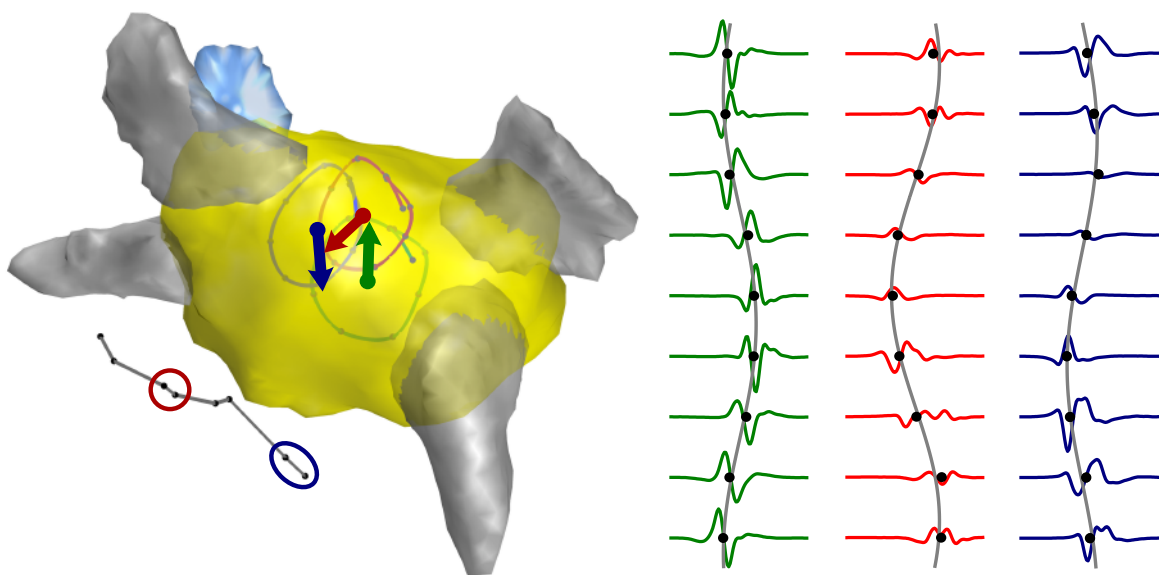


Frank Michael Weber

Personalizing Simulations of the Human Atria

Intracardiac Measurements, Tissue Conductivities, and Cellular Electrophysiology



Frank Michael Weber

Personalizing Simulations of the Human Atria
Intracardiac Measurements, Tissue Conductivities,
and Cellular Electrophysiology

Vol. 12

Karlsruhe Transactions on Biomedical Engineering

Editor:

Karlsruhe Institute of Technology

Institute of Biomedical Engineering

Eine Übersicht über alle bisher in dieser Schriftenreihe erschienene Bände finden Sie am Ende des Buchs.

Personalizing Simulations of the Human Atria

**Intracardiac Measurements, Tissue
Conductivities, and Cellular Electrophysiology**

by
Frank Michael Weber

Dissertation, Karlsruher Institut für Technologie
Fakultät für Elektrotechnik und Informationstechnik, 2011

Impressum

Karlsruher Institut für Technologie (KIT)
KIT Scientific Publishing
Straße am Forum 2
D-76131 Karlsruhe
www.ksp.kit.edu

KIT – Universität des Landes Baden-Württemberg und nationales
Forschungszentrum in der Helmholtz-Gemeinschaft



Diese Veröffentlichung ist im Internet unter folgender Creative Commons-Lizenz
publiziert: <http://creativecommons.org/licenses/by-nc-nd/3.0/de/>

KIT Scientific Publishing 2011
Print on Demand

ISSN: 1864-5933
ISBN: 978-3-86644-646-5

Personalizing Simulations of the Human Atria: Intracardiac Measurements, Tissue Conductivities, and Cellular Electrophysiology

Zur Erlangung des akademischen Grades eines

DOKTOR-INGENIEURS

von der Fakultät für

Elektrotechnik und Informationstechnik

des Karlsruher Instituts für Technologie (KIT)

genehmigte

DISSERTATION

von

Dipl.-Phys. M.Sc. Frank Michael Weber

geb. in Heilbronn

Tag der mündlichen Prüfung: 10. Februar 2011
Referent: Prof. Dr. rer. nat. Olaf Dössel
Korreferent: Prof. Dr. med. Martin Borggrefe

Danksagung

Diese Arbeit wurde zwischen August 2007 und Februar 2011 am Institut für Biomedizinische Technik des Karlsruher Instituts für Technologie (KIT) durchgeführt. Ich möchte mich bei allen Personen herzlich bedanken, die zum Gelingen beigetragen haben.

Ganz besonders möchte ich mich bei Herrn Prof. Dr. rer. nat. Olaf Dössel für die sehr kompetente Betreuung und die Übernahme des Hauptreferats bedanken. Sein großes Interesse an meiner Arbeit, die vielen nützlichen Diskussionen und Anregungen sowie seine Aufgeschlossenheit gegenüber neuen Methoden und Lösungsansätzen habe ich sehr geschätzt.

Herrn Prof. Dr. med. Martin Borggreffe möchte ich ebenfalls für das Interesse an meiner Dissertation und die Übernahme des Korreferats herzlich danken.

Herrn Dr. med. Armin Luik, Herrn Prof. Dr. med. Claus Schmitt sowie dem gesamten EPU-Team des Städtischen Klinikums Karlsruhe danke ich für die exzellente und stets unkomplizierte Zusammenarbeit sowie wertvolle medizinische Anregungen. Diese Arbeit ist erst durch die klinischen Messdaten zu dem geworden, was sie nun ist.

Mein Dank gebührt weiterhin PHILIPS für die Finanzierung eines Großteils des Projektes sowie Herrn Cristian Lorenz und Herrn Hans Barschdorf aus dem PHILIPS Forschungslabor Hamburg für die aufgeschlossene und sehr kompetente Kooperation.

Bedanken möchte ich mich weiterhin bei allen Mitarbeitern des Instituts, die zu dieser Arbeit beigetragen haben. Ich danke Herrn Christopher Schilling für die konstruktive Zusammenarbeit in der Analyse klinischer Messdaten und Korrekturen der Dissertation. Weiterhin geht mein Dank an Herrn David Keller für die gemeinsamen Anstrengungen im Bereich der Gewebeleitfähigkeiten, sowie an Herrn Martin Krüger für die Kollaboration im Bereich der Modellpersonalisierung und Korrekturen der Dissertation. Ich danke außerdem Herrn Dr.-Ing. Gunnar Seemann für die Betreuung in seiner

Arbeitsgruppe Herzmodellierung, viele Anregungen sowie Korrekturen der Dissertation. Allen Kollegen gilt mein besonderer Dank für die sehr angenehme Arbeitsatmosphäre.

Allen Diplomanden, Master-Studenten und Studienarbeitern, die zu dieser Arbeit beigetragen haben, danke ich ebenfalls ganz herzlich, im besonderen Herrn Stefan Bauer, Herrn Martin Bauer und Herrn Michael Burdumy.

Zu guter Letzt möchte ich denen danken, die diese Arbeit erst ermöglicht haben — meinen Eltern für die kontinuierliche Unterstützung und Hilfsbereitschaft während meines Studiums und während der letzten dreieinhalb Jahre, meinen Freunden für viele schöne Momente, sowie Heike für einfach alles.

“A good head and a good heart are always a formidable combination.”
(Nelson Mandela)

Contents

1	Introduction	1
1.1	Motivation	1
1.2	Aims of the Thesis	2
1.3	Structure of the Thesis	2

Part I Basic Foundations

2	Medical Background	7
2.1	Cardiac Anatomy and Physiology	7
2.1.1	General Anatomy	7
2.1.2	General Physiology	8
2.1.3	Measuring Electrical Heart Activity on the Body Surface	10
2.2	Atrial Arrhythmias	11
2.2.1	Specific Atrial Anatomy and Physiology	11
2.2.2	Arrhythmia Types and Underlying Mechanisms	13
2.2.3	Remodeling	14
2.3	Electrophysiological Studies	15
2.3.1	Catheter Types and Mapping Techniques	16
2.3.2	Ablation of Cardiac Arrhythmias	17
3	Simulation and Quantitative Analysis of Cardiac Excitation	19
3.1	Anatomical Models	19
3.1.1	Visible Human Project	19
3.1.2	Individual Segmentation	19
3.2	Electrophysiological Cell Models	20
3.2.1	Hodgkin-Huxley Model	20
3.2.2	Courtemanche et al. Model	21

3.2.3	Minimal Model	22
3.3	Excitation Conduction	25
3.3.1	Bidomain Model	25
3.3.2	Cellular Automaton	26
3.4	Forward Calculation and Tissue Conductivities	27
3.4.1	Forward Problem Formulation	27
3.4.2	Conductivities and Importance of Different Tissue Types	28
3.5	Atrial Simulations	29
3.6	Quantitative Analysis of Electrophysiological Measurements	29

Part II Methods

4	Adaptation of a Minimal Cell Model to Properties of Atrial Tissue	33
4.1	Parameter Analysis	33
4.2	Simulation of Reference Data	35
4.3	Choosing the Parameters for Adaptation	36
4.4	Adaptation Process	37
4.5	2D Patch Simulations	38
5	Influence of Tissue Conductivities on the ECG	39
5.1	Ranking the Influence of Different Tissues	39
5.1.1	Literature Overview of Tissue Conductivities	40
5.1.2	Torso Model and Forward Calculation	40
5.1.3	Ranking by Sensitivity and Uncertainty Analysis	42
5.1.4	Possible Torso Model Simplifications	42
5.2	BSPM Prediction for Varying Conductivities Based on PCA	43
5.2.1	Data Source	44
5.2.2	PCA Analysis	45
5.2.3	Signal Estimation for Arbitrary Conductivities	47
5.2.4	Validation	49
5.2.5	Confidence Intervals	50
6	Quantitative Analysis of Electrophysiological Data	53
6.1	Cosine Fit	53
6.1.1	Activation Time Detection	54
6.1.2	Data Model	55
6.1.3	Patch Validation	55

6.2	RBF Interpolation	58
6.2.1	Mathematical Background	58
6.2.2	Analysis of EP Measurements	61
6.2.3	Validation	62
6.2.4	Detection of Two Colliding Wavefronts	62
6.3	Analysis of Coronary Sinus Signals	63
6.3.1	Linear Correlation Coefficient	63
6.3.2	Linear Fit	64
6.4	Electrogram Simulation and Analysis in a Realistic Atrial Data Set	64
6.5	Analysis of Patient Data	65
6.5.1	Details of Electrophysiological Data	65
6.5.2	Data Analysis	67
6.6	CV Restitution Curves	70
6.6.1	Available Data	70
6.6.2	Local Conduction Velocity	70
6.6.3	Global Conduction Velocity	71
7	Comparison of Simulated and Clinical Data	73
7.1	Creating Anatomical Models	73
7.1.1	Automatic Segmentation Tool	73
7.1.2	Creating Simulation Models	74
7.2	Extracting and Adapting Catheter Positions	75
7.3	Electrogram Simulation and Analysis	76
<hr/>		
Part III Results		
<hr/>		
8	Results: Adaptation of a Minimal Cell Model to Atrial Tissue	79
8.1	Adaptation Results	79
8.1.1	Physiological Case	79
8.1.2	Remodeling Case	80
8.2	Re-entry Simulations in a 2D Patch	81
8.3	Discussion	82
9	Results: Influence of Tissue Conductivities on the ECG	85
9.1	Tissue Ranking	85
9.1.1	Conductivity Values in the Literature	85
9.1.2	Ranking for Atrial Signals	86

9.1.3	Ranking for Ventricular Signals	87
9.1.4	Possible Torso Model Simplifications	88
9.1.5	Discussion	88
9.2	BSPM Prediction for Varying Conductivities Based on PCA	92
9.2.1	Eigenvalue Ratios and Eigenvector Angles	92
9.2.2	Signal Reconstruction	93
9.2.3	Confidence Intervals	93
9.2.4	Discussion	94
10	Results: Quantitative Analysis of Electrophysiological Data	99
10.1	Validation of the Cosine Fit	99
10.2	RBF Interpolation	101
10.2.1	Validation	101
10.2.2	Detection of Two Colliding Wavefronts	101
10.2.3	Detection of Ectopic Foci	102
10.3	Electrogram Simulation and Analysis in a Realistic Atrial Data Set ...	103
10.4	Analysis of Patient Data	103
10.5	CV Restitution Curves	114
10.5.1	Individual Results from Different Patients	115
10.6	Discussion	118
10.6.1	Simulation and Analysis of Intracardiac Electrograms	118
10.6.2	Analysis of Clinical Measurements	120
10.6.3	CV Restitution	121
11	Results: Comparison of Simulated and Clinical Data	125
11.1	Simulation Results	125
11.2	Discussion	129
12	Conclusion	131
	References	135
	List of Publications and Supervised Theses	149

List of Abbreviations

<i>AF</i>	Atrial Fibrillation
<i>AP</i>	Action Potential
<i>APD</i>	Action Potential Duration
<i>AV</i>	Atrio-ventricular
<i>BSPM</i>	Body Surface Potential Map
<i>CA</i>	Cellular Automaton
<i>CC</i>	Correlation Coefficient
<i>CL</i>	Cycle Length
<i>CRN</i>	Courtemanche-Ramirez-Nattel (atrial cell model)
<i>CS</i>	Coronary Sinus
<i>CT</i>	Computed Tomography
<i>CV</i>	Conduction Velocity
<i>ECG</i>	Electrocardiogram
<i>EGM</i>	Electrogram
<i>EP</i>	Electrophysiological
<i>ERP</i>	Effective Refractory Period
<i>GG</i>	Gabriel-Gabriel (tissue conductivity values)
<i>IBI</i>	Inter-Beat-Interval
<i>IVC</i>	Inferior Vena Cava
<i>LA</i>	Left Atrium
<i>LAA</i>	Left Atrial Appendage
<i>LAT</i>	Local Activation Time
<i>LIPV</i>	Left Inferior Pulmonary Vein
<i>LSPV</i>	Left Superior Pulmonary Vein
<i>MM</i>	Minimal Model
<i>NLEO</i>	Non-Linear Energy Operator
<i>NSR</i>	Normal Sinus Rhythm

<i>PC</i>	Principal Component
<i>PCA</i>	Principal Component Analysis
<i>PCL</i>	Pacing Cycle Length
<i>PV</i>	Pulmonary Vein
<i>RA</i>	Right Atrium
<i>RBF</i>	Radial Basis Function
<i>RIPV</i>	Right Inferior Pulmonary Vein
<i>RMSE</i>	Root Mean Square Error
<i>RSPV</i>	Right Superior Pulmonary Vein
<i>SN</i>	Sinus Node
<i>SVC</i>	Superior Vena Cava
<i>TMV</i>	Transmembrane Voltage
<i>VM</i>	Visible Man

Introduction

1.1 Motivation

Atrial fibrillation (AF) is the most common cardiac arrhythmia. An estimated number of 2.2 million people in the United States and 4.5 million people in Europe suffer from AF. The number of patients is strongly increasing, among others due to ageing of the population. Hospital admissions have increased by about 66% during the last 20 years. Furthermore, treatment of AF is extremely expensive. The overall annual societal burden in Europe caused by AF is estimated to around 13.5 billion Euros [1]. Hospitalization causes over 50% of these costs. Other atrial arrhythmias such as atrial flutter are not even included in these statistics. So there is a very strong interest for efficient and successful treatment methods for these atrial arrhythmias.

AF by itself is not lethal, however it severely impairs quality of life and increases the risk of stroke. Therefore, it requires treatment. Besides drug administration, a very common therapeutic approach for atrial arrhythmias is catheter ablation. Selected regions of atrial tissue that are suspected to initiate or maintain the arrhythmia are thereby electrically isolated. This prevents excitation conduction and optimally terminates the arrhythmia. However, catheter ablation is still challenging, and clinically evaluated ablation methods are leading to moderate success rates only. Many patients have to undergo repeated interventions until the arrhythmia is cured.

Personalized computer models have been proposed to assist the physicians in planning and performing interventions. However, model personalization is a difficult task. Many different parameters that influence the results need to be adjusted to the individual patient. In this context, several aspects are of special importance. First, a personalized simulation anatomy is required, i.e. a segmented model of the patient's atria. Second, the description of cellular electrophysiology must be adjusted, that means cell model parameters need to be tuned to represent individual pathologies in the patient. If conclusions based on simulated electrocardiograms are to be made, the

electrical conductivities of different structures within the torso must further be considered, because they show large individual variations and impact on the simulated signals. Finally, measurements from electrophysiological studies should be considered for model personalization, because they are recorded directly at the location of the electric sources and thus possess a very high information content. Apart from that, it is important that the necessary steps be applicable in clinical practice. Otherwise, the required efforts will quickly exceed the possible benefits.

With appropriate methods available, however, personalized computer models could in a long-term perspective be able to assist the cardiologists. This could, for example, be achieved by simulating the outcome of different ablation strategies or providing patient-individual analyses of arrhythmia patterns. Thus, it might further lead to a better understanding of the underlying mechanisms. This way, personalized models could reduce examination times, improve success rates and significantly reduce both the patients' burden and the overall treatment costs.

1.2 Aims of the Thesis

Four major challenges in the personalization of atrial models are addressed in this thesis:

- Investigation of a minimal electrophysiological cell model and an adaptation of its parameters to atrial excitation properties
- A ranking of the influence of electrical conductivities of different organs in the torso on simulated ECGs. Furthermore, an efficient method for predicting changes in ECG that are caused by tissue conductivity variations
- Methods for quantitative analysis of intracardiac electrograms to calculate conduction properties such as propagation direction and conduction velocity from the electrograms
- Comparison of personalized simulations with clinical measurements

1.3 Structure of the Thesis

Part I introduces fundamental clinical and technical backgrounds:

- Chapter 2 gives an overview over the medical background of the heart, atrial arrhythmias, and electrophysiological studies.
- Chapter 3 presents technical foundations about cardiac simulations and the analysis of intracardiac data.

Part II explains the methods that were created and applied in this work:

- Chapter 4 describes the adaptation of the minimal cell model to atrial excitation properties.
- Chapter 5 covers the influence of different organ conductivities in the torso on the simulated body surface potentials. A ranking of the different tissue types is performed, and an efficient prediction of signal changes caused by conductivity variations is developed.
- Chapter 6 discusses the simulation of intracardiac electrograms and introduces analysis techniques for these signals.
- Chapter 7 describes how patient-specific simulation models were created, parameterized, and compared to clinical measurements.

Part III presents the results that were obtained in the course of this thesis:

- Chapter 8 displays the adaptation results of the minimal cell model to atrial excitation properties and shows simulations in 2-D patches.
- Chapter 9 shows the results of the organ ranking and the efficient prediction of signal changes for conductivity variations.
- Chapter 10 demonstrates the applicability of the techniques that analyze intracardiac electrograms and discusses the analysis results from clinical patient data.
- Chapter 11 covers the results of the comparison between patient-specific simulation models and clinical measurements.

Finally, chapter 12 summarizes the thesis and gives an outlook on possible future work.

Part I

Basic Foundations

Medical Background

2.1 Cardiac Anatomy and Physiology

This section gives a general overview over the anatomy and physiology of the heart as well as the measurement of electrocardiograms.

2.1.1 General Anatomy

The heart is a hollow muscular organ located between the lungs and posterior to the sternum. With a size comparable to the human fist, it pumps approximately 8000 liters of blood every day [2]. As shown in Fig. 2.1, the heart comprises four different chambers: the left ventricle pumps blood into the systemic circuit via the aorta, the blood returns to the right atrium (RA) via the superior and inferior vena cava (SVC and IVC), the right ventricle pumps it into the pulmonary circuit, from where it returns to the left atrium (LA) via the pulmonary veins (PVs).

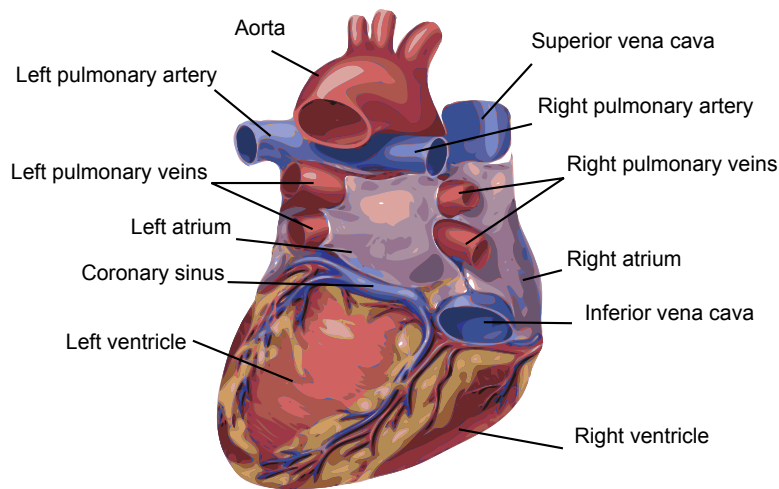


Fig. 2.1. The human heart (posterior view). Adapted from [3, 4].

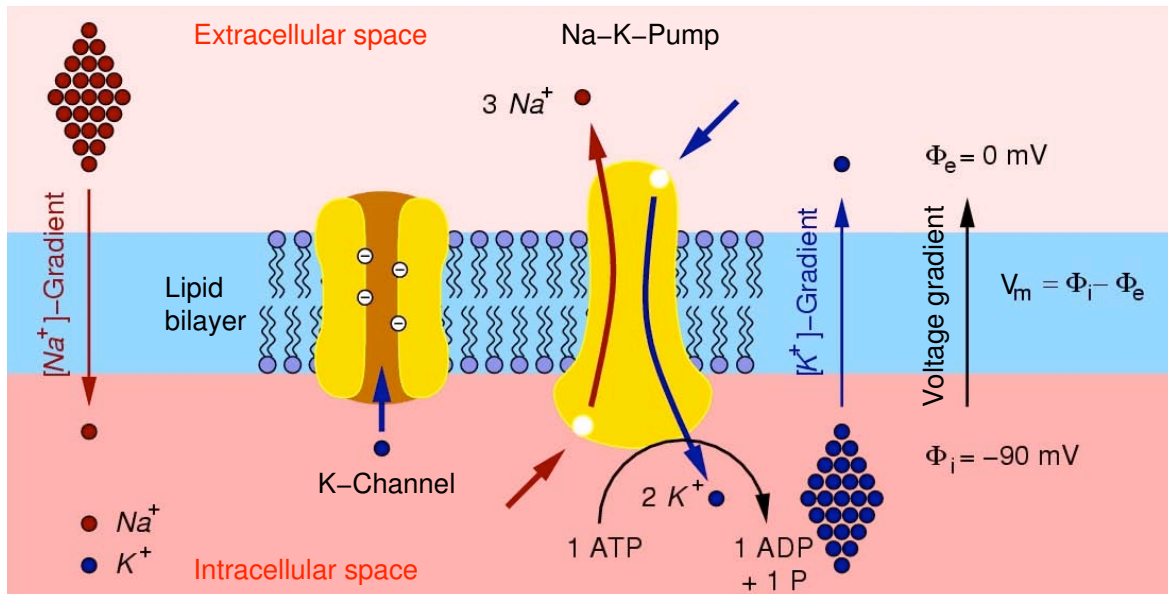


Fig. 2.2. Simplified illustration of the cell membrane. Active transportation mechanisms for sodium and potassium as well as a passive potassium channel are included. The equilibrium potential is maintained at -90 mV. Adopted from [5].

The coronary arteries originate from the aorta closely behind the aortic valve and supply the heart muscle with blood over a network of vessels. This blood is returned to the heart via the coronary sinus (CS). The CS runs closely along the posterior LA wall and then enters the RA in the vicinity of the IVC ostium.

2.1.2 General Physiology

Cardiac myocytes are excitable. In the cellular membrane, specific ionic channels, pumps, and exchangers for mainly Na^+ , K^+ , and Ca^{2+} ions are embedded (see Fig. 2.2). During the resting phase, they maintain a constant transmembrane voltage (TMV) of -80 to -90 mV, i.e. the intracellular potential is 90 mV lower than the extracellular potential. If the TMV is raised above a certain threshold due to external currents (typically -50 to -60 mV), an action potential (AP) as shown in Figure 2.3 is triggered.

The sudden increase in TMV (Phase 1) is mainly caused by the opening of Na^+ gates as soon as the threshold voltage is reached. After several milliseconds, the Na^+ channels are inactivated. In the following, the influx of Ca^{2+} from the extracellular space prolongs the AP and results in the plateau phase (Phase 2). After 200 to 400 ms, outward K^+ currents repolarize the membrane (Phase 3) to the original resting potential (Phase 4). The Na^+ channels are not reactivated unless repolarization is almost complete, which makes the cell refractory during the AP course. This means that no

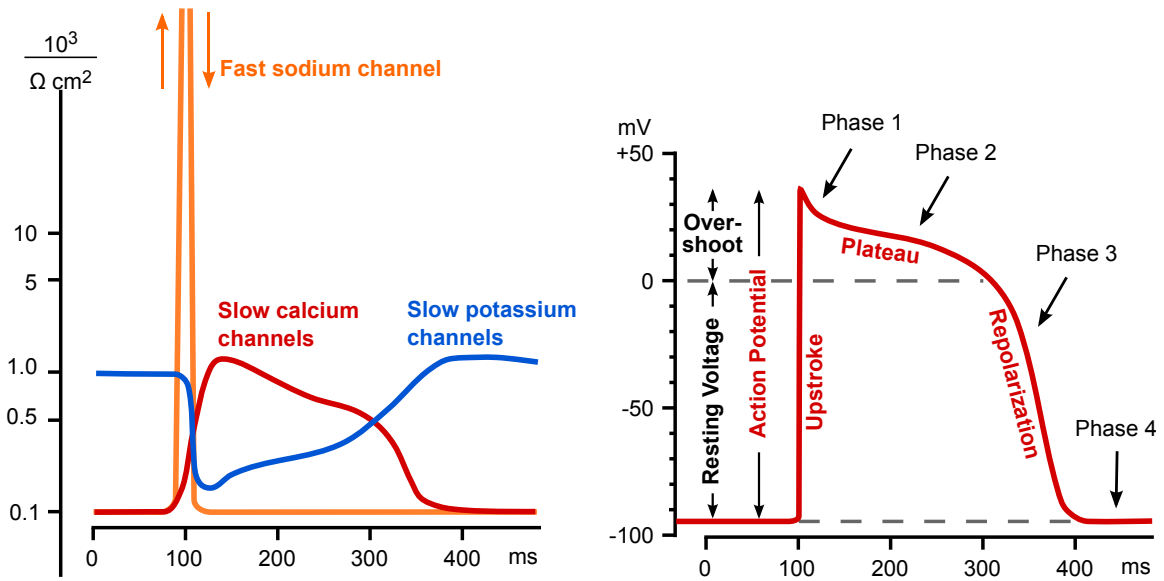


Fig. 2.3. Time-dependent conductivities of the most important ionic channels (left) and resulting action potential (right), both schematic. The AP comprises a fast upstroke during the depolarization, a plateau phase, and a slower repolarization. Adopted from [6].

further excitations can be triggered before the first AP is complete. As a result of the Ca^{2+} influx during the plateau phase and further Ca^{2+} release from the sarcoplasmic reticulum, mechanical contraction of the myocyte is triggered.

Adjacent cells are coupled via so-called gap junctions. They are formed by two non-selective ion channels (connexons) from the opposing cells. Each connexon consists of six connexin proteins. Excitation from a depolarized cell to a neighbour cell spreads to a large extent via intercellular currents through gap junctions. Therefore, conductivity of the gap junctions is an important factor for the speed of excitation conduction, the so-called conduction velocity (CV). Because all cardiac cells are electrically coupled by such gap junctions, the heart is an electrical syncytium. This means that the whole myocardium will be excited if an electrical excitation is triggered anywhere in the heart [2].

A small part of the cardiac cells belongs to the cardiac excitation-conduction system. These cells have an unstable resting potential and are thus self-depolarizing. They can be found in the sinus node (SN), the atrio-ventricular (AV) node, the Bundle of His and the left and right bundle branches. The sinus node is located subepicardially in the RA, close to the orifice of the superior vena cava and is the primary pacemaker. Excitation spreads over the atria to the AV node, where a proper delay of conduction is added. A fast-conducting pathway continues along the bundle branches to the apex. From there, excitation spreads over the whole myocardium via the Purkinje fibers.

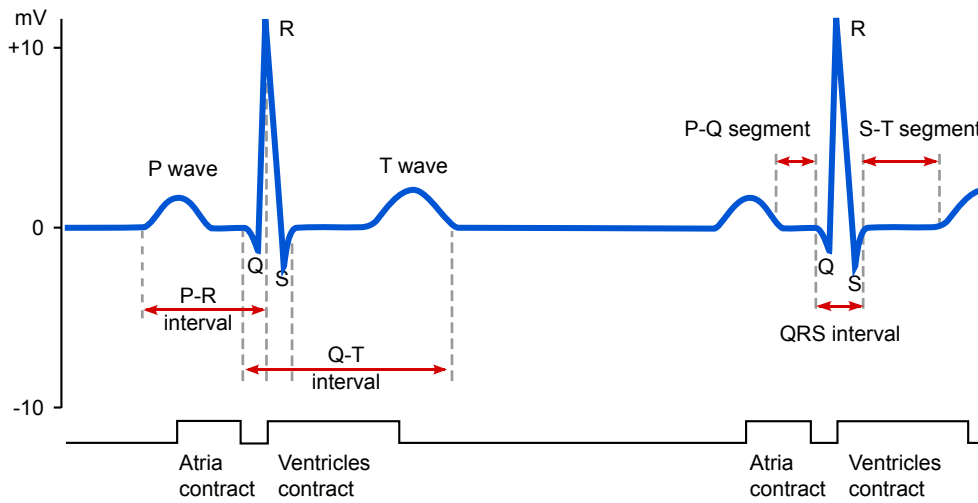


Fig. 2.4. Standard ECG. During the P-wave, the atria depolarize. The QRS complex marks depolarization of the ventricles, and the T-wave is caused by the repolarization of the ventricles. Adapted from [3].

2.1.3 Measuring Electrical Heart Activity on the Body Surface

Depolarization wavefronts on the myocardium cause currents, which create an electrical field in the torso and on the body surface. Measuring the electrocardiogram (ECG) on the body surface is a routine clinical procedure with a very high diagnostic value. Typically, potential differences between two points are measured. For example, the Einthoven leads I to III are measured between right arm and left arm, right arm and left leg, and left arm and left leg. Lead systems of 3 or 12 leads are common in clinical practice.

A typical ECG signal as depicted in Figure 2.4 can be divided into three parts: During the P-wave, the atria depolarize. The QRS complex describes the depolarization of the ventricles. Finally, the T-wave represents repolarization of the ventricles. Atrial repolarization is normally obscured by the QRS complex and thus cannot be recognized in the ECG.

Besides clinical ECG recordings, so-called body surface potential maps (BSPMs) can be acquired with 64 or 80 electrodes distributed over the body surface. As can be seen in Figure 2.5, most of the electrodes are located on the left anterior thorax side. There, the spatial potential variation is highest because the region is close to the heart. With such dense measurements, the potential distribution on the whole torso can be visualized and analyzed in more detail than possible for normal ECG measurements.

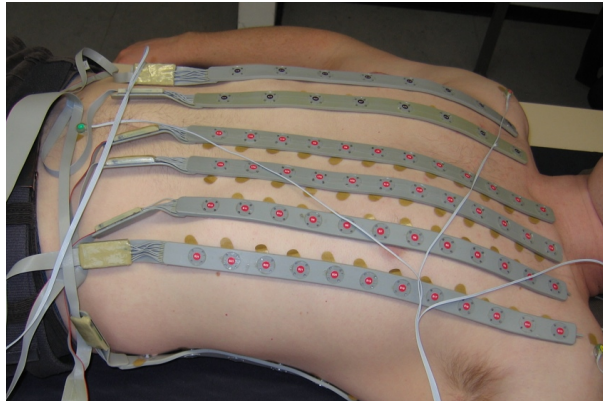


Fig. 2.5. Body Surface Potential Map acquisition. The electrodes are mainly located on the left chest, which is closest to the heart.

2.2 Atrial Arrhythmias

2.2.1 Specific Atrial Anatomy and Physiology

The atrial walls are relatively thin compared to the ventricles. Observations in the LA revealed values between 1 and 3 mm with variations between the different parts of the LA [7]. Thinner walls were reported especially at the LA roof and thicker walls at the septum that separates RA and LA.

Besides the septum, the RA mainly consists of three parts: the appendage, the venous part and the vestibule [8]. The appendage is located anterior and laterally with wide junctions to the venous part and the vestibule. Its surface contains the pectinate muscles that originate in the Crista Terminalis. The venous part receives the caval veins, and the vestibule describes the smooth-walled myocardium around the tricuspid valve.

The Crista Terminalis is a horseshoe-shaped muscular structure that is significantly thicker (typically 2 to 10 mm) than the normal atrial wall. It originates close to the sinus node, extends inferior to the IVC orifice, and ends in the region between the IVC and the tricuspid valve. Thus, it separates the venous part from the pectinate muscles. Its conduction properties are anisotropic with a higher CV in the longitudinal direction up to 10 times faster than in the transverse direction, which makes it a functional conduction block in the transverse direction.

The region between the tricuspid valve and the IVC orifice is referred to as cavotricuspid isthmus. It is a part of re-entrant circuits during typical atrial flutter. Reduced conduction velocities have been reported for the cavotricuspid isthmus in patients suffering from atrial flutter [9]. It is therefore a standard target for ablation.

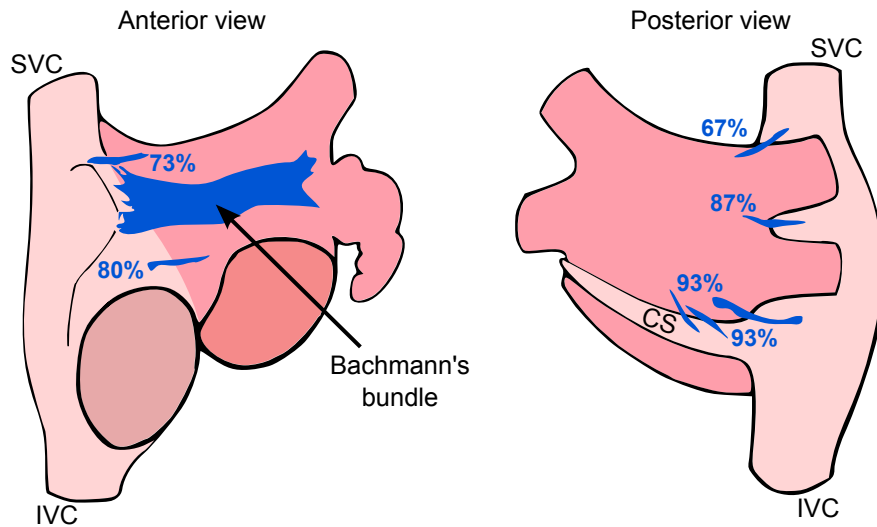


Fig. 2.6. Interatrial bridges between right and left atrium in 15 specimens [12].

The LA comprises four components: appendage, vestibule, venous part, and septum. All parts except the left atrial appendage (LAA) have a smooth wall without trabeculations. The LAA is a tubular structure that is located anterior of the left superior pulmonary vein. The vestibular part covers the area surrounding the mitral valve. The venous component receives the PVs. Typically, there are two left and two right PVs: the left superior PV (LSPV), the left inferior PV (LIPV), the right superior PV (RSPV), and the right inferior PV (RIPV). However, there exist variations in number, size, and shape of the ostial regions [10]. Muscular sleeves surround the PV ostia [11]. The LA walls are often described as superior/roof, posterior, lateral, septal, and anterior [8].

Excitation conduction between RA and LA has not yet been completely understood. However, three mechanisms are widely accepted to play an important role [12] (Fig. 2.6). Firstly, Bachmann's Bundle originates in the RA close to the SVC orifice and extends over the septum to the region of the LAA. According to [12] it is present in 73% of the population. Secondly, the rim of the fossa ovalis was shown to connect the RA and LA during LA pacing [13]. Finally, the CS was reported to contain its own musculature and to serve as intraatrial connection [13, 14].

Measurements of conduction velocity in the human atrium are scarce. CVs on the RA free wall between 68 and 103 cm/s (mean value 88 ± 9 cm/s) have been reported by Hanson et al. [15] in patients suffering from ischemic heart disease or Wolff-Parkinson-White syndrome. In the cavotricuspid isthmus, CVs between 37 and 42 cm/s were measured during pacing in patients with a history of atrial flutter and

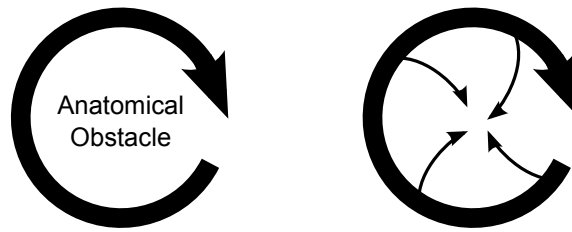


Fig. 2.7. Macroscopic reentries can either occur around an anatomical obstacle (left side) or around a refractory zone that is maintained by the rotor itself (right side, so-called leading circle concept [19]).

values between 50 and 55 cm/s in patients with no such history [9]. Especially, slow conduction was observed in the medial part of the isthmus [16].

Normal effective refractory periods (ERPs) in adults between 150 and 360 ms have been reported [8]. Furthermore, measurements of the ERP in the RA and LA as well as in the PVs were performed in patients without prior history of atrial fibrillation, both before and after inducing and maintaining AF for 15 min. ERPs before vs. after the AF episodes were 248 ± 27 ms vs. 211 ± 40 ms in the PVs, 233 ± 23 ms vs. 214 ± 20 ms in the LA, and 226 ± 29 ms vs. 188 ± 20 ms in the RA [17].

2.2.2 Arrhythmia Types and Underlying Mechanisms

Cardiac arrhythmias can be subdivided into ventricular and supraventricular (i.e. atrial) arrhythmias. Ventricular arrhythmias comprise mainly bundle branch blocks, ventricular extrasystoles, and ventricular tachycardias (repeated ventricular extrasystoles). Supraventricular arrhythmias may have their origin in the sinus node, the atrial myocardium (including the PV ostia), or the AV node [18]. Both focal origins and reentry mechanisms are possible, see below. In this thesis, only supraventricular arrhythmias are considered with a focus on atrial flutter and atrial fibrillation.

Atrial tachycardias with macroscopic excitation fronts may arise from ectopic activity of a single focus (ectopic atrial tachycardia) or multiple foci (multifocal atrial tachycardia), as well as from reentrant circuits. The latter mechanism is referred to as reentry tachycardia or — for frequencies above 220 bpm — atrial flutter. Reentry mechanisms both with and without anatomical obstacle have been demonstrated [19], as shown in Figure 2.7. A key parameter of such reentry circuits is the wavelength calculated as the product of ERP and CV. Thus, it corresponds to the distance travelled by the wavefront during the refractory phase. If it is smaller than the reentry path, the cardiac tissue can be repeatedly excited by the circulating excitation wave. A region of slow conduction in the cavotricuspid isthmus is part of the (clockwise or counterclockwise) reentry path in typical atrial flutter [9]. Atypical atrial flutter

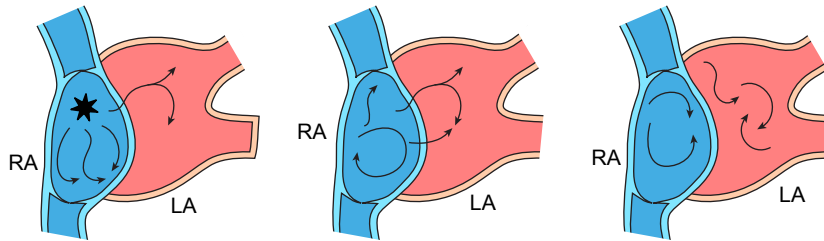


Fig. 2.8. AF is believed to be maintained by a combination of focal activity (left), large-scale rotors (middle) and multiple wavelets (right) [22].

circuits may be located in the RA or LA, for example, around the tricuspid or mitral valve.

Atrial fibrillation (AF), in contrast, is characterized by repetitive, chaotic, and dissynchronous activation of different parts of the atria. AF is classified according to the length of episodes and their termination [8]. If the episodes do not last longer than 7 days and terminate spontaneously, they are referred to as *paroxysmal* AF. Characteristic for paroxysmal AF is an initiating trigger that is often located in the pulmonary veins [20]. In contrast, *persistent* AF lasts from 7 days to several months and does not terminate spontaneously. Sites showing complex fractionated atrial electrograms have been associated with the maintenance of persistent AF [21].

The mechanisms of AF maintenance are still under debate. It is assumed that a combination of focal activity, single mother rotors and multiple wavelets maintains the arrhythmia [22], see Figure 2.8.

2.2.3 Remodeling

The atrial substrate responds to atrial fibrillation by structural and electrophysiological changes, a process known as remodeling. Unfortunately, these changes favour the genesis and maintenance of further arrhythmia episodes. This vicious circle is also described as “AF begets AF” [22, 23].

Three major contributions to cellular remodeling have been identified: electrical, contractile, and structural remodeling [24], see Figure 2.9. Electrical remodeling affects the ionic channels. Due to the repetitive activations with short cycle lengths, the cellular Ca^{2+} loading increases. As a protection mechanism, the conduction of the $I_{\text{Ca,L}}$ current is reduced on a time scale of several minutes, and the expression of the $I_{\text{Ca,L}}$ channels is reduced within several hours to days [22]. The reduced $I_{\text{Ca,L}}$ leads to a shorter APD and ERP, which in its turn decreases the wavelength and favours reentry. Furthermore, an increase in the inward rectifier K^+ current I_{K1} leads to a reduced resting transmembrane voltage and a further APD shortening. Finally, although it

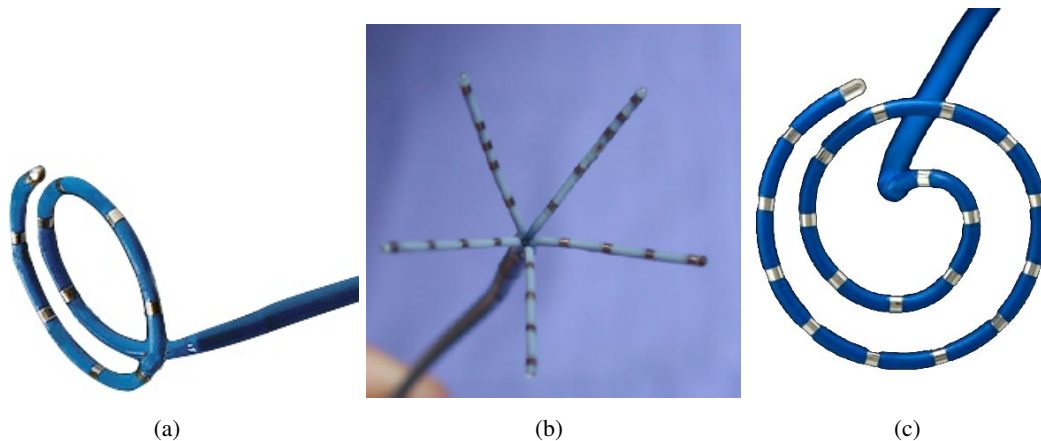


Fig. 2.10. Three different intracardiac measurement catheters [4]. (a) Inquiry Optima circular mapping catheter (www.sjm.com). (b) Biosense Pentaray catheter (www.spo.escardio.org). (c) Inquiry Optima AFocus spiral catheter (www.sjm.com).

examinations, catheter ablation can be performed to damage areas of pro-arrhythmic substrate to such an extent that excitation conduction in this tissue is blocked.

2.3.1 Catheter Types and Mapping Techniques

There exist different catheter types with different shapes as well as electrode number and arrangement. A standard mapping catheter with typically eight or ten electrodes arranged in pairs is placed in the CS. It covers a large region in the LA around the mitral valve and records signals both from the LA and the left ventricle. Excitation in the CS catheter normally starts at the proximal end during sinus rhythm.

For spatial mapping, a circular mapping catheter as shown in Figure 2.10(a) is often inserted into the atria. Especially for PV isolation during AF ablation, it is used to find excitation breakthroughs from the PV ostia to the LA myocardium. Many circular catheters are variable in diameter, i.e. the diameter can be adjusted during the examination. Further catheters that cover a larger area are the PentaRay catheter (Biosense Webster, Diamond Bar, USA; Fig. 2.10(b)) and the AFocusII spiral catheter (St. Jude Medical, St. Paul, USA; Fig. 2.10(c)). Such catheters can be used for high-density mapping [30, 31], e.g. the localization of ectopic foci.

The current position of the catheter in the heart can be tracked by x-ray fluoroscopy. However, in recent years, 3D electroanatomical mapping systems have been developed such as Biosense CARTO and EnSite NavX (St. Jude). They allow to localize the catheter electrodes based on magnetic sensors (older CARTO systems [32]) or impedance measurements in high-frequency transthoracic electrical fields (CARTO3 [33] and Ensite NavX [34]). It has been shown that such mapping

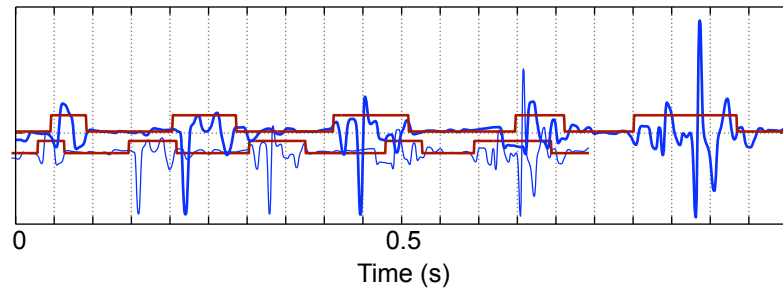


Fig. 2.11. Schematic example of complex fractionated electrogram (blue). Activity is marked by the red curve. Active regions of the fractionated EGM show multiple deflections. Figure modified from [40].

systems can reduce fluoroscopy exposure and procedure duration during PV isolation [35].

2.3.2 Ablation of Cardiac Arrhythmias

The most commonly used catheter ablation techniques are nowadays radiofrequency (RF) [36] and cryothermal [37] ablation. During RF ablation, high-frequency currents with 300 to 1000 kHz are inserted into the tissue at the tip of an ablation catheter. Most commonly, a unipolar setup is used, in which the currents leave the body at a large ground electrode at the posterior aspect of the chest. The high density of electric current near the catheter tip causes local resistive heating of the tissue in a 2 mm radius [8]. Due to thermal conduction, deeper regions are progressively heated [38], even after termination of the RF pulse. To form lesions by irreversible cellular death, the tissue must be heated up to at least 50° C. To ensure lesion formation in deeper regions, ablation currents are typically applied for 60 s. However, temperatures should not exceed 70° C to avoid thromboembolic complications. Therefore, tip temperature and impedance are constantly monitored. To avoid local temperature peaks at the electrode tip, irrigated tip electrodes are used.

Cryothermal catheter ablation is performed by delivering a refrigerant (typically liquid nitrogen) through the catheter shaft that expands in the catheter tip. This results in a cooling of the tip and the surrounding tissue. The tissue is damaged and replaced by fibrotic tissue within a few weeks after the procedure [8]. It is an alternative to RF ablation, and possible advantages of both approaches are currently under study [39]. Typical targets for catheter ablation are the pulmonary veins, re-entry paths, and sites of focal activity. However, attention has recently been drawn also to sites showing complex fractionated atrial electrograms that may be sustaining persistent AF [21]. An example signal is shown in Figure 2.11. The ultimate goal of catheter ablation is restoring sinus rhythm. This is not always achieved, however, in such cases at least a rhythm regulation may be possible [41].

Simulation and Quantitative Analysis of Cardiac Excitation

This chapter describes the basics for simulating cardiac excitation and analyzing measured data of cardiac activation. The required components for simulations are an anatomical model, cellular electrophysiological models, and excitation conduction models. Optionally, the resulting surface ECG can be forward-calculated. Furthermore, an overview of simulation approaches and analysis techniques is given.

3.1 Anatomical Models

Anatomical models describe the geometry of the heart. In addition, inside the heart different tissue types can be differentiated. Different possibilities to create such models are available.

3.1.1 Visible Human Project

The visible human project comprises two highly detailed anatomical data sets of a 38 year old man (Visible Man, VM) and a 59 year old woman (Visible Female) [42, 43]. Computed tomography (CT) and magnetic resonance (MR) images were acquired from both whole bodies. Afterwards, the bodies were frozen and cut into small slices of 1 mm (VM) and 0.33 mm (Visible Female) thickness. These cryosections were photographed and digitalized and provided additional high resolution data. From the CT and MR scans together with the cryosection images, high resolution models of the thorax and the heart were created. Examples of the VM data are shown in Figure 3.1.

3.1.2 Individual Segmentation

While principal questions can be investigated in the visible human models, clinical applications require personalized anatomical models. These must be derived based on data from standard medical imaging techniques such as CT or MR imaging. The

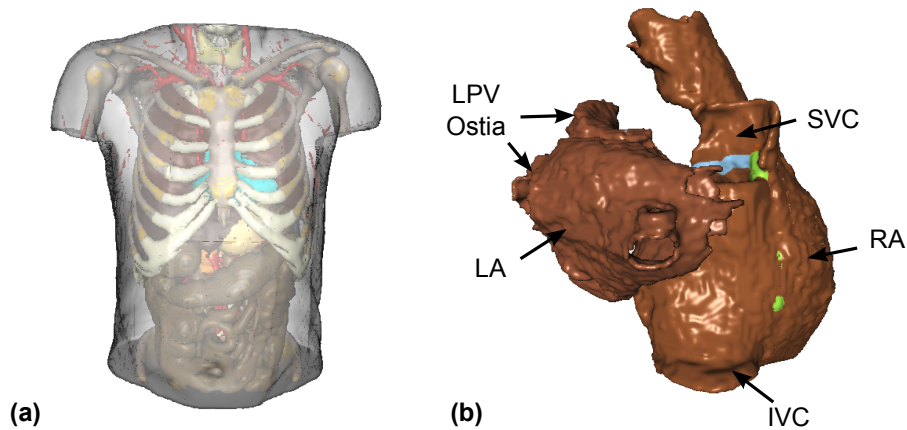


Fig. 3.1. Visible Man (VM) data set. (a) Semi-transparent anterior view of the torso model. (b) Posterior view of the atrial model.

segmentation of the data can be performed manually, for example, using deformable meshes.

However, manual segmentation is time-consuming and thus hardly applicable for clinical studies. Therefore, automatic or semi-automatic segmentation techniques have been developed. For example, the endocardium of the four cardiac chambers and the epicardial wall of the left ventricle can be segmented with an active-shape approach proposed by Lorenz and von Berg [44], see Figure 3.2. Segmentation of the atrial epicardium is not included in this model, because the atrial walls are very thin and cannot be distinguished on normal CT or MR scans. However, the simulations performed in this thesis are based on models with finite wall thickness, therefore, this approach cannot be directly applied.

3.2 Electrophysiological Cell Models

The ionic properties of different cell types are described by electrophysiological cell models. They can include a detailed description of all ionic channels or be based on phenomenological properties. The heart comprises different cell types with different ionic properties, therefore, it can be necessary to combine different cell models in one simulation. This is made possible by including the different cell models in a common C++ framework [45].

3.2.1 Hodgkin-Huxley Model

The basis for the current mathematical models of cellular electrophysiology was proposed in 1952 by Hodgkin and Huxley [46]. Their model described an electrical equivalent circuit for a giant squid axon membrane and is depicted in Figure 3.3(a).

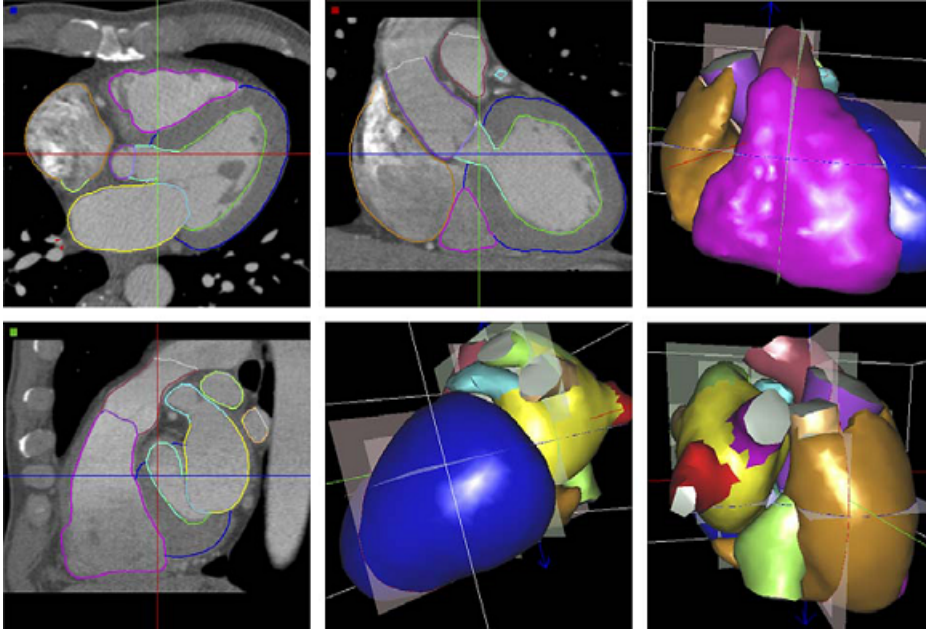


Fig. 3.2. Segmentation results with the active-shape approach proposed by Lorenz and von Berg [44].

Ion channels are modeled as voltage dependent resistors, and the voltage sources are determined by the Nernst voltages (and thus the concentration gradients). The cell membrane itself is represented by a capacitance C .

The total transmembrane current I_{mem} is the sum of the sodium current I_{Na} , the potassium current I_{K} , and the leakage current I_{L} :

$$I_{\text{mem}} = I_{\text{Na}} + I_{\text{K}} + I_{\text{L}}. \quad (3.1)$$

Considering also intercellular currents I_{inter} , the change in transmembrane voltage V_m can be calculated according to [5] as

$$\frac{dV_m}{dt} = -\frac{1}{C} (I_{\text{mem}} - I_{\text{inter}}). \quad (3.2)$$

3.2.2 Courtemanche et al. Model

A cell model for the atrial working myocardium has been developed by Courtemanche, Ramirez, and Nattel (referred to as CRN model) based on data from humans and animals [47]. A schematic description is shown in Figure 3.3(b). The sum of the different ionic currents represents the total membrane current

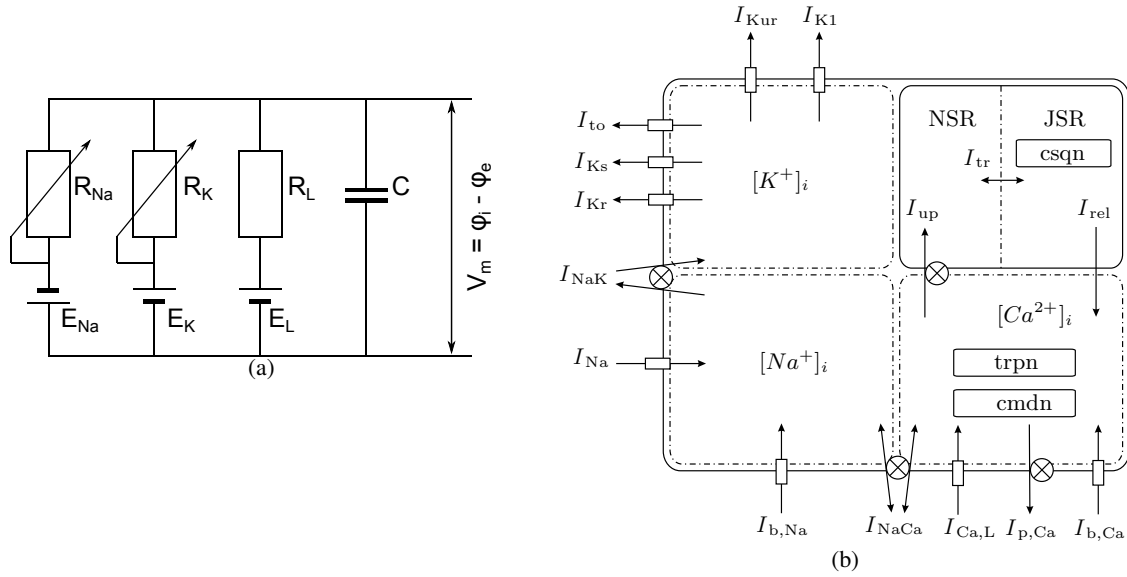


Fig. 3.3. (a) Hodgkin-Huxley model of a giant squid axon. (b) Atrial cell model by Courtemanche, Ramirez, and Nattel [47]. Figures adopted from [5].

$$I_{mem} = I_{Na} + I_{K1} + I_{to} + I_{Kur} + I_{Kr} + I_{Ks} + I_{Ca,L} + I_{p,Ca} + I_{NaK} + I_{NaCa} + I_{b,Na} + I_{b,Ca}. \quad (3.3)$$

The different currents are: I_{Na} = fast Na^+ ; I_{K1} = rectifier outward K^+ ; I_{to} = transient outward K^+ ; I_{Kur} = ultra rapid delayed outward K^+ ; I_{Kr} = rapid delayed outward K^+ ; I_{Ks} = slow delayed outward K^+ ; $I_{Ca,L}$ = L-type inward Ca^{2+} ; $I_{p,Ca}$ = Ca^{2+} pump outward; I_{NaK} = Na/K pump; I_{NaCa} = Na/Ca exchanger; $I_{b,Na}$ = background Na^+ ; and $I_{b,Ca}$ = background Ca^{2+} . Details can be found in [47].

It is known that the ionic concentrations in the model drift away from the steady-state values during long-term repetitive stimulations. Solutions to overcome this limitation have been proposed in [48].

The properties of electrophysiological remodeling during AF as described in section 2.2.3 can be implemented into the model by changing the corresponding model parameters [49].

3.2.3 Minimal Model

The Courtemanche model described in section 3.2.2 is a detailed mathematical description of the ionic processes on the cell level. In contrast, a rather phenomenological model, the so-called “minimal model” (MM), has been proposed by Bueno-Orovio, Cherry, and Fenton [50]. It describes more abstract currents which, however, reflect the most important features of detailed ionic models, such as AP morphology and restitution behaviour. The MM is an extension of the Fenton-Karma model [51]

Table 3.1. Parameter sets for the MM for ventricular cells as supplied in [50].

	u_o	u_u	θ_v	θ_w	θ_v^-	θ_o	τ_{v1}^-	τ_{v2}^-	τ_v^+	τ_{w1}^-
Epi	0	1.550	0.300	0.130	0.006	0.006	60	1150	1.451	60
M	0	1.610	0.300	0.130	0.100	0.005	80	1.451	1.451	70
Endo	0	1.560	0.300	0.130	0.024	0.006	75	10	1.451	6
	τ_{w2}^-	k_w^-	u_w^-	τ_w^+	τ_{fi}	τ_{o1}	τ_{o2}	τ_{so1}	τ_{so2}	k_{so}
Epi	15	65	0.030	200	0.110	400	6	30.018	0.996	2.046
M	8	200	0.016	280	0.078	410	7	91.000	0.800	2.100
Endo	140	200	0.016	280	0.104	470	6	40.000	1.200	2.000
	u_{so}	τ_{s1}	τ_{s2}	k_s	u_s	τ_{si}	$\tau_{w\infty}$	w_∞^*	$V_{m,u}$	V_0
Epi	0.650	2.734	16	2.099	0.909	1.887	0.070	0.940	85.7	-83
M	0.600	2.734	4	2.099	0.909	3.385	0.010	0.500	85.7	-83
Endo	0.650	2.734	2	2.099	0.909	2.901	0.027	0.780	85.7	-83

with an additional state variable for producing spike-and-dome morphology in the AP. Its behaviour can be adjusted by tuning the 28 model parameters listed in Table 3.1.

Details of the model can be found in [50], but a brief summary is given here. The MM describes three major currents: a fast inward current J_{fi} , a slow outward current J_{so} , and a slow inward current J_{si} (Figure 3.4(a)). No absolute correspondence between these phenomenological currents and real ionic currents exists. However, J_{fi} mainly represents the sodium currents during AP upstroke, J_{so} the potassium currents during repolarization, and J_{si} the calcium currents during the plateau phase. Current equations are given as

$$J_{fi} = -\frac{v \cdot H(u - \theta_v)(u - \theta_v)(u_u - u)}{\tau_{fi}} \quad (3.4)$$

$$J_{so} = \frac{(u - u_o)(1 - H(u - \theta_w))}{\tau_o} + \frac{H(u - \theta_w)}{\tau_{so}} \quad (3.5)$$

$$J_{si} = -\frac{H(u - \theta_w) \cdot w \cdot s}{\tau_{si}} \quad (3.6)$$

where $H(x)$ is the Heaviside (or step) function. The four state variables implemented in the model are u (corresponds to scaled TMV), v (gate for J_{fi} /sodium current), as well as w and s (gates for J_{si} /calcium current). Their time-dependence is shown in Figure 3.4(b) and is governed by the following equations:

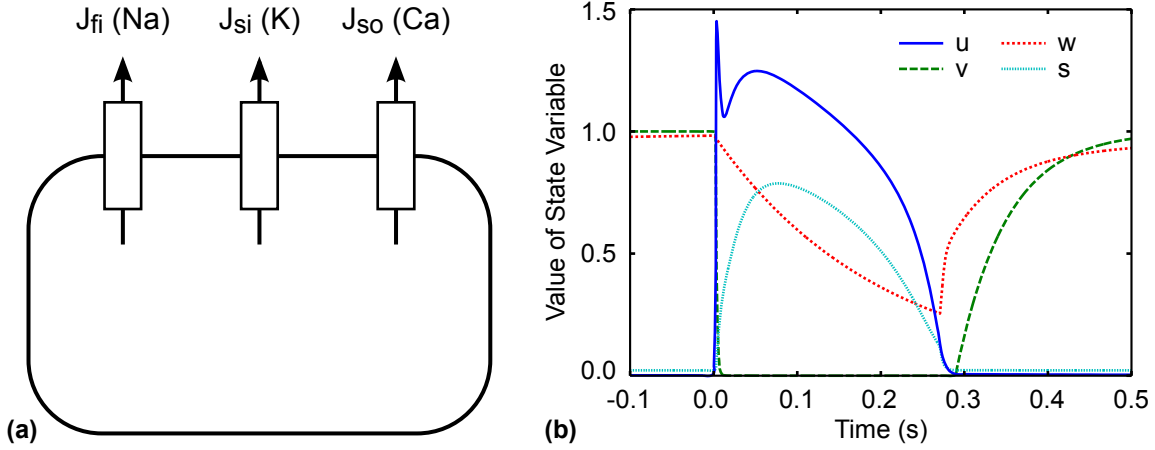


Fig. 3.4. Minimal Model. (a) Schematic description of currents. (b) Time-course of the state variables for the supplied ventricular parameter set (epicardial cells).

$$\partial_t u = \nabla(\tilde{D}\nabla u) - (J_{fi} + J_{so} + J_{si}) \quad (3.7)$$

$$\partial_t v = \frac{(1 - H(u - \theta_v))(v_\infty - v)}{\tau_v^-} - \frac{H(u - \theta_v) \cdot v}{\tau_v^+} \quad (3.8)$$

$$\partial_t w = \frac{(1 - H(u - \theta_w))(w_\infty - w)}{\tau_w^-} - \frac{H(u - \theta_w) \cdot w}{\tau_w^+} \quad (3.9)$$

$$\partial_t s = \frac{(1 + \tanh(k_s \cdot (u - u_s)))/2 - s}{\tau_s} \quad (3.10)$$

Several of the time constants determining the evolution of the currents or state variables are functions of the voltage variable u :

$$\tau_v^- = (1 - H(u - \theta_v^-)) \cdot \tau_{v1}^- + H(u - \theta_v^-) \cdot \tau_{v2}^- \quad (3.11)$$

$$\tau_w^- = \tau_{w1}^- + \frac{(\tau_{w2}^- - \tau_{w1}^-) \cdot (1 + \tanh(k_w^- \cdot (u - u_w^-)))}{2} \quad (3.12)$$

$$\tau_{so} = \tau_{so1} + \frac{(\tau_{so2} - \tau_{so1}) \cdot (1 + \tanh(k_{so} \cdot (u - u_{so})))}{2} \quad (3.13)$$

$$\tau_s = (1 - H(u - \theta_w)) \cdot \tau_{s1} + H(u - \theta_w) \cdot \tau_{s2} \quad (3.14)$$

$$\tau_o = (1 - H(u - \theta_o)) \cdot \tau_{o1} + H(u - \theta_o) \cdot \tau_{o2} \quad (3.15)$$

As an example, τ_v^- takes on either the value τ_{v1}^- or τ_{v2}^- with a step-like transition at θ_v^- . In contrast, τ_w^- takes on values between τ_{v1}^- and τ_{v2}^- . The transition is smooth, it reaches the mean value of both at u_w^- , and the sharpness of the transition is determined by k_w^- .

Further definitions comprise limits for the gating variables:

$$v_\infty = \begin{cases} 1, & u < \theta_v^- \\ 0, & u \geq \theta_v^- \end{cases} \quad (3.16)$$

$$w_\infty = (1 - H(u - \theta_o)) \cdot (1 - u/\tau_{w_\infty}) + H(u - \theta_o) \cdot w_\infty^* \quad (3.17)$$

The initial conditions for the state variables are $u = 0$, $v = 1$, $w = 1$, and $s = 0$. The TMV can be calculated from u by a linear transformation

$$V_m = V_{m,u} \cdot u + V_0, \quad (3.18)$$

in which V_0 is the resting membrane potential and $V_{m,u}$ is the scaling factor between u and V_m .

It was previously shown that in the MM, action potential duration (APD) and ERP are relatively closely linked. This impairs the simulation of ischemia [52], in which APD is shortened and ERP prolonged. For the simulation of atrial arrhythmias, however, this is not a problem, because no extreme disparity between APD and ERP has been reported.

3.3 Excitation Conduction

Excitation is conducted between adjacent heart cells based on electrical coupling through gap junctions. To model this conduction, macroscopic models which are frequently used were applied in this work. On one hand, the electrophysiologically detailed bi-/monodomain model was used, on the other hand, a rule-based cellular automaton was employed.

3.3.1 Bidomain Model

In the bidomain model, the intra- and extracellular space are considered as two continuous domains [53, 54]. They are separated by the cell membrane, through which the currents between the two domains flow. For each domain, Poisson's equation connects the respective current source densities with the resulting potential Φ

$$\nabla(\sigma_e \nabla \Phi_e) = -\beta \cdot I_m - I_{se}, \quad (3.19)$$

$$\nabla(\sigma_i \nabla \Phi_i) = \beta \cdot I_m - I_{si}. \quad (3.20)$$

The indices i or e denote the intra- or extracellular domain. σ_i and σ_e represent the (possibly anisotropic) conductivity tensors, β is the surface-to-volume ratio of the

cell, I_m stands for the total membrane current and I_{si} and I_{se} for intra- and extracellular stimulus currents.

If no external stimulus currents are applied, the equations can be reformulated to

$$\nabla((\sigma_i + \sigma_e)\nabla\Phi_e) = -\nabla(\sigma_i\nabla V_m). \quad (3.21)$$

This is the first part of the bidomain model. It describes how the transmembrane voltage V_m (calculated from the electrophysiological cell models) influences the extracellular potential. Furthermore, the second bidomain equation can be derived as

$$\nabla(\sigma_i\nabla V_m) + \nabla(\sigma_i\nabla\Phi_e) = \beta \cdot (C_m \cdot \frac{dV_m}{dt} + I_{mem}) - I_{si}. \quad (3.22)$$

It describes how the currents in the intra- and extracellular space affect the intercellular stimulus current, which in its turn serves as input for the cell models.

The excitable cardiac tissue is normally surrounded by an unexcitable bath medium. The extracellular domain is assumed to be connected between the excitable cells and the bath with different conductivity tensors. The intracellular domain is not defined in the bath, i.e. $\sigma_i = 0$. A Dirichlet boundary condition is applied in the bath by setting a grounded potential. At the tissue-bath interface, Neumann boundary conditions are applied to the extracellular and intracellular potential. This means that in the extracellular domain, the normal current density across the boundary must be continuous. In the intracellular domain, the normal current density at the boundary must vanish. Under the assumption that conductivities in the intra- and extracellular domain have the same anisotropy ratio (i.e. $\sigma_i = \kappa \cdot \sigma_e$), the monodomain equation can be derived as

$$\nabla(\sigma_i\nabla V_m) = (\kappa + 1) \cdot \beta \cdot (C_m \cdot \frac{dV_m}{dt} + I_{mem}). \quad (3.23)$$

In practice, the monodomain model is significantly less computationally intensive and was therefore used in this work for electrophysiologically detailed simulations.

3.3.2 Cellular Automaton

In contrast to the detailed electrophysiological models coupled with the bidomain approach, the cellular automaton (CA) is a rule-based system [55]. The principle function of the CA is depicted in Figure 3.5. Conduction times between adjacent cells are calculated from the intercellular distance and the predefined conduction velocity (CV). After a cell has been activated, it is unexcitable for a configured refractory time.

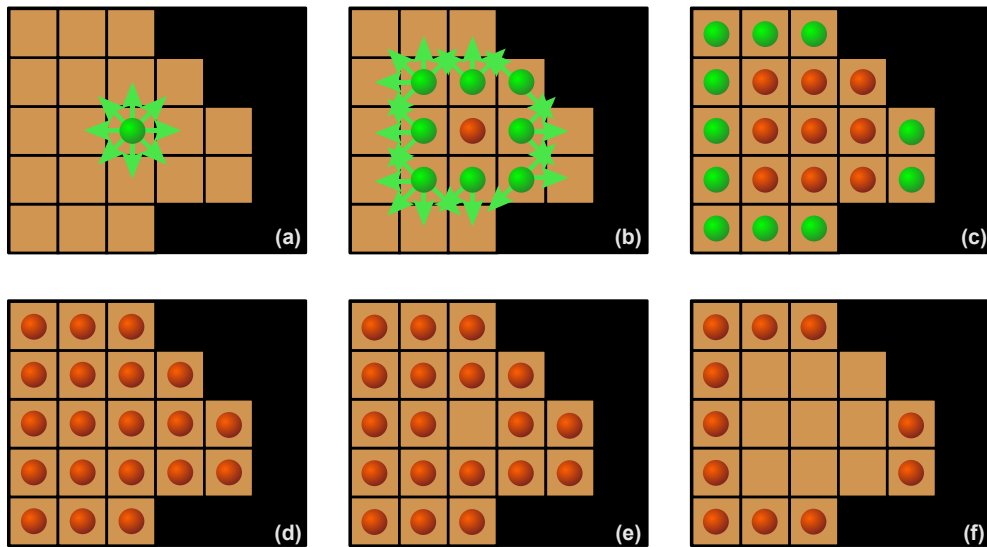


Fig. 3.5. Principle function of a cellular automaton. Active elements are marked with green dots, red dots represent the refractory cells. From an initial stimulus (a), excitation is conducted to neighboring cells (b). During the plateau phase, the elements are refractory (c,d). After repolarization (e,f) the cells can be excited again. Figure adapted from [5].

Finally, it becomes re-excitable again. Whenever a cell in the CA has been excited, a precalculated action potential course takes place in the cell.

Different AP courses, CVs and refractory periods can be stored for up to 255 distinct tissue types. AP courses and the upcoming refractory periods can further depend on heart rate (i.e. the preceding cycle length) and level of repolarization when the last excitation occurred.

The CA is much faster than detailed electrophysiological models coupled with the bi-/monodomain approach. However, all states and transitions are discrete. Especially for simulations of chaotic rhythms e.g. during atrial fibrillation (AF), it therefore suffers from discretization artifacts. Thus, it was only used for simulations during sinus rhythm or during controlled stimulation in this work.

3.4 Forward Calculation and Tissue Conductivities

The forward problem of electrocardiography calculates the resulting potential distribution on the body surface from the electrical current sources in the heart.

3.4.1 Forward Problem Formulation

To calculate the potentials in the torso and on the torso surface, a model of the torso volume is required. In principle, the bidomain equation (3.21) could be solved in a

combined model of the heart and thorax. This would directly calculate the extracellular potential in the torso as part of the bath medium.

However, this is hardly recommendable or feasible due to computational reasons. In practice, a two-step approach is commonly used. First, the transmembrane voltage distribution on the heart is calculated with the monodomain model or a cellular automaton. The right-hand side of (3.21), which constitutes the impressed current source density, is then calculated from V_m as $I_{\text{imp}} = -\nabla \cdot (\sigma_i \nabla V_m)$. In a second step, the remaining differential equation

$$\nabla \cdot [(\sigma_i + \sigma_e) \nabla \Phi_e] = I_{\text{imp}} \quad (3.24)$$

is solved using a finite element technique (with $\sigma_i = 0$ in the torso). To this end, a tetrahedron model of the heart and surrounding torso is created, in which the extracellular potential Φ_e is calculated [56].

3.4.2 Conductivities and Importance of Different Tissue Types

For a given set of cardiac sources during an excitation sequence, the electric field in the torso and on the torso surface is mainly determined by size and position of internal organs and structures (also referred to as inhomogeneities). However, it is known that electrical conductivity and degree of anisotropy of the various tissues, fluids, and structures vary [57, 58]. Thus, their influence on the surface ECG cannot be intuitively predicted.

Obviously, there is a lack of consensus in the literature about measured tissue conductivity values [59]: For all major tissues in the thorax, the conductivities differ by a factor of 2.3 to 16.5 comparing different studies. As an example, values between 0.0544 S/m [60] and 0.9 S/m [61] for the conductivity of the kidneys have been reported.

Partly, these differences are due to the technological challenges that occur when measuring conductivities in the low frequency range that is relevant for the forward problem. Further deviations arise from differing measurement techniques [62], measurements on different species or even sample variations within the same species. Apart from that, many measurements are performed ex-vivo after the sample has been excised, for which it is known that tissue conductivities change [63, 64]. Finally, pathological conditions may cause changes in tissue or fluid conductivity [65, 66]. These variations also influence simulated ECGs. The higher the conductivity uncertainty for a specific tissue becomes, the more severe modeling errors it can introduce depending on site and location with respect to the electrodes.

Simulation studies have previously attempted to characterize how such inhomogeneities influence the computed body surface potential maps (BSPMs). Studies based on dipole sources [67] and measured epicardial signals [68] have been reported. However, they do not consider the lack of consensus in the literature mentioned above. Furthermore, no studies based on simulated physiological excitation sequences exist to the knowledge of the author.

3.5 Atrial Simulations

Atrial simulations have reached a level of sophistication that allows for moving towards clinical applications, e.g. interpreting study outcomes and aiding in therapy design [69].

The simplest and earliest models represented the two atria as two spheres with holes for the veins and valves [70, 71], for example to study re-entry behaviour. More realistic 2D surface models were derived from MR images [72, 73]. The first 3D model including atrial wall thickness was presented in [74] with simulations using the Nygren et al. cell model [75]. Further studies on 3D models have also been performed with the VM data set [76] and the CRN model.

A substrate for atrial fibrillation was for example modeled by introducing patchy heterogeneities in APD_{90} [72]. Sustained AF was then induced by rapid pacing with a cycle length of 150 ms. In the 3D visible female atria, AF was induced in a cellular automaton simulation by S1-S2 pacing. Different ablation strategies were then evaluated with respect to their effect on AF suppression [77].

Recently, special attention is paid to complex fractionated atrial electrograms. Such signals are likely to result from fibrotic tissue which plays an important role in the maintenance of persistent AF. Simulations of fractionated electrograms in a 2D tissue patch with high resolution yielded valuable insights into possible underlying mechanisms to the development of fractionated electrograms [78].

3.6 Quantitative Analysis of Electrophysiological Measurements

Intracardiac electrograms (EGMs) recorded during electrophysiological (EP) studies can be classified qualitatively by the physician, e.g. in terms of which electrodes are activated first and which are activated later [31, 30]. Alternatively, mapping techniques such as activation mapping can be used to identify the earliest point of activation.

There are interesting parameters that can be quantitatively determined from cardiac mapping data, especially the local wave direction and conduction velocity (CV). These parameters can aid in the understanding of the arrhythmia pattern and possible substrate changes. Some quantitative approaches have been applied [79, 80, 81], however they require additional efforts. Local activation time (LAT) maps are regularly interpolated from measured activation times at different locations. Such maps give an overview of activation patterns if these are stable over several minutes, which is the time required to record the map. This is possible, for example, during sinus rhythm or atrial flutter. Local direction of propagation and CV were estimated from LAT maps using a three-point method [79, 80] or vector field analysis [81]. However, the LAT map must be recorded at a large number of sites in the atrium and is therefore time-consuming to create. A problem is that the arrhythmia pattern can change during the examination, for example, after starting the ablation. Then, a new activation map must be recorded for every new pattern to perform the analysis.

A quantitative analysis of *single* wavefronts was reported based on epicardial measurements from dense electrode arrays. Activation sequences in pigs and dogs were mathematically analyzed with the help of 2D and 3D vector fields [82, 83]. CV in humans has also been measured using dense electrode arrays [15]. However, these methods are invasive and require open-heart surgery, thus, they cannot be applied to a larger group of patients during catheter ablations. An interpolation method for activation times from single simulated wave fronts that were measured with a PentaRay catheter has been proposed by Mase et al. [84]. It is based on radial basis functions and will be further described and investigated in section 6.2.

Of further interest is the analysis of complex fractionated atrial electrograms [85, 86, 87] and electrograms recorded during atrial fibrillation [88]. Finally, CS electrograms recorded during 60 s have been analyzed using correlation analysis [89].

However, such quantitative analysis methods have not yet been applied in clinical practice on a larger scale. This may be due to the fact that they are not implemented in current electroanatomical mapping systems. However, analysis techniques that on one hand are simple and on the other hand deliver data of high diagnostic value could be interesting for manufacturers to implement into future mapping systems.

Part II

Methods

Adaptation of a Minimal Cell Model to Properties of Atrial Tissue

As presented in section 3.2.3, the minimal model (MM) comprises 28 parameters. They can be adjusted to reproduce different AP shapes and restitution behaviours. So far, only parameters for the ventricles were available [50]. In this work, the model parameters have been analyzed and adapted to reproduce excitation properties as given by the CRN model. Both the physiological and the electrical remodeling case were considered.

The adaptation process was performed as follows:

- Detailed model parameter analysis
- Creation of reference curves
- Selection of parameters for adaptation
- Adaptation in 3 steps: AP shape, APD restitution, and CV restitution, followed by iterative refinement

Finally, 2D patch simulations with the CRN and the minimal model considering electrical and structural remodeling (reduction of gap junction conductivity) were performed. The results of the adaptation and the patch simulations will be discussed in chapter 8.

4.1 Parameter Analysis

To better understand the influence of the distinct parameters, a schematic analysis was plotted for the epicardial parameters supplied in [50]. The three currents were analyzed separately, and the results are shown in Figures 4.1 to 4.3.

The fast inward (Na^+) current is controlled by a single gating variable v . The slow outward (K^+) current is not related to a gating variable and only depends on the voltage variable u . The slow inward (Ca^{2+}) current is controlled by two gating variables,

AP Course:	Depolarization			Max Plateau Repolarization		
Value of u :	(0)	θ_v^- (0.06)	θ_v (0.3)	u_u (1.55)	θ_v (0.3)	θ_v^- (0.06)
Threshold θ_v			Na current can be active only here			
Positive Feed-back ($u - \theta_v$)			Positive Feedback increases			
Approaching Maximum ($u_u - u$)			Higher TMV limits inward current			
Current Time Constant	$T_{fi} = 1.45$					
Gating Variable v	1	0			1	
Limit for v	1	0 (Inactivation gates close)				1
Time Constant τ_{v1}	$T_{v1}^+ = 60$	$T_{v2}^- = 1150$	$T_{v+} = 1.45$		$T_{v2}^- = 1150$	$T_{v1}^+ = 60$

Fig. 4.1. Parameters for fast inward current (Na). Promoting or inhibiting factors are color coded from orange to green. Orange represents inhibiting factors (e.g. values close to 0) and green promoting factors (e.g. values close to 1). Time constants are color coded from light blue to violet. Light blue stands for slow processes (large time constants) and violet for fast processes (small time constants). During the AP course, the current can only be active for $u > \theta_v$ (excitation threshold). In this region, the term $(u - \theta_v)$ describes a positive feedback, i.e. more channels open for higher u . The term $(u_u - u)$ corresponds to the inhibition of ion flux for positive TMVs that approach the respective equilibrium potential. The current time constant τ_{fi} that determines the current strength is constant during the AP course. The gating variable v is 1 before depolarization (all channels open) and quickly approaches 0 after depolarization starts (channels inactivated). This is described by the limit that v approaches with the time constant τ_{v1} . Gates become inactivated very quickly ($\tau_{v+}^+ \approx 1$) while reactivation is much slower ($\tau_{v1}^- = 60$).

AP Course:	Depolarization			Max Plateau Repolarization			
Value of u :	θ_o (0.006)	θ_w (0.13)	u_{so} (0.65)	u_{so} (0.65)	θ_w (0.13)	θ_o (0.006)	
Current Type	Proportional u / T_o		Proportional $1 / T_{so}$		Proportional u / T_o		
Time Constant	$T_{o1} = 400$	$T_{o2} = 6$	$T_{so1} = 30$	$T_{so2} = 1$	$T_{so1} = 30$	$T_{o2} = 6$	$T_{o1} = 400$

Fig. 4.2. Parameters for slow outward current (K). It is described without gating variables using two types of currents. For $u < \theta_w$, it amounts to u/τ_o with two regions of different time constants. For $u \rightarrow 0$, the current vanishes. In the region $u > \theta_w$, the current is described as $1/\tau_{so}$, i.e. the time constant τ_{so} directly determines the current strength. τ_{so} values become lowest (i.e. the current strongest) for $u > u_{so}$.

w and s . While the restitution behaviour is mainly controlled by w , the additional variable s enables the presence of spike-and-dome morphology in the AP [50].

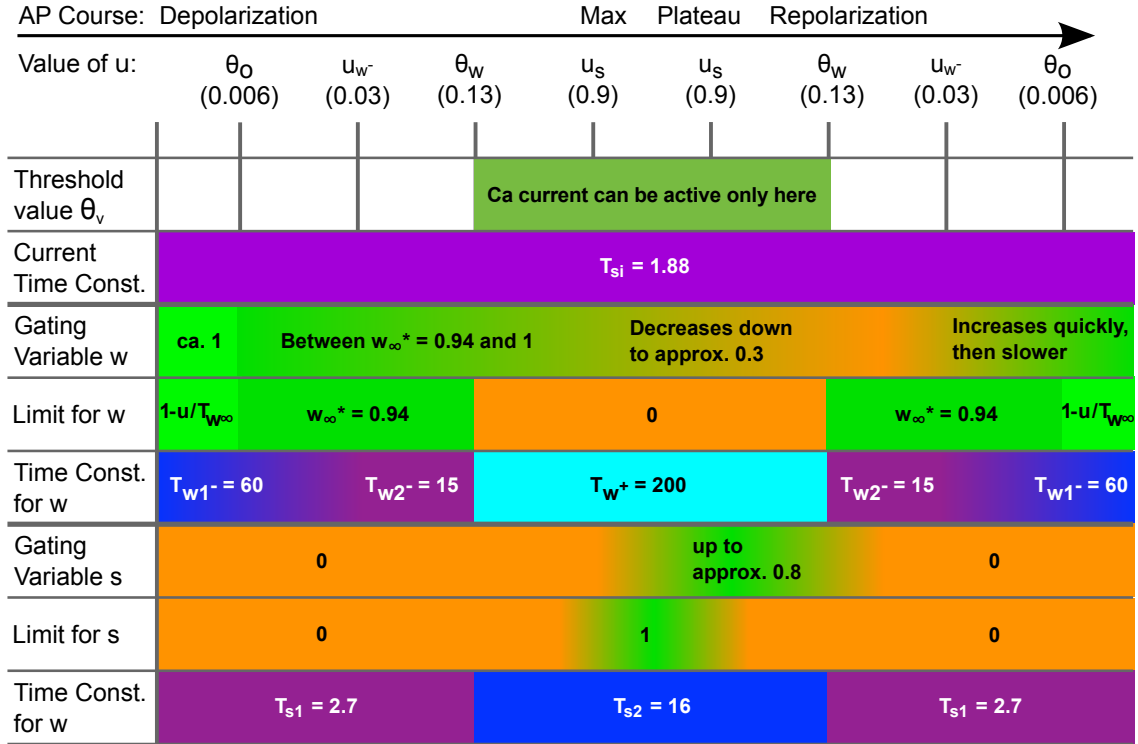


Fig. 4.3. Parameters for slow inward current (Ca). The current can only be active for $u > \theta_w$ and has a time-independent time constant τ_{si} . The gating variable w is close to 1 before depolarization in sinus rhythm. It then decreases slowly during the AP course (limit for w is 0 for $u > \theta_w$ with time constant $\tau_w^+ = 200$). As soon as u falls below θ_w again, w increases. If the next beat is stimulated before w is close to 1, the APD of this beat will be shortened. The gating variable s is 0 before depolarization and increases dome-like in the course of the AP. Thus, it permits to reproduce spike-and-dome morphology in the AP.

4.2 Simulation of Reference Data

Reference data from the CRN cell model for adaptation comprised the AP shape at a cycle length (CL) of 1000 ms, an APD restitution curve (APD vs. CL), and a CV restitution curve (CV vs. CL).

References for both the physiological and remodeling CRN model were simulated in a one-dimensional tissue patch with monodomain coupling. It consisted of $200 \times 1 \times 1$ voxels with 0.1 mm border length. The integration time step for both the cell models and the monodomain coupling was $dt = 10 \mu s$. The conductivity was adjusted such that the CV amounted to approximately 700 mm/s for the physiological model at a CL of 1000 ms.

Stimulations at different cycle lengths were performed on one end, and the resulting APs during propagation were recorded at a distance of 3 mm and 18 mm from the stimulus site. Cycle lengths were chosen in 14 steps between 1250 and 320 ms for the physiological case and in 16 steps between 1250 and 110 ms for the remodeling case.

Steps were chosen with smaller intervals at shorter CLs where APD and CV changes were larger. The resulting steps for the physiological case were 1250, 1090, 1000, 920, 750, 650, 550, 500, 450, 400, 380, 360, 340, and 320 ms. For the remodeling case, they amounted to 1250, 1000, 750, 650, 550, 470, 400, 340, 270, 230, 210, 190, 170, 150, 130, and 110 ms, the last two steps were only included in the CV adaptation.

At every CL, the tissue was initialized with the state after 50 beats of single cell simulations. Then, APD and CV from the fifth stimulus in tissue were recorded as reference. CV was calculated from the time difference and the spatial distance between the two recording sites. APD was calculated as time difference between the maximum TMV and the point at which TMV reached -73 mV. This is the voltage that corresponds to the APD₉₀ in the physiological CRN model at a CL of 1000 ms. It is of advantage to use a fixed threshold instead of 90% of the maximum TMV. Otherwise, parameters causing a change in the maximum TMV could falsely be related to changes in APD.

Furthermore, it is important to note that for the CRN model, AP morphology is considerably different between single cell and patch simulations. Therefore, also the reference curve for the AP shape must be generated in a tissue patch. For the MM, in contrast, AP morphology did not change notably between single cell and patch simulations. Thus, during the optimization, parameter sets could be tested in single cell simulations which are significantly faster.

4.3 Choosing the Parameters for Adaptation

For the actual optimization it is desirable not to tune all 28 parameters simultaneously, but only a limited set that covers the relevant changes in the specific optimization step. As an example, recovery of the state variables u and w should not affect AP shape at a CL of 1000 ms, because under normal conditions they typically have recovered to 1 when the next beat is stimulated. Regarding the AP shape, parameters were manually tuned based on the ventricular parameter set as initial guess. More parameters were successively included until the result was satisfying. The parameters to be optimized in the AP shape adaptation were thus chosen as u_u , θ_w , θ_o , τ_v^+ , τ_{w1}^- , τ_{w2}^- , τ_w^+ , τ_{o1} , τ_{o2} , τ_{so1} , τ_{so2} , k_{so} , u_{so} , τ_{s1} , τ_{s2} , k_s , u_s , τ_{si} , and $\tau_{w\infty}$.

For APD restitution, the parameter set was limited to the main contributors to recovery of the J_{si} (Ca) gating variable w . This comprised τ_{w1}^- , τ_{w2}^- , u_w^- , k_w^- , and w_∞^* . Additionally, small variations of τ_{si} were allowed, which could shift the restitution curve up or down.

Optimization of CV restitution was performed by adjusting τ_{v1}^- and θ_v^- (controlling v recovery) as well as τ_{fi} (upstroke velocity corresponding to a CV shift).

The respective fit borders were chosen empirically such that on one hand, sufficient parameter variations were possible, and on the other hand, physiological constraints were considered.

4.4 Adaptation Process

First of all, the V_0 parameter was set to the resting membrane potential. Then, adaptation of AP shape and APD restitution was performed using an interior point algorithm supplied with Matlab. To this end, a single-cell version of the MM with explicit Euler time integration was implemented. This approach was much more efficient compared to evaluating MM parameter sets in patch simulations.

In the AP shape adaptation step, the reference was preprocessed by detecting the AP upstroke and cutting out an appropriate window of the reference AP. Then, the actual parameter adaptation was performed with respect to the minimal quadratic error between the reference AP and the AP of the adapted model.

The resulting parameter set was used as initial values for the APD adaptation. APD parameters were further tuned manually to estimate a good initial guess. For the actual optimization, single-cell simulations were performed for the same CLs that were used for the reference. From the resulting APs, the APD_{-73mV} value was determined. This way, the quadratic error between the reference APDs and the APDs calculated from the MM model was minimized.

Adaptation of CV restitution started with a manual parameter adjustment. CV adaptation required testing parameter sets in patch simulations in the C++ framework during the adaptation. Combining these patch simulations with the Matlab optimization routines seemed disadvantageous due to several reasons. First, due to the limited spatial and temporal resolution of the patch simulation, for very small parameter changes it could happen that the numerically calculated CV did not change at all. Furthermore, for calculation of numerical derivatives with respect to the varied parameters, a large number of test function calls (in this case time-consuming patch simulations) would be required. Therefore, an alternative technique based on Particle Swarm Optimization, which was implemented in the C++ framework, was used [45]. With 20 test points (so-called particles) in each of the 10 iterations, it could find the minimum with altogether 200 patch simulations.

The adaptation cycle was repeated for iterative refinement. Thus, the result of the CV adaptation was used as initial-guess for another AP shape adaptation. Subsequently,

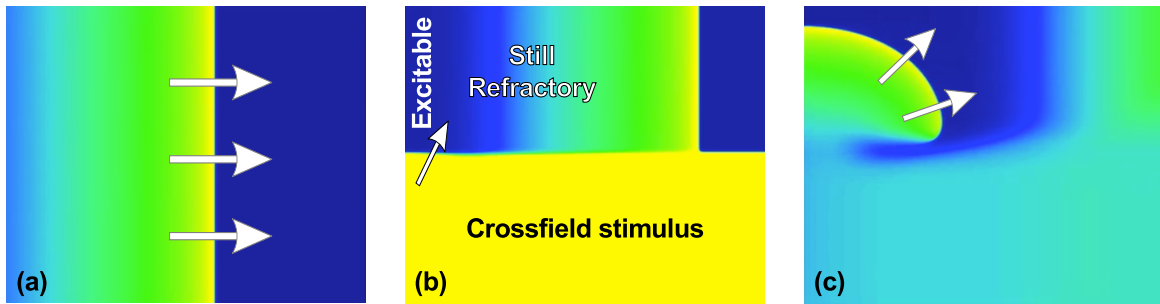


Fig. 4.4. Patch simulation with crossfield stimulus (schematic). (a) The tissue is initialized with plane waves. (b) A crossfield stimulus is applied. It excites the repolarized back of the previous wave. (c) This results in a spiral wave, or rotor, to arise in the tissue.

adaptation of APD and CV restitution were performed with the result of the previous step as initial-guess.

To increase the chance of finding the global minimum, the parameters obtained from the second CV adaptation were randomly varied in the range of $\pm 50\%$ of their final value. This way, each of the adaptation steps was repeated with fifteen new randomly created start vectors. It was then ensured that none of these adaptations resulted in a better fit as it had been achieved before.

4.5 2D Patch Simulations

The adaptation of the MM parameters was performed based on single-cell or 1D tissue simulations. However, when considering simulations of AF, especially 2D wave dynamics are of interest.

Therefore, simulations in a 2D patch of $1000 \times 1000 \times 1$ voxels (size 0.1 mm) were performed to compare the excitation patterns of the CRN and the minimal model. This corresponded to a size of 10×10 cm, which is comparable to the dimensions of a human atrium.

Structural remodeling was included by reducing intracellular conductivity by 30% as described in [49] ($\kappa = 0.046$ S/m). The tissue was initialized with 50 beats of single-cell simulations at a frequency of 3 Hz. Three initialization beats were then performed at the left edge of the tissue with a frequency of 3 Hz. A crossfield stimulus at 140 ms after the last beat created a single spiral wave (schematically shown in Fig. 4.4). It was then exemplarily compared how the system evolved for another smaller ectopic focus 190 ms later in the two models.

Influence of Tissue Conductivities on the ECG

As described in section 3.4, the electrocardiographic forward problem connects the electrical sources in the heart with the resulting potential distribution on the body surface. The electric field in the human torso (and therefore also on the body surface) is strongly influenced by size and position of internal organs and structures (also referred to as inhomogeneities). However, the various tissues, fluids, and structures vary with respect to conductivity and degree of anisotropy [57, 58]. Thus, it is important to quantify their influence on the surface ECG.

Furthermore, tissue conductivities are difficult to determine and the resulting uncertainty [59] could have a strong impact on the calculated body surface potential maps (BSPMs). Especially for patient-individual models it will be difficult to specify exact conductivity values for the different tissues.

To address these problems, the following steps are described in this chapter:

- Tissue conductivity values from previous literature reports were compiled and the importance of different tissues based on a sensitivity and an uncertainty analysis was ranked.
- Based on principal component analysis, a method was developed to quantitatively describe changes in surface potentials caused by conductivity variations.

The corresponding results will be presented in chapter 9.

5.1 Ranking the Influence of Different Tissues

In the following, a literature overview is presented to determine minimum and maximum conductivity values for certain tissues. A test geometry was created based on the VM anatomy to perform forward calculations with different conductivity setups. This way, a sensitivity and an uncertainty analysis were performed [90].

5.1.1 Literature Overview of Tissue Conductivities

To evaluate the conductivity uncertainty in the measurement literature, a table with the conductivity ranges for the most relevant organs was compiled (see results in Table 9.1 on page 86). 10 primary sources [62, 64, 66, 91, 92, 93, 94, 95, 96, 97] and five review articles [57, 60, 61, 63, 98] were considered. The conductivities for each organ were tabulated and sorted for the highest and lowest reported value. If a range of conductivities instead of a single value was stated, the respective upper or lower boundary was considered. An exception was made for the intestine: because reported measurement values were scarce and most anatomical models do not separate between different parts of the intestine, the lower boundary was chosen based on measurements from colon samples and the upper boundary based on values from the small intestine. The forward problem is considered to be quasi-static, therefore measurements that were reported to be performed above 10 kHz were not included in the analysis.

One of the main goals was to include conductivity values that are frequently used in modeling studies. This explicitly included measurements on animal samples that are often used because human data are rare. Furthermore, no distinction was made between in-vivo or ex-vivo studies or measurements at different sample temperatures.

5.1.2 Torso Model and Forward Calculation

Excitation in the VM atria was simulated with the Cellular Automaton parameterized from the CRN model. CV was set to 70 cm/s in the atrial myocardium, 130 cm/s in the crista terminalis and 177 cm/s in Bachmann's bundle [74, 99].

To calculate the surface potentials for different tissue conductivity setups, a tetrahedron torso model was created based on the VM data set. In this model, the forward problem was implemented using the finite element method. The torso model contained the heart and the following tissue types: blood (both intracavitary and in the main vessels), lungs, fat (both visceral and subcutaneous), anisotropic skeletal muscle (referred to as muscle in all tables), intestine, liver, kidneys, bone, cartilage, and spleen. Tissues covering less than 0.5% of the body volume are omitted in this list.

An initial mesh comprising 70,000 nodes was created from a 2 mm voxel data set of the VM torso. Next, the heart region was refined with another 200,000 nodes generated from the high-resolution cardiac data sets: 190,000 nodes for atria and ventricles and 10,000 for the major blood vessels in the vicinity of the heart.

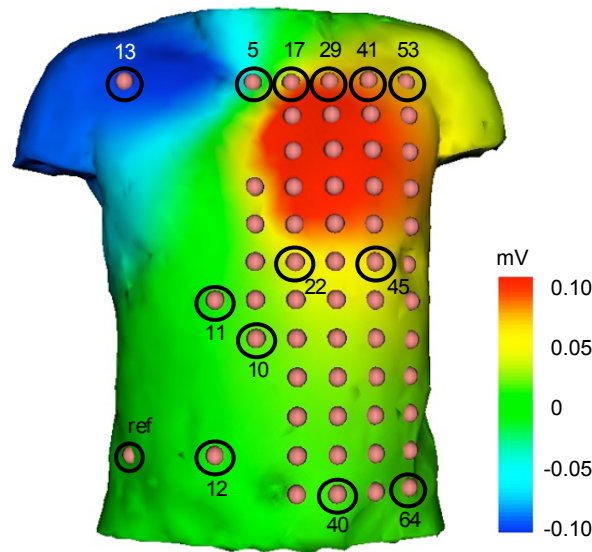


Fig. 5.1. Tetrahedron model of the VM torso. A BSPM is superposed for atrial activation at 41 ms. Electrode locations at which the body surface potentials were extracted are marked with red dots. Exemplary electrode numbers are labeled (black circles). Seven electrodes are not visible because they are positioned on the back of the torso.

All tissues, except the ventricles and the skeletal muscle, were assumed to be isotropic within the torso. Skeletal muscle fiber orientation was created based on the highly detailed thin-section photos of the VM data set [100].

In the standard configuration, the tissue conductivities as reported by Gabriel et al. [60] at 10 Hz were used. For the skeletal muscle, an anisotropy ratio of 7 was applied as this value is frequently cited in the literature [57]. The intestine was not separated into small intestine and colon. Instead, an averaged intestine conductivity of 0.278 S/m was used. It was calculated based on medical textbook's length and diameter reports of the small intestine and colon (small intestine: length 6.7 m; \varnothing 31.5 mm / colon: length 1.5 m; \varnothing 62.3 mm). The resulting volume fractions (small intestine: 53.3% / colon: 46.7%) were multiplied with the corresponding Gabriel et al. conductivities at 10 Hz (small intestine: 0.511 S/m; colon: 0.0122 S/m).

Besides this standard conductivity configuration, different test setups (as will be described in section 5.1.3) were used to determine the changes in surface potential caused by the conductivity variations. With each of these setups, the forward calculation was performed as described in section 3.4. The potentials at the body surface were then extracted at 64 electrodes (see Fig. 5.1) on the front side and parts of the back side of the torso. To simplify further statistical analysis, the extracted signals were rearranged to an m -dimensional spatio-temporal vector Φ . For k electrodes and t time samples, the vector dimension m calculates to $m = k \cdot t$.

5.1.3 Ranking by Sensitivity and Uncertainty Analysis

The importance of a certain tissue or fluid was assessed by two different approaches. In a *sensitivity analysis*, the conductivity of one organ at a time was increased and decreased by 25% of its value used in the standard configuration (see section 5.1.2). Skeletal muscle anisotropy was varied in the same way. The influence of the specific tissue conductivity on the BSPM was assessed as the difference between the BSPM calculated at the upper and lower conductivity value.

As an alternative method, the conductivity of one organ at a time was varied between the minimal and maximal conductivity that were found in the literature (section 5.1.1). All other conductivities were set to their standard value. This way, the effect of known uncertainties in distinct conductivities on the BSPM could be evaluated. This analysis is referred to as *uncertainty analysis*.

The difference between the signals Φ_1 and Φ_2 calculated at two conductivity values σ_1 and σ_2 was determined quantitatively using the root mean square error (RMSE)

$$\text{RMSE} = \sqrt{\frac{1}{m} \cdot \sum_{i=1}^m [\Phi_1(i) - \Phi_2(i)]^2}. \quad (5.1)$$

Additionally, the signals were normalized to a maximum absolute value of 1. The RMSE of the normalized signals was calculated again and labeled $\text{RMSE}_{\text{norm}}$. The idea behind this was that, unlike the RMSE for the original signals, the $\text{RMSE}_{\text{norm}}$ for the normalized signals was not influenced by homogeneous signal amplitude scalings. $\text{RMSE}_{\text{norm}}$ was rather considered to measure changes in signal morphology or relative amplitude changes between different regions or time instants.

Finally, the linear correlation coefficient (CC) between Φ_1 and Φ_2 was calculated as an alternative measure. It is independent of amplitude scaling as well:

$$\text{CC} = \frac{1}{s_1 \cdot s_2} \sum_{i=1}^m [\Phi_1(i) - \bar{\Phi}_1] \cdot [\Phi_2(i) - \bar{\Phi}_2] \quad (5.2)$$

The arithmetic mean values are denoted $\bar{\Phi}_{1,2}$, and $s_{1,2}$ are the standard deviations of the respective signals $\Phi_{1,2}$.

5.1.4 Possible Torso Model Simplifications

To evaluate possible torso model simplifications, low-ranking organs or structures were removed from the model. The conductivity of the heart muscle was included in each simplified setup because the heart always has to be segmented to simulate excitation conduction. Additionally to the heart, the 7, 5 or 3 structures with the highest im-

portance in the RMSE-sorted (and additionally CC-sorted) sensitivity ranking were added. The resulting setups were referred to as $\text{TOP7}_{\text{RMSE}}$ ($\text{TOP7}_{1-\text{CC}}$), $\text{TOP5}_{\text{RMSE}}$ ($\text{TOP5}_{1-\text{CC}}$) and $\text{TOP3}_{\text{RMSE}}$ ($\text{TOP3}_{1-\text{CC}}$). Furthermore, the quality of the results that can be achieved with a homogeneous torso model that only contains the heart as inhomogeneity was assessed. To this end, the HOM_{RMSE} setup with no additional inhomogeneities was created (equal to $\text{HOM}_{1-\text{CC}}$).

A mean conductivity value $\bar{\sigma}$ replaced the removed organs, it represented the average conductivity within the trunk. Two different mean values were considered: $\bar{\sigma}_1$ was calculated from the weighted average conductivity over all structures in the torso. Using the conductivity values from Gabriel *et al.* at 10 Hz [60] and each organ's volume fraction within the Visible Man torso, it amounted to 0.123 S/m. $\bar{\sigma}_2$ was derived from literature values for the trunk. Measurements by Burger *et al.* [93] (0.241 S/m) and Rush *et al.* [95] (0.216 S/m) resulted in an arithmetic mean value of $\bar{\sigma}_2 = 0.229$ S/m. The quality of the simplified setups was determined by comparing them to the results of the fully inhomogeneous model which served as gold standard for this comparison. The RMSE was used as a quality measure for the TOP_{RMSE} models, and 1-CC for the $\text{TOP7}_{1-\text{CC}}$ models, respectively.

5.2 BSPM Prediction for Varying Conductivities Based on Principal Component Analysis

With the conductivity ranking described in the previous section, it was evaluated which organs had the strongest effects on the BSPM. However, no description was made of *how* the signal was actually changed. Therefore, in this section it is described how certain conductivities actually affected the BSPM and how these effects can be efficiently predicted from few sample simulations based on principal component analysis (PCA).

The PCA is used to describe the variance in data by transforming it to a new set of orthogonal basis vectors. This allows to reduce the dimensionality of the problem while minimizing the representation error [101]. It has been applied in many fields of biomedical engineering, e.g. in image processing [102]. Regarding BSPM or ECG analysis, PCA has been used to remove spatial redundancy [103], extract respiratory information [104], estimate T-Wave alternans [105], or suppress signal noise [106, 107]. For the proposed approach, we performed few sample forward calculations over a wide range of conductivities. This data was then used as input for the PCA. BSPM changes due to conductivity variations were described by a mean signal and the first PCA eigenvector scaled by a conductivity dependent PCA score.

With this relationship, missing PCA scores were interpolated and the BSPM for conductivities that were not part of the initial sample could be reconstructed [108]. The method is presented and evaluated for conductivity variations in single as well as in multiple tissues. The method is very promising especially for combined conductivity variations in more than one tissue, because it can predict the resulting BSPMs from separate forward calculations in which only one conductivity at a time is varied. In addition to the atria, the analysis was also performed on ventricular data from [108].

5.2.1 Data Source

The same torso model as described in section 5.1.2 was used to simulate body surface potentials. The electrophysiological simulation in the atria was performed on the same anatomical model as in section 5.1.2. Here, the monodomain reaction-diffusion equations together with the cell model by Courtemanche *et al.* [47] were used to calculate excitation propagation. The cell model was initialized with 60 beats at 1 Hz. Intracellular conductivities were set isotropic such that the CV was 70 cm/s in all tissue classes. Excitation in the atria was simulated for 150 ms and V_m was recorded with time steps of 1 ms. This comprised the whole atrial depolarization (P-wave).

The electrophysiological simulation in the ventricles was performed as described in [90]. The ventricular anatomical data set from the VM was interpolated to an isotropic voxel size of 0.4 mm. Fiber orientation was implemented in the left and right ventricle identically using a rule-based approach based on the measurements from Streeter *et al.* [109]. Thus, the transmurally rotating helix angle α_1 was decreased linearly from 55° at the endocardium to -75.3° at the epicardium. For the transverse angle α_3 describing the amount of fiber imbrication, a fixed value of -3° was used.

The ionic model by ten Tusscher *et al.* [110] described the dynamic electrophysiological properties of the ventricular tissue. This model describes transmural heterogeneities of the transient outward current I_{to} and the slow delayed rectifier current I_{Ks} . To account for these heterogeneous channel distributions, the ventricular walls were divided into three distinct tissue layers: endocardium 40%, midmyocardium 40%, and epicardium 20%, which is in the range reported in literature [111, 112, 113]. Changes in tissue resistivity through the ventricular walls have been reported for human and canine [112, 113]. Yan *et al.* [112] determined resistivity-scaling factors from wedge-measurements. These were used to adapt transmural conductivities in the left and right ventricle. Apart from that, larger values of the potassium conductance g_{Ks} at the apex (2x basal value) have been reported by Szentadrassy *et al.* [114]. These were integrated into the model by linearly increasing g_{Ks} towards the ventric-

ular apex similar to [115]. Between left and right ventricle, no electrophysiological distinctions were made. Activation in the ventricles was initiated with a sequence of endocardial stimulation imitating the excitation conduction system [116].

Before simulation of the ventricular activation, all parameter configurations of the electrophysiological models were pre-calculated in an uncoupled environment for 60 s with a basic cycle length of 1 s. Intracellular conductivity in the ventricles was adapted to compensate for the large voxel size of 0.4 mm and the relatively thick walls of the Visible Man ventricles. The adapted intracellular conductivity was chosen such that the average transmural conduction time amounted to approximately 30 ms [112]. In order to test if the PCA method could describe the changes in BSPM caused by tissue conductivity variations, several tissues were considered. These were blood, skeletal muscle, lungs and fat, because they belonged to the tissues with the strongest influence on the BSPM. The respective Gabriel-Gabriel (GG) conductivity values were 0.7 S/m, 0.202 S/m, 0.0389 S/m, and 0.0377 S/m [60]. To probe the prediction-technique for these tissues, forward calculations at distinctive conductivities were performed the results analyzed using PCA (see section 5.2.2.2). For each tissue, seven forward calculations were conducted over a wide range of conductivities to account for the existing conductivity uncertainties. Thus, the default GG conductivities were varied by $\pm 25\%$, $\pm 50\%$ and $\pm 75\%$. A change of $\pm 75\%$ corresponds to a ratio of 7 between the highest and lowest conductivity value. This is larger than the uncertainty ranges of 2.3 to 5.5 found in the literature for the tissues that were considered here (see Table 9.1 on page 86). For better readability, the resulting seven conductivities are in the following referred to as $\sigma_i = -75\%$, -50% , -25% , GG, $+25\%$, $+50\%$, $+75\%$.

5.2.2 PCA Analysis

The changes in body surface potential that arise from the underlying conductivity variations were quantitatively analyzed using PCA. For all four tissues (blood, muscle, lungs, and fat) the method described in this section was applied separately for atrial and ventricular data. This resulted in eight PCA decompositions altogether.

5.2.2.1 Arrangement of Spatio-Temporal Data Matrix

PCA is a statistical analysis method that detects variational patterns in data of high dimension. Given are m variables with n observations each, which are arranged in an $m \times n$ matrix \mathbf{X} . For the BSPM data, the signal at a certain electrode at a given time corresponded to a variable ($m = \text{number of electrodes} \times \text{number of time steps}$). Each variable was observed using the seven different conductivity values for the tissue under investigation ($n = 7$).

The forward calculations provided seven BSPMs from the different conductivity values, recorded at 64 electrodes at time steps $t = t_0, \dots, t_{\max}$. For every conductivity σ_i , the signals from all 64 electrodes at all time steps were concatenated into one spatio-temporal signal vector

$$\mathbf{x}_{\sigma_i} = [x_{\sigma_i}^1(t_0), \dots, x_{\sigma_i}^1(t_{\max}), \dots, x_{\sigma_i}^{64}(t_0), \dots, x_{\sigma_i}^{64}(t_{\max})]^T$$

Next, the signal vectors from the seven BSPMs ($\sigma_i = -75\%$, -50% , -25% , GG, $+25\%$, $+50\%$, $+75\%$) were combined to a signal matrix \mathbf{X} that was used as input for the PCA:

$$\mathbf{X} = \begin{pmatrix} x_{-75\%}^1(t_0) & \cdots & x_{\text{GG}}^1(t_0) & \cdots & x_{+75\%}^1(t_0) \\ \vdots & \vdots & \vdots & \vdots & \vdots \\ x_{-75\%}^{64}(t_{\max}) & \cdots & x_{\text{GG}}^{64}(t_{\max}) & \cdots & x_{+75\%}^{64}(t_{\max}) \end{pmatrix}$$

Each *column* of \mathbf{X} contained the full signal vector for one conductivity value.

5.2.2.2 PCA Decomposition

The principle of PCA is as follows: From every row in the input matrix \mathbf{X} , the mean value over all observations is calculated and stored in the m -dimensional mean vector $\hat{\mathbf{x}}$. It is subtracted from all columns of \mathbf{X} to obtain the mean-free data matrix \mathbf{X}_{mf} . From the $m \times m$ -dimensional covariance matrix

$$\mathbf{C} = \text{cov}(\mathbf{X}_{\text{mf}}) \quad (5.3)$$

the principal components \mathbf{P} are determined by solving the eigenvector problem

$$\mathbf{C}\mathbf{P} = \mathbf{P}\Lambda, \quad (5.4)$$

where \mathbf{P} and Λ are $m \times m$ -dimensional matrices. The columns $j = 1, \dots, m$ of \mathbf{P} contain the m eigenvectors \mathbf{p}_j , and the diagonal elements of Λ contain the corresponding eigenvalues λ_j (with all off-diagonal elements being 0). The magnitude of the eigenvalue λ_j describes the amount of signal variation represented by \mathbf{p}_j . Therefore, eigenvectors and eigenvalues are sorted in order of decreasing eigenvalue.

For practical reasons, the PCA is often performed more efficiently using singular value decomposition [101]. It then delivers the first $n - 1$ eigenvectors. This approach was also applied in this work based on the implementation of a modified Golub-Reinsch algorithm [117, 118] in the GNU Scientific Library [119].

5.2.2.3 Signal Reconstruction

The eigenvectors obtained from the PCA span a new orthonormal coordinate system with the origin $\hat{\mathbf{x}}$ and the base $\{\mathbf{p}_j \mid j = 1, \dots, m\}$. The input signals \mathbf{x}_{σ_i} can be expressed in the new coordinate system by superposing the new base vectors

$$\mathbf{x}_{\sigma_i} = \hat{\mathbf{x}} + \sum_{j=1}^m s_{j,i} \mathbf{p}_j. \quad (5.5)$$

The PCA scores $s_{j,i}$ are the coordinates in the new system and correspond to the entries of the score matrix $\mathbf{S} = \mathbf{P}^T \mathbf{X}_{\text{mf}}$. It is calculated by projecting the initial mean-free data onto the new coordinate system.

In many cases, however, the main amount of data variation is already described by the first few eigenvectors. For the analysis shown here, it was even sufficient to only consider the first eigenvector, because $\lambda_1 \gg \lambda_2$ as will be shown in section 9.2.1. Therefore, the signal can be reconstructed using

$$\mathbf{x}_{\sigma_i} \approx \hat{\mathbf{x}} + s_{1,i} \cdot \mathbf{p}_1. \quad (5.6)$$

The mean signal $\hat{\mathbf{x}}$ is usually different for the respective tissues. Therefore, the origin of the coordinate system was shifted to the default signal obtained from the GG conductivities, because this signal was included in the PCA input matrix for all tissues. This yielded the shifted scores $q_{1,i} = s_{1,i} - s_{1,GG}$ and the reconstruction formula

$$\mathbf{x}_{\sigma_i} \approx \mathbf{x}_{GG} + q_{1,i} \cdot \mathbf{p}_1. \quad (5.7)$$

This last step is not part of a standard PCA, but (5.6) and (5.7) are mathematically equivalent. The advantage of this shift was that it allowed to combine the results of PCAs from different tissues in section 5.2.3.

5.2.3 Signal Estimation for Arbitrary Conductivities

Equation (5.7) described how to reconstruct the *simulated* signal for each of the seven conductivities from the standard GG signal for a given setup, e.g. for atrial signals and blood conductivity variations. This is done by adding a certain “portion” of the first principal component to the GG signal. The “size” of the portion for conductivity σ_i was solely determined by the shifted score $q_{1,i}$.

In this section, the signal is estimated for *arbitrary* conductivity values between the minimal and maximal conductivity used for the simulations. This was performed first

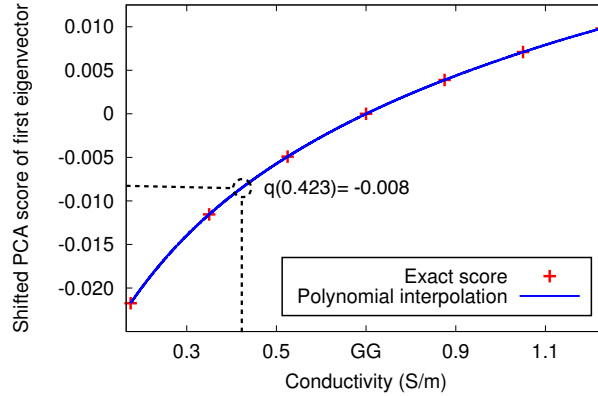


Fig. 5.2. Example for shifted scores from PCA of blood conductivity variations for the ventricular signals [108]. The PCA coordinate system was shifted such that the GG conductivity was located at the origin (shifted score q is 0). With the polynomial interpolation function, the interpolated score for any conductivity between the minimal and maximal conductivity could be calculated (e.g. for $\sigma = 0.423$ S/m, the shifted score was $q(\sigma) = -0.008$). The shifted score together with the first PCA eigenvector allowed to estimate the corresponding signal with the help of (5.8).

for one tissue conductivity that was varied and then also for combined conductivity variations in several tissues.

Signal estimation for variations in one tissue

Fig. 5.2 shows an example of shifted scores for the seven blood conductivities during the QRS-complex. Because the scores were monotonically dependent on the conductivities, a polynomial interpolation function $q(\sigma)$ was calculated in the range $\sigma_1 = -75\%$ to $\sigma_7 = +75\%$. It established a bijective relation between conductivity σ and shifted score q . The signal \mathbf{x} for an arbitrary conductivity σ was then predicted by the relation

$$\mathbf{x}(\sigma) \approx \mathbf{x}_{GG} + q(\sigma) \cdot \mathbf{p}_1. \quad (5.8)$$

Signal Estimation for Variations in Several Tissues

The PCAs for the four different tissues blood, muscle, lungs, and fat resulted in the interpolated score curves $q(\sigma)$ and first eigenvectors \mathbf{p}_1 for each tissue. These were denoted with the respective indices B, M, L, and F, e.g. $q_B(\sigma_B)$ and $\mathbf{p}_{1,B}$ for blood. The prediction of the BSPM signal for combined conductivity variations was then performed as follows:

$$\begin{aligned}
\mathbf{x}(\sigma_B, \sigma_M, \sigma_L, \sigma_F) \approx & \mathbf{x}_{GG} + q_B(\sigma_B) \cdot \mathbf{p}_{1,B} \\
& + q_M(\sigma_M) \cdot \mathbf{p}_{1,M} \\
& + q_L(\sigma_L) \cdot \mathbf{p}_{1,L} \\
& + q_F(\sigma_F) \cdot \mathbf{p}_{1,F}
\end{aligned} \tag{5.9}$$

This implied the hypothesis that the effect of combined conductivity variations of several tissues could be described as superposition of signal changes caused by separately varying the single conductivities.

5.2.4 Validation

As a first validation step for this methodology, the ratio between the first and second eigenvalue of each PCA decomposition was compared. This ensured that it was tolerable to reconstruct the signal from the first eigenvector only.

Furthermore, the first eigenvectors from the PCAs for the four tissues were not necessarily orthogonal, therefore the pairwise angles between them were calculated. They are a measure of how independent changes caused by different tissues were. Pairwise angles were calculated separately for atria and ventricles.

Subsequently, BSPM signals for different conductivities of one tissue were reconstructed using the *exact* shifted PCA scores, with only the first eigenvector according to (5.7). Then, the root mean squared error (RMSE) was calculated between the reconstructed and the original forward-calculated signal which provided the reference. This RMSE could assess possible errors that were due to the omission of the second and successive eigenvectors. The process is summarized in Fig. 5.3(a).

The simulated signals mainly comprised the relevant parts in the cardiac cycle (150 ms of atrial depolarization and 400 ms of ventricular de- and repolarization). Therefore, the RMSE reflected the relevant errors that could be introduced.

The error that originated from the PCA score interpolation was assessed by a leave-one-out validation. In this case, one input signal at a specific conductivity was deliberately omitted from the PCA (see Fig. 5.3(b)). Then, the interpolation technique was used to derive the associated *interpolated* score. The BSPM signal was reconstructed from this score and compared to the original signal by calculating the RMSE. This addressed the combined error introduced by both the omission of the second and successive eigenvectors and the score interpolation.

Finally, it was tested if the PCA method could reconstruct simultaneous conductivity variations in all four tissues. To this end, the signals were estimated for the cases in which all four conductivities were either increased or decreased by 25%. All possible $2^4=16$ combinations were reconstructed using (5.9). Additional 16 forward calcu-

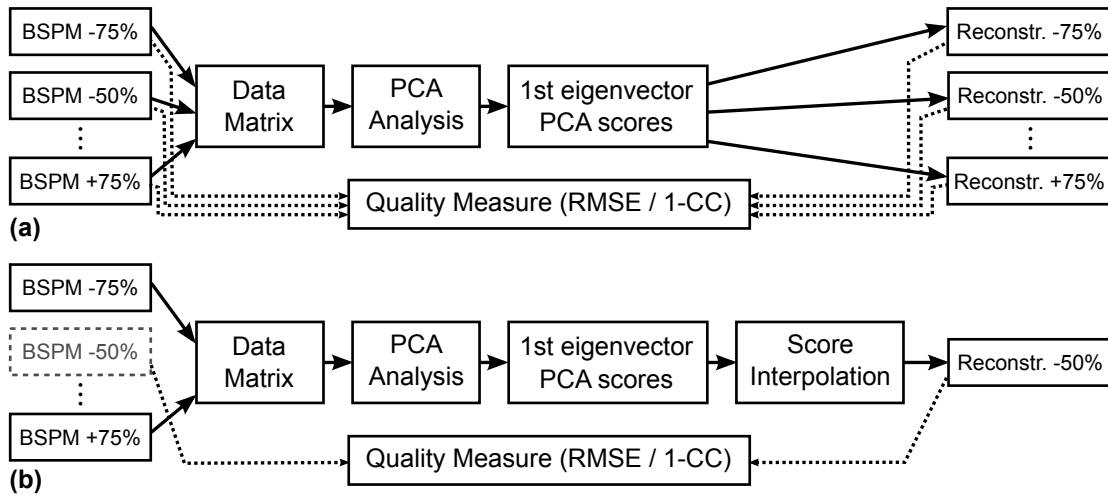


Fig. 5.3. PCA reconstruction and validation for single tissue conductivities. (a) Reconstruction from exact scores. The simulated BSPMs with the conductivity values from -75% to $+75\%$ were arranged in the PCA input data matrix. After the PCA analysis, the first PCA eigenvector and the shifted PCA scores were used to reconstruct the different input signals from the GG signal. Then, the reconstructed signals were compared to the respective input signals with the RMSE or CC. (b) Reconstruction from interpolated scores. In a leave-one-out validation, one conductivity at a time was omitted in the data matrix (here -50%). After the PCA analysis, the score function was interpolated to determine the score for the omitted conductivity. The signal that was reconstructed from the interpolated score was then compared to the input signal to determine the interpolation error.

lations with the combined conductivity variations were performed as a reference. Finally, the RMSE between the reconstructed signal and the simulated reference was calculated. It was used to evaluate the assumption that combined conductivity variations of several tissues could be predicted by superposing the changes introduced by a single tissue separately. This procedure was repeated for larger variations of $\pm 50\%$, respectively.

5.2.5 Confidence Intervals

It can be assumed that for a given model, e.g. for a specific patient, there exist best-guess conductivity values that however contain some measurement uncertainty. The question in this case is: How large are the possible deviations in the BSPM or ECG signal if the true σ value for a certain tissue lies somewhere between the uncertainty boundaries? The upper and lower signal boundary can then be regarded as confidence interval for the signal.

The ECG signal could be predicted over the full range of simulated conductivity values as described in section 5.2.3. If upper and lower boundaries for each conductivity were given, the minimum and maximum possible signal value between these boundaries at each time step could be determined. In this work, the best-guess values

were the GG conductivity values, for which a relative uncertainty $\delta\sigma_{\text{rel}}$ was assumed. Here, the confidence interval for simultaneous uncertainties $\delta\sigma_{\text{rel}} = \pm 10\%$, $\pm 30\%$, and $\pm 50\%$ in all four tissues was calculated.

The uncertainties in clinical *bipolar* ECG leads are of special interest, therefore the minimum and maximum bipolar signals of the Einthoven II lead were evaluated exemplarily.

Quantitative Analysis of Electrophysiological Data

This chapter presents methods that allow for quantitatively analyzing data from intracardiac electrophysiological (EP) studies. Such data are frequently acquired during routine interventions. Because they contain valuable information for model personalization and validation, quantitative analysis techniques were developed.

Catheter electrogram recordings were analyzed for local activation times. A cosine fit method was developed to calculate the incidence direction and conduction velocity for the activation times from a single wavefront passing a circular mapping catheter as reported in [120]. Additionally, a more general approach based on activation time interpolation using radial basis functions (RBFs) was implemented. It was proposed in [84] together with tests on simulated data. Furthermore, electrograms recorded in the coronary sinus were analyzed in terms of the general propagation direction.

These analysis methods were then applied to clinical electrogram recordings to analyze incidence direction and conduction velocity. Finally, changes in CV for decreasing pacing cycle length were analyzed to estimate patient-individual CV restitution curves. The results will be presented in chapter 10.

6.1 Cosine Fit

Circular mapping catheters are often used during EP studies in patients suffering from atrial arrhythmias. In this section, a data model is presented that calculates the incidence direction and CV from the activation pattern of a single wavefront passing a circular catheter. The presence of single wavefronts is a valid assumption for both sinus rhythm and several arrhythmic conditions, such as atrial flutter or ectopic atrial tachycardias.

First, the activation time in each channel is determined, then, a cosine data model is numerically fitted to the detected activation times. To validate the method, simula-

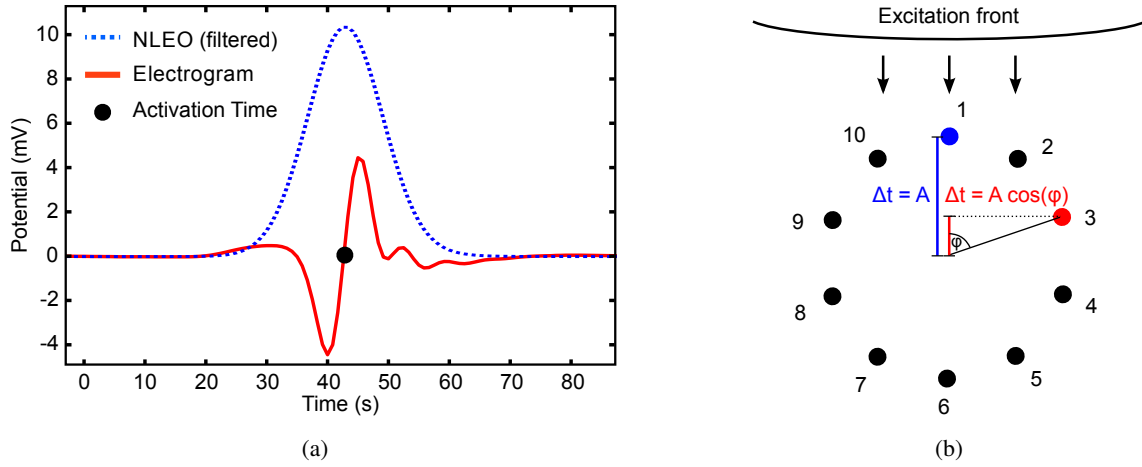


Fig. 6.1. Analysis of intracardiac electrograms. (a) Example activation time detection with NLEO analysis. The Gauss-filtered NLEO signal was rescaled, but because the barycenter is determined, the absolute value of the signal does not influence detection of the activation time. (b) Schematic derivation of cosine data model for activation pattern. An almost plane excitation front hits the catheter from above. Because the electrodes are arranged on a circle, their activation time delays with respect to the catheter center are described by a cosine function.

tions in a 2D tissue patch are performed and artificial noise is added to test the model accuracy.

6.1.1 Activation Time Detection

The activation time in each electrogram (EGM) was determined with the help of a non-linear energy operator (NLEO). It was proposed by Teager and Kaiser [121] and has been demonstrated to be an effective analysis method for intracardiac electrograms [122, 40].

From a signal x_j , the operator calculates the non-linear energy E_j at each sample j as

$$E_j = x_j^2 - x_{j+1}x_{j-1}. \quad (6.1)$$

The resulting energy signal E_j was filtered using a Gaussian low pass filter with a cut-off frequency of 24 Hz at -3 dB. The barycentric median of the filtered energy signal was then determined as the activation time in the EGM. An example is shown in figure 6.1(a).

This procedure was repeated for each EGM in the catheter recording, resulting in the activation times $t(n)$. For bipolar EGMs, $n = 1.5, 2.5, \dots$ denoted the virtual, half-integer “electrode numbers” for the EGMs 1-2, 2-3, ..., respectively.

6.1.2 Data Model

If a plane excitation wave front travels across a circular catheter, this results in a sinusoidal activation pattern (Figures 6.1(b) and 6.2). Therefore, the activation pattern $t(n)$ in the n catheter electrodes is described as a cosine function

$$t(n) = t_c - A \cdot \cos[\varphi(n) - \varphi_0]. \quad (6.2)$$

Here, t_c is the center activation time (base line of the cosine function), A is the time amplitude of the cosine function, $\varphi(n)$ is the angle at which electrode n is placed, and the phase shift φ_0 corresponds to the angle at which the earliest activation occurs. φ was defined relative to electrode 1, i.e. $\varphi(1) = 0^\circ$. If a parameter γ is introduced that describes the angle offset between two neighbour electrodes, then φ could be written as $\varphi(n) = \gamma \cdot (n - 1)$ (bipolar electrograms are virtually placed at the point between the electrodes, e.g., EGM 1-2 is recorded between electrodes 1 and 2 at $\varphi(1.5) = \gamma/2$). Thus, (6.2) becomes

$$t(n) = t_c - A \cdot \cos[\gamma \cdot (n - 1) - \varphi_0]. \quad (6.3)$$

The parameters t_c , A , γ and φ_0 could then be determined by fitting (6.3) to any detected set of activation times. For this, a sequential quadratic programming algorithm implemented in Matlab was used. The initial values and boundaries for t_c , A , and φ_0 were estimated from the activation sequence. A best-guess for γ was either known from the catheter parameters for simulated data or derived from the mapped positions for the clinical data (see section 6.5.2.2).

The incidence angle φ_0 gave the incidence direction of the wave and therefore represented the wave direction. The local CV at the measurement position was calculated from the catheter radius r and the cosine amplitude A as $CV = r/A$. Finally, the fit residual was calculated as the sum of squared deviations between fitted and measured time at each data point.

6.1.3 Patch Validation

The cosine fit algorithm was first tested on synthetic intracardiac EGMs. These were derived from a patch simulation ($301 \times 301 \times 5$ voxels with 0.33 mm voxel size). Stimulation sites were located around the patch center at angles in 10° intervals (see Fig. 6.2(a) for example) and at a distance of 50 mm. This resulted in 36 setups with 36 different stimulation points. For these setups, intracardiac EGMs in a virtual catheter at the patch center were simulated in the following way.

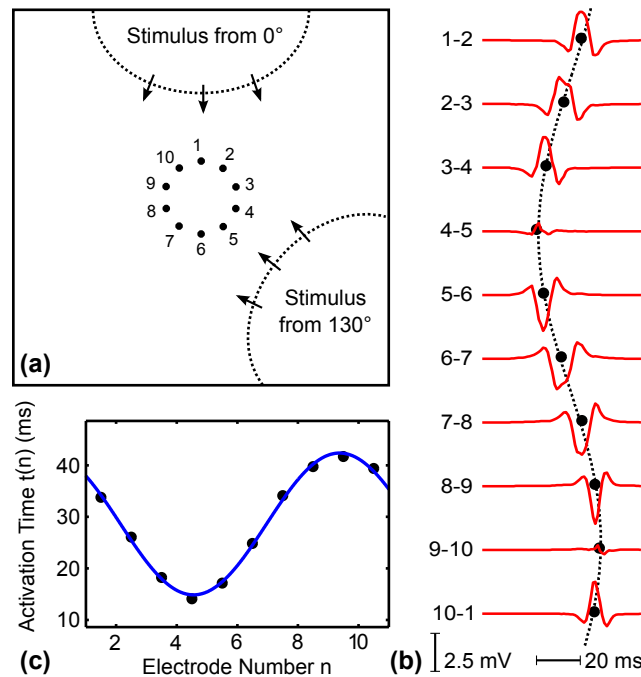


Fig. 6.2. Simulation and analysis of intracardiac EGMs in a tissue patch [120]. (a) Schematic patch setup. The circular mapping catheter with 10 electrodes was placed in the center of the patch. All angles were measured clockwise relative to electrode 1 that was aligned with the y-axis. 36 stimuli were initiated at 10° intervals. Two example stimuli at 0° and 130° are illustrated. (b) Simulated bipolar EGMs (potential differences between neighbour electrodes) for the 130° stimulus. Black dots represent the detected activation times. The fitted cosine curve is marked with a dotted line. (c) Detailed plot of activation times as a function of electrode number. The times were assigned to half-integer electrode numbers as *bipolar* EGMs were analyzed.

Transmembrane voltages V_m for the 36 setups were simulated using the cellular automaton. The CV was set to 70 cm/s (within the range reported for atrial tissue in [15]). Due to the rule-based architecture of the automaton, the CV is independent of e.g. wavefront or tissue curvature and thus provides a well-known reference.

The extracellular potentials Φ_e that the catheter measures were derived using a forward calculation on a tetrahedron representation of the patch, embedded in blood. Before the actual forward calculation, a circular mapping catheter had been inserted into the model at the patch center. It comprised ten equally-spaced electrodes and had a radius of 10 mm. The electrodes were represented by metallic spheres of 1 mm radius. The signal for each electrode was then recorded at the sphere center for 60 ms with a sampling frequency of 1000 Hz while the wavefront passed the catheter. The synthetic bipolar EGMs were calculated from the signal difference of two neighbour electrodes. The EGMs were artificially prolonged with 50 ms of zero signal at both ends. This ensured a correct signal analysis.

Stability Analysis

To prove the stability of this algorithm against misdetections in the activation times, random errors were applied to the detected times from the patch simulation. This covered all possible error sources that could lead to errors in the detected activation times. If, in contrast, signal noise was added to the electrograms, this would neglect other potential influences such as local signal distortions, small catheter deformations, and even other unexpected factors. Therefore, the noise is added directly to the activation times, where all such error sources would manifest. Gaussian noise with different standard deviations σ was used. This was repeated 1000 times for each angle and each σ value. The σ values were chosen based on the approximate cosine amplitude $A = 14$ ms for the catheter radius of 10 mm and the CV of 70 cm/s. Then, σ values of 5%, 10%, 15%, and 20% of A were used to calculate the noise offsets. Thus, the 3- σ range covering 99% of the deviations amounted to 15%, 30%, 45%, and 60% of A , respectively.

For the simulated catheter in the patch, $\gamma = 36^\circ$ is exactly known. For clinical measurements, this is generally not the case because many catheters are variable in diameter while the electrode spacing is constant. Therefore, the sensitivity of the algorithm to the allowed variation in γ was evaluated. From clinical data, the overall angle covered by ten catheter electrodes can be estimated from the recorded positions. It was assumed that this error normally does not exceed 20° in total, which corresponds to 2° per electrode. Therefore, each of the above-described analyses was repeated with $\delta\gamma$ values in that range, which were 1° , 2° , and 3° .

For each of the 36 stimulation setups, this resulted in 12 parameter combinations (4 σ values \times 3 $\delta\gamma$ values) that were tested 1000 times. This way, a total number of 432,000 parameter estimations were performed. For each of the 12 parameter combinations, 36,000 results (36 stimuli \times 1,000 tests) were analyzed regarding the mean angle error, the 95-quantile of the angle error and the mean fit residual. The 95-quantile corresponds to the error that was not exceeded by 95% of the calculated angles. The mean fit residual was further calculated for the four σ values from all parameter estimations including different $\delta\gamma$ values.

Furthermore, the algorithm was tested on data where two wavefronts collided under the catheter. To this end, two synchronous stimuli were set at 0° and 210° . For this setup, the cosine function no longer is a valid data model. The fit residual was compared to the average fit residuals of the single wavefronts with noise added in order to determine how the parameter estimation responded in such cases.

6.2 RBF Interpolation

In the cosine fit analysis presented in section 6.1, a spatio-temporal relationship was established between the measurement position and the local activation time (LAT) at that point. With a data model especially designed for a plane wave front passing a circular mapping catheter, the incidence direction and conduction velocity could be estimated.

However, there may be different situations, such as measurements with other catheter types or activation patterns (e.g. colliding wavefronts), that cannot be resolved with the cosine fit method. Therefore, a more general approach as proposed by Masè et al. [84] is the following: First, from the measured LATs, the LAT field at every point in the catheter area is interpolated. Then, the interpolated LAT field is quantitatively analyzed.

The interpolation is performed using radial basis functions (RBFs), a so-called “mesh-free interpolation” [123]. This means it can be used to reconstruct an unknown function (here, the LAT field) from scattered and sparse data as is the case with the catheter measurements. RBF interpolation is further used in, for example, geophysics, computer graphics, or economics.

6.2.1 Mathematical Background

Some mathematical aspects have to be considered when using the RBF interpolation. Section 6.2.1.1 introduces different types of radial basis functions. Section 6.2.1.2 describes how RBFs can be used to interpolate activation time fields. Finally, section 6.2.1.3 covers the analysis of the interpolated fields in terms of conduction direction and velocity.

Table 6.1. Common radial basis functions and their properties [124].

Name	ϕ	Type
Gaussian	$e^{-\frac{1}{2}(\frac{r}{\sigma})^2}$	Positive definite
Linear	$ r $	Conditionally positive definite
Cubic	$ r^3 $	Conditionally positive definite
Thin-plate splines	$r^2 \log(r+1)$	Conditionally positive definite
Multiquadrics	$\sqrt{1 + \frac{r}{\sigma}}$	Conditionally positive definite

6.2.1.1 Definition and Function Types

A radial basis function $\phi(r)$ depends only on one variable, which is the distance r from its origin

$$\phi(r) = \phi(\mathbf{x}) = \phi(\|\mathbf{x}\|), \quad (6.4)$$

or from a defined “center” point \mathbf{c}

$$\phi(r) = \phi(\mathbf{x}, \mathbf{c}) = \phi(\|\mathbf{x} - \mathbf{c}\|). \quad (6.5)$$

The norm used in this work is the Euclidean Distance, although other distance functions are possible. Several RBF types exist, an overview is given in Table 6.1.

6.2.1.2 Interpolation of the Activation Time Field

The unknown activation time field $T(\mathbf{x})$ is reconstructed by a superposition of translates $\phi(\|\mathbf{x} - \mathbf{x}_k\|)$ of a specified RBF

$$T(\mathbf{x}) = \sum_{k=1}^N \lambda_k \phi(\|\mathbf{x} - \mathbf{x}_k\|), \quad N \in \mathbb{N} \quad (6.6)$$

which is the so-called trial function. The N translations \mathbf{x}_k are the RBF centers which represent the N points at which data were measured. With the measured function values $\mathbf{f}(\mathbf{x}_k) = [f(\mathbf{x}_1), f(\mathbf{x}_2), \dots, f(\mathbf{x}_N)]^T$ at these points, the coefficients λ_k are calculated such that the trial function exactly reproduces the measured values at the function centers. This results in solving the linear system $\Phi \cdot \lambda = \mathbf{f}$ as follows:

$$\begin{pmatrix} \phi(\|\mathbf{x}_1 - \mathbf{x}_1\|) & \phi(\|\mathbf{x}_1 - \mathbf{x}_2\|) & \cdots & \phi(\|\mathbf{x}_1 - \mathbf{x}_N\|) \\ \phi(\|\mathbf{x}_2 - \mathbf{x}_1\|) & \phi(\|\mathbf{x}_2 - \mathbf{x}_2\|) & \cdots & \phi(\|\mathbf{x}_2 - \mathbf{x}_N\|) \\ \vdots & \vdots & \ddots & \vdots \\ \phi(\|\mathbf{x}_N - \mathbf{x}_1\|) & \phi(\|\mathbf{x}_N - \mathbf{x}_2\|) & \cdots & \phi(\|\mathbf{x}_N - \mathbf{x}_N\|) \end{pmatrix} \begin{pmatrix} \lambda_1 \\ \lambda_2 \\ \vdots \\ \lambda_N \end{pmatrix} = \begin{pmatrix} f(\mathbf{x}_1) \\ f(\mathbf{x}_2) \\ \vdots \\ f(\mathbf{x}_N) \end{pmatrix} \quad (6.7)$$

$\Phi_{j,k}$ is given as

$$\Phi_{j,k} = \phi(\|\mathbf{x}_j - \mathbf{x}_k\|) \quad 1 \leq j, k \leq N. \quad (6.8)$$

To ensure solvability, the system matrix Φ must be non-singular. One possible way for achieving this is to use positive definite RBFs according to the following definition [125]:

Definition 6.1. A radial basis function ϕ on $[0, \infty)$ is positive definite on \mathbb{R} , if for all choices of sets $X := \{x_1, \dots, x_m\}$ of finitely many points x_1, \dots, x_m and arbitrary m , the symmetric $m \times m$ matrices Φ_X are positive definite.

However, as can be seen in table 6.1, many RBF types are not positive definite. For interpolations with such RBFs, additional polynomials are added [124]. In this work, linear polynomials (i.e. maximal order 1) were used. In the two-dimensional case of the LATs with $\mathbf{x} = (x, y)$, this resulted in $M = 3$ polynomials: $p_1(\mathbf{x}) = 1$, $p_2(\mathbf{x}) = x$ and $p_3(\mathbf{x}) = y$.

Thus, the new general trial function can be written as

$$T(\mathbf{x}) = \sum_{k=1}^N \lambda_k \phi(\|\mathbf{x} - \mathbf{x}_k\|) + \sum_{l=1}^M d_l p_l(\mathbf{x}), \quad \mathbf{x} \in \mathbb{R}^2. \quad (6.9)$$

p_1, \dots, p_M span the basis of the M -dimensional linear space of polynomials. Requiring that $T(\mathbf{x}_k) = f(\mathbf{x}_k)$ be valid also for the new trial function leads to a new linear equation system with M additional degrees of freedom. To solve the new system, M additional conditions are added

$$\sum_{k=1}^N \lambda_k p_l(\mathbf{x}_k) = 0, \quad l = 1, \dots, M, \quad (6.10)$$

which lead to a unique solution [124].

Thus, the linear system to be solved now can be written as

$$\begin{pmatrix} \Phi & P \\ P^T & O \end{pmatrix} \begin{pmatrix} \lambda \\ \mathbf{d} \end{pmatrix} = \begin{pmatrix} \mathbf{f} \\ \mathbf{0} \end{pmatrix}, \quad (6.11)$$

where $P_{jl} = p_l(\mathbf{x}_j)$ with $j = 1, \dots, N$, $l = 1, \dots, M$ form the matrix P of polynomial function values at the RBF centers, $\mathbf{d} = (d_1, \dots, d_M)^T$ is the vector of polynomial coefficients, $\mathbf{0}$ is a zero vector of length M , and O is an $M \times M$ zero matrix.

6.2.1.3 Analysis of the Activation Time Field

The interpolated LAT field as a function of position $T(x, y)$ can then be analytically analyzed in terms of propagation direction and conduction velocity as described in [82]. The gradient vector $\nabla T = [\frac{\partial T}{\partial x}, \frac{\partial T}{\partial y}] = [\partial_x T, \partial_y T]$ is always normal to the local isochrone. Thus, it defines the direction of propagation. It can also be regarded as “slowness-vector”, because high values correspond to large changes in time over small distances in space, i.e. a slow conduction.

The actual CV is derived from the LAT field as follows. Because the gradient is normal to the isochrone, the components of a differential vector $(dx, dy)^T$ always satisfy the equation

$$\frac{dy}{dx} = \frac{\partial_y T}{\partial_x T} \quad \text{or} \quad dy = \frac{\partial_y T}{\partial_x T} dx. \quad (6.12)$$

Between two points on the surface $T(x, y)$ separated by $(dx, dy)^T$, the following identity holds:

$$dT = \partial_x T dx + \partial_y T dy = \left(\partial_x T + \frac{(\partial_y T)^2}{\partial_x T} \right) dx. \quad (6.13)$$

From this, the velocity v_x along the x direction can be determined as

$$v_x = \frac{dx}{dT} = \frac{\partial_x T}{(\partial_x T)^2 + (\partial_y T)^2}. \quad (6.14)$$

The y -component v_y is calculated analogously, so the velocity vector field is determined as

$$\mathbf{v} = [v_x, v_y] = \left[\frac{dx}{dT}, \frac{dy}{dT} \right] = \left[\frac{\partial_x T}{(\partial_x T)^2 + (\partial_y T)^2}, \frac{\partial_y T}{(\partial_x T)^2 + (\partial_y T)^2} \right]. \quad (6.15)$$

6.2.2 Analysis of EP Measurements

A single wavefront detected in a circular mapping catheter could be analyzed as follows. The LATs in all channels were determined with the NLEO as for the cosine fit. The electrode positions were part of the NavX data and thus known. The spatial positions \mathbf{x} for the RBF interpolation were chosen as the points between the two electrodes that delivered one bipolar EGM channel.

The RBF coefficients were determined by solving the linear system (6.11). Next, the LAT field was reconstructed according to (6.9) on a numerical rectangular grid with a resolution of 0.1 mm. The grid size was chosen such that it covered the catheter electrodes. The local velocity vector was then calculated numerically at each grid point according to (6.15).

From the velocity vectors at all grid points, the mean propagation direction and conduction velocity were calculated. The standard deviations of all angles or CVs *within one LAT field* are a measure of the field inhomogeneity and thus of the interpolation quality. It is in this work referred to as *angle spread* or *CV spread*, respectively.

To account for regions of local stationary LAT values (i.e. local maxima) that could cause very low numerical gradients and therefore very high CV values, grid points with unphysiologically high CVs above 200 cm/s were excluded from the analysis.

6.2.3 Validation

The RBF interpolation analysis method was validated and the quality of the results was compared to the cosine fit algorithm. To this end, RBF interpolation was applied to the same simulated data with artificial noise that was used for validation of the cosine fit (see section 6.1.3 for details). It must be noted that exactly the same activation times (including the same noise representation) were fed into the RBF analysis for comparison. The interpolation centers were placed between two neighbour electrodes.

6.2.4 Detection of Two Colliding Wavefronts

It is possible that two wave fronts collide under the circular mapping catheter during the measurement. Then, it would be desirable to detect such a collision. Wavefront collision is characterized by two regions of velocity vectors that (at least partially) point into opposite directions. At the border between these regions, this results in a high negative value of the divergence, corresponding to a sink. Therefore, wavefront collision was determined by analyzing the divergence of the velocity vector field

$$\operatorname{div} \mathbf{v} = \nabla \cdot \mathbf{v} = \frac{\partial v_x}{\partial x} + \frac{\partial v_y}{\partial y}. \quad (6.16)$$

Like the CV, the divergence was numerically calculated using finite differences on the 0.1 mm grid.

To find a line of high divergence, the Radon transformation was used. In contrast to other line finding algorithms (such as a linear least-squares fit or the Hough transformation), the Radon transformation can easily be applied to non-binarized data and is not sensitive to outliers. Furthermore, in the interpolated LAT field, there often was no real line but just spots of high divergence along that line. The Radon transformation was therefore easy to implement and has been used for line detection before [126, 127].

Once a split line was found, two analysis approaches were tested: First, the existing LAT field could be analyzed on both sides of the split line separately. Second, two new interpolations could be carried out including only the centers from the respective sides. The advantage of the new interpolation is that in the original interpolation, smoothing effects appear at the collision line with local conduction vectors along the line. With separate interpolation for the respective sides, these effects disappear. On the other hand, the reduced number of centers for the split interpolation makes the

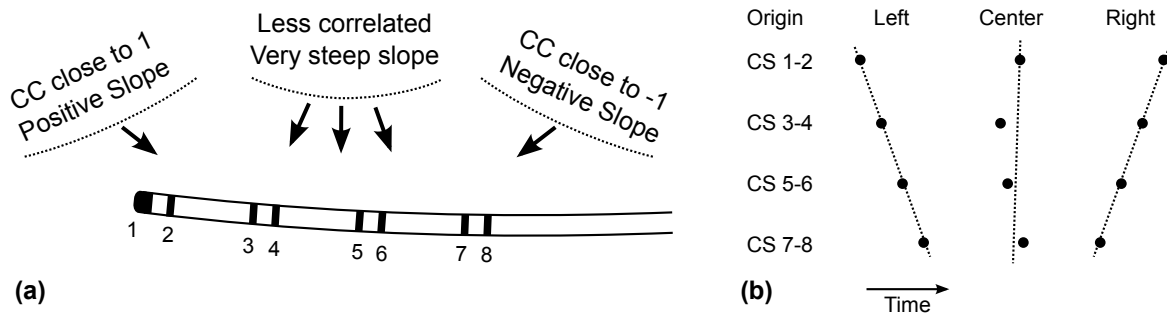


Fig. 6.3. Analysis techniques for CS signals. (a) Wavefronts that activate the CS catheter from distal end, center, and proximal end. Wave fronts that first activate the distal end (CS 1-2) and then uniformly travel along the catheter result in a CC close to +1 and a positive linear slope. Wave fronts that first activate the proximal end (CS 7-8) and then travel along the catheter in the opposite direction lead to a CC close to -1 and a negative linear slope. If fronts first activate the catheter center and then travel towards both catheter ends, the CC value will be closer to 0 (e.g. between -0.5 and +0.5) and the linear slope will be very steep (with either positive or negative values). (b) Corresponding activation patterns with linear fits (schematic). Note that the data were arranged as they can be observed when EGM recordings are displayed, i.e. with a horizontal time axis. In the CS analysis, however, the pair number actually corresponded to the x -axis and the time to the y -axis, so that activations from the left side had a positive CC or slope m .

method more sensitive to detection errors. It is only suitable if a sufficient number of centers is present in the initial interpolation.

6.3 Analysis of Coronary Sinus Signals

During the EP study, a stationary mapping catheter is placed in the coronary sinus (CS). The catheter used in the clinical measurements analyzed in this work comprised four electrode pairs with an electrode spacing of 2 mm and a distance between the pairs of 5 mm. Because the location does not change significantly during the study, the electrograms from the CS can be used to compare different sections of the studies with respect to atrial activation rate, propagation direction etc.

In this section, two quantitative analysis methods are introduced that determine if the activation along the CS occurs from the proximal to the distal end or vice versa. To this end, the activation times $t(n_p)$ in the electrode pairs $n_p = 1, \dots, 4(, 5)$ (from distal to proximal) are determined with the NLEO operator described in section 6.1.1. They are further analyzed using a linear correlation coefficient and a linear least-squares fit.

6.3.1 Linear Correlation Coefficient

The linear correlation coefficient (CC) according to Pearson between two variables X and Y with standard deviations σ_X and σ_Y is defined as

$$r_{X,Y} = \frac{\text{cov}(X,Y)}{\sigma_X \sigma_Y}. \quad (6.17)$$

Its value is between +1 for absolutely correlated data and -1 for absolutely anti-correlated data (A value of 0 means that there is no linear correlation between X and Y , while other, non-linear, correlations still may exist).

For the CS data, the correlation coefficient was calculated between pair number n_p and the corresponding activation time $t(n_p)$. A value close to +1 represented an almost linear increase of activation time with pair number and corresponded to a wave front that first activated the distal end. A value close to -1 meant an activation starting at the proximal end, such as typical during NSR. Examples are shown in Figure 6.3.

6.3.2 Linear Fit

The activation pattern was further fitted to a linear equation

$$t(n_p) = m \cdot n_p + t_0 \quad (6.18)$$

with slope m and center activation time t_0 by linear regression. The slope m also was an indicator for the direction of propagation. As for the CC, negative values resulted from right-to-left conduction whereas positive value corresponded to left-to-right conduction. However, the CV cannot be estimated from m , because for wave fronts that do not run along the catheter but rather hit it under a certain angle, as normally is the case, the CV will be overestimated.

6.4 Electrogram Simulation and Analysis in a Realistic Atrial Data Set

To bridge the gap between patch simulations and clinical measurements, intracardiac EGMs were also simulated in the realistic Visible Man atria [128] as described in [129]. The same computational setup as for the patch validation (section 6.1.3) was used.

A circular mapping catheter was placed in the simulation model on the left atrial roof at approximately equal distances to all four PV ostia. To this end, a projection method [130] was used as follows: The number of electrodes (10), the catheter radius (7.5 mm) and a center point at some distance from the heart wall were specified. There, inside the atrium, a temporary set of electrodes was created. Using a second point, the direction towards the tissue was specified. Then, each electrode was projected onto the boundary between blood and tissue to ensure wall contact for each

electrode. Details about the projection method can be found in [130]. Further, a decapolar deflectable catheter was manually placed in the CS. The five electrode pairs had an electrode spacing of 1.5 mm and 9 mm distance between the pairs.

Simulations were performed with the cellular automaton that was initialized with two sinus beats at a cycle length of 800 ms. Data for NSR were taken from the third beat. Furthermore, stimuli in all four PVs were simulated. They were initiated 100 ms before the following sinus beat to ensure that no tissue was refractory and that wavefronts from the PV stimuli did not collide with NSR on the LA roof.

Intracardiac EGMs were simulated in the LA roof circular catheter with the different PV stimuli sites and during NSR. They were then analyzed with the cosine fit method described in section 6.1.2. The EGMs had a sampling frequency of 1000 Hz and were 150 ms long. From the incidence angle, the origin of the stimulus was estimated. Additionally, the CV was calculated and compared to the simulated value of 70 cm/s. The data from the CS catheter was analyzed as described in section 6.3 with respect to linear slope and CC.

6.5 Analysis of Patient Data

The analysis methods presented in this chapter were applied to clinical data from Städtisches Klinikum Karlsruhe. Data were acquired during EP studies in patients suffering from atrial arrhythmias. For AF patients, a CT scan with contrast enhancement in the LA and the PVs was routinely acquired the day before the examination and was available in DICOM format. Normally, the cosine-fit analysis was applied, however, for a case with suspected wavefront collision and measurement with an AFocusII spiral catheter, RBF interpolation was used.

6.5.1 Details of Electrophysiological Data

The seven patients under study suffered from paroxysmal AF (six patients) or focal right atrial (RA) tachycardia (one patient) and underwent an EP study for catheter ablation. An overview of available patient data is given in Table 6.2 on page 69. The data segments analyzed for each patient are listed together with the measurement site and a description of the analyzed data.

The following catheters were introduced via a right femoral vein access: a mapping catheter (10-electrode circular mapping catheter of type Inquiry Optima, St. Jude Medical, or Lasso 2515, Biosense Webster; in patient 7, a St. Jude AFocus II spiral catheter), an ablation catheter (Cool Path Duo, St. Jude Medical), and an octopolar

catheter (EP-XT, Bard Electrophysiology, Lowell, USA) for stationary placement in the CS. The proximal electrode pair of the CS catheter was normally located close to the CS orifice and the distal pair at the inferolateral wall. Catheter electrode numbering started in the distal electrode. Pacing pulses could be applied from the CS catheter or the tip of the ablation catheter using a Biotronik UHS 3000 stimulator (5 V, 1 ms pulse width). Pacing was performed such that 1:1 capture was present. Patients were off antiarrhythmic agents for more than five half time periods at the time of the EP study.

All data were retrospectively extracted from an EnSite NavX electroanatomical mapping system (St. Jude Medical) for offline analysis. A whole EP study could manually be subdivided into so-called segments during the examination. After data export, each data segment consisted of two parts, one containing recorded electrograms and another one containing the static anatomical geometry of the atria as well as the catheter positions at each time during the measurement.

In detail, the electrogram part typically contained the following recordings with a sampling frequency of 1200 Hz:

- Bipolar electrograms from mapping catheter (Optima 7-7 / Lasso 2515 with 10 electrodes or AFocus II with 20 electrodes)
- Bipolar electrograms from CS catheter with 8 electrodes (4 pairs with 2 electrodes each)
- Bipolar electrograms from mapping/ablation catheter
- ECG recording

The geometry part consisted of

- The 3D positions of all catheter electrodes at every 13th time step in the electrogram data
- The static surface geometry of the patient's atrium that was mapped with the circular mapping catheter at the beginning of the examination (containing RA or LA depending on arrhythmia type; LA geometries included the PV ostia and the LAA with separate labels).

For most EP studies in the LA, the static geometry recorded with the NavX system was semi-automatically registered with the atrial CT scan by the physician directly after it had been recorded. To this end, defined landmark points were selected in both geometries and further processed by the EnSite system (so-called Fusion). As a result of this process, the coordinate system of an EnSite geometry was adjusted to match the CT coordinate system.

6.5.2 Data Analysis

The clinical data were analyzed with the cosine fit and (for measurements without CS pacing) the CS analysis methods. Furthermore, some test applications of the RBF interpolation were performed. Compared to the analysis of simulated data, additional solutions had to be found for the clinical data regarding:

- Detection of single wavefronts in the continuous EGM recordings
- Analysis of the electrode positions to determine initial values for γ (cosine-fit) or to set up the coordinate system for RBF interpolation
- Suppression of far-field signals originating from pacing electrodes during stimulation

These techniques are described in the following sections.

6.5.2.1 Detecting Wavefronts in Continuous EGM Recordings

Wavefront detection was performed in the complete set of electrograms from one catheter using a moving window (width typically 125-200 ms). At the current window position, all channels exceeding a voltage amplitude threshold were marked active (threshold typically 0.3-2 mV). If the number of active channels was large enough (3-5 active channels for circular catheters and 2-3 for CS catheter), the activation times in all channels were detected. Then, the position of the moving window was iteratively re-adjusted to the center of detected activation times to avoid cutting of electrograms at the window edge. At this position, the final activation times in all channels were detected. Finally, it was ensured that the time difference between the detected activation and the previous one was large enough (typically 200 to 500 ms). If the difference was smaller, the activation set with the lower added signal energy from all channels was discarded.

6.5.2.2 Geometrical Preprocessing

For every detected wavefront, the corresponding electrode positions of the circular mapping catheter were analyzed.

First, the positions were projected onto a 2D surface. To this end, a PCA was performed on the 3D position data to separate the in-plane components (first and second eigenvector) from the normal direction (third eigenvector). An elliptic model was then fitted to the in-plane positions to determine the catheter center and the semi-major axis. This was necessary, because the mean position of all electrodes did not

necessarily represent the catheter center, especially when there was an overlap between the first and last electrodes. In this case, the first PCA eigenvector did not correspond to the semi-major axis either.

An estimate for the γ parameter in the cosine fit (angle difference between neighbouring electrodes) was finally determined by performing a cosine-fit of the x - and y -positions depending on the electrode number. To improve stability and reduce the number of parameters, a combined fit for x and y with a fixed phase shift of 90° was used.

6.5.2.3 Pacing Suppression

Several data segments contained measurements during pacing, i.e. electrically stimulated activity originating mostly in the CS. Due to the pulse strength, the pacing far-field was also detected in the circular mapping catheter, and its amplitude was often comparable to the EGMs originating from local substrate activation. Thus, it could impair wavefront detection.

Because the circular mapping catheter was far away from the pacing site, the time delay between pacing far-field and local excitation was large enough so that the two signals did not overlap. Therefore, far-fields could be removed with a relatively simple method. The pacing pulse was clearly visible in the electrograms of the corresponding pacing electrodes (e.g. in the CS catheter) and could be detected by applying a threshold of 15 mV. Then, 30 ms of signal in the circular catheter were set to 0 around the maximum of the pacing pulse.

Table 6.2. Overview over patient data. PAF = paroxysmal AF; RAFT = right atrial focal tachycardia

Pat	Age	Sex	Diagnosis	Segment	Meas Site	Analyzed data
1	50	f	PAF	1a	LA roof	NSR followed by incremental pacing from CS 3-4 (500 to 300 ms)
				1b	LA roof	NSR followed by incremental pacing from CS 7-8 (500 to 300 ms)
				1c	(CS only)	Stimulation with ablation catheter close to LSPV (500 to 300 ms)
				1d	(CS only)	Stimulation with ablation catheter close to LIPV (500 to 300 ms)
				1e	(CS only)	Stimulation with ablation catheter close to RIPV (500 to 300 ms)
				1f	(CS only)	Stimulation with ablation catheter close to RSPV (500 to 300 ms)
2	73	f	PAF	2a	LA ant	Alternating pattern with CLs 1300 / 450 ms
				2b	LA ant	NSR followed by pacing from CS 3-4 (600 ms), contained signal distortions
				2c	LA post	NSR followed by pacing from CS 3-4 (500 ms)
				2d	LA post	Incremental pacing from CS 3-4 (600 to 300 ms)
3	58	m	PAF	3a	LA ant	NSR
				3b	LA ant	NSR followed by pacing from CS 7-8 and CS 3-4 (500 ms)
				3c	LA roof	NSR
4	75	f	PAF	3d	LA roof	NSR followed by pacing from CS 7-8, NSR, and pacing from CS 3-4 (600 to 300 ms)
				4a	LA ant	NSR followed by pacing from CS 3-4 (600 ms)
				4b	LA ant	Pacing from CS 7-8 (500 ms)
				4c	LA roof	Pacing from CS 3-4 (500 ms)
				4d	LA roof	NSR followed by incremental pacing from CS 3-4 (600 to 300 ms)
				4e	LA roof	Pacing from CS 7-8 (500 ms)
5	59	m	RAFT	4f	LA roof	NSR followed by incremental pacing from CS 7-8 (600 to 300 ms)
				5a	RA FW	NSR followed by incremental pacing from ABL tip close to SN (500 to 300 ms)
6	61	f	PAF	5b	RA post	NSR followed by incremental pacing from CS 5-6, 500 to 300 ms
7	33	m	PAF	6a	LA ant	NSR
				7a	LA ant	Measured with AFocus II: NSR followed by pacing from CS 7-8 (500 ms)

6.6 CV Restitution Curves

CV restitution plays an important role in the genesis and maintenance of re-entrant excitations. Unfortunately, measurements from humans are very scarce. However, the cosine-fit method presented in section 6.1(b) allowed to calculate CV restitution curves from in-vivo measurements.

CV restitution can be expressed as relation between CV and the preceding diastolic interval [131]. However, effective refractory periods (ERPs) that are required to calculate the diastolic interval are more difficult to determine in clinical measurements. Therefore, CV restitution is also given as the relation between CV (or time delay) and preceding pacing cycle length (PCL) [132, 133] or inter-beat-interval (IBI) [134]. In the context of this analysis, CV restitution refers to the relation between CV and preceding IBI.

6.6.1 Available Data

Analysis of CV restitution was performed on the five patients in which measurements from incremental pacing were available. These were patients 1 to 5 (mean age 63 ± 10 years) with the recorded segments 1a, 1b, 2d, 3d, 4f, 4g, and 5a (see Table 6.2).

In patient 2 and 5, stimulation was performed from one position, whereas in patients 1, 3, and 4, two pacing sequences were available: one from CS bipole 3-4 and one from CS 7-8. The initial PCL was typically 600 ms and was then stepwise decreased to 500, 450, 400, 350, and 300 ms. In patients 1 and 5, the maximal pacing cycle length was 500 ms instead of 600 ms.

The electrograms of the wave propagation during normal sinus rhythm and during the different pacing setups were measured with the circular catheter. During the LA recordings, the catheter was in a stable position on the LA roof or posterior wall in case of the AF patients. For patient 5 with the RA tachycardia, the circular catheter was positioned at the RA free wall.

6.6.2 Local Conduction Velocity

The recorded pacing sequences were analyzed with the cosine-fit method presented in section 6.1(b). Local CV was calculated for every wavefront that was detected in the circular mapping catheter. If fits had a strongly increased residual they were likely to be invalid and were thus excluded from the analysis. As will be shown in section 10.5, typical residual values varied strongly between the data sets depending on signal morphology. Therefore, the residual mean and standard deviation over all

beats from one pacing sequence were determined. Then, beats with a residual of larger than two standard deviations above the mean residual were excluded.

Next, the IBI for each beat was calculated from the time difference to the previous event that was detected. To quantify rate-dependent changes, the events were binned based on the preceding IBI. Bins were separated at 275, 325, 375, 425, 475, 525, 800, and 1250 ms, resulting in seven bins from 275–325 to 800–1250 ms. They were set up such that the pacing intervals were mostly at the bin center. For patients in which pacing started at 500 ms, the bin 525–800 ms was not considered for further analysis. To test if there were significant differences between the distinct PCLs, the results were statistically analyzed. For every bin, the mean CV, the standard deviation and the 95% confidence interval for the mean CV were calculated. For a bin with n beats, the confidence interval was calculated from the t-distribution with $n - 1$ degrees of freedom.

To have a concrete quantity that could be compared between different patients and pacing sequences, the relative CV change between PCLs of 500 and 300 ms was examined. To test if the change was significant, a two-tailed Student's t-test was used [135, 136]. Changes with $P < 0.05$ were considered significant. Quantitative comparisons between NSR and pacing were not performed because in these cases CV changes could either result from different propagation directions or from different cycle lengths, making the results ambiguous.

In patient 4 during a PCL of 300 ms, a single pacing pulse was followed by multiple excitations in the circular mapping catheter, which implied a more chaotic rhythm. Therefore, only PCLs down to 350 ms were considered for analysis and statistics were calculated between 500 and 350 ms PCL.

6.6.3 Global Conduction Velocity

As an additional validation, the time delay T between pacing pulse and wavefront detection in the circular mapping catheter was calculated for all events (except for NSR, because there was no defined pacing pulse). The real distance that the wavefront travelled over the atria before detection was unknown, e.g. due to surface curvature and possible conduction anisotropy. However, the inverse $1/T$ of the time delay constituted a rescaled, spatially averaged CV over the regions that the wavefront passed before detection. It is from now on referred to as *global CV* and is expressed in relative units compared to the value at 500 ms in each pacing sequence.

The same statistical analysis as described in section 6.6.2 for the local CV was also performed for the global CV: For each bin, the average global CV over all beats was calculated together with the standard deviation and the 95% confidence interval.

Furthermore, the relative change in global CV between pacing at 500 and 300 ms was analyzed, including a t-test as described above.

Comparison of Simulated and Clinical Data

As a long-term goal, patient-specific atrial simulations could improve the understanding, diagnosis, and treatment of atrial arrhythmias. The first step into this direction is to test how well real excitation conduction in patients is reproduced by simulations. In this chapter, an attempt is described to compare patient measurements to simulation results based on the analysis of intracardiac electrograms.

To this end, patient-specific anatomical models were created from cardiac CT scans of the patients. Measurement positions of a circular mapping catheter and stimulation positions during coronary sinus (CS) pacing were taken from the recorded mapping data. These positions together with the anatomical model were then used to repeat the measurements *in silico*, i.e. in a simulation environment. The CV measured with the circular catheter was used in the simulations. The incidence directions of the clinical measurements and the simulations were then compared.

The analysis was performed for patients 1 to 4, for which a CT scan with contrast enhancement in the LA and the PVs was available. For each measurement site in the LA (anterior/posterior/roof) one segment with normal sinus rhythm (NSR), CS 3-4 stimulation, and CS 7-8 stimulation was included where available. The results will be demonstrated in chapter 11.

7.1 Creating Anatomical Models

Anatomical simulation models were created with an automatic segmentation tool. The segmented mesh was then transformed into a simulation geometry.

7.1.1 Automatic Segmentation Tool

CT scans from the four patients were segmented with an automatic atrial segmentation tool provided by PHILIPS Research Hamburg [137]. The tool was developed in

the course of two diploma theses by Raghed Hanna [138] and Peter Neher [139] in close collaboration with the Institute of Biomedical Engineering at KIT.

Automatic segmentation of the atria is especially challenging because the atrial epicardium is barely or not at all visible in CT-images. Therefore, a model based segmentation of only the atrial endocardium based on [44] was used as a landmark generator. Then, a finite wall-thickness model of only the left or of the left and right atrial myocardium was registered to the endocardial model.

As described in section 2.2.1, the PVs in the left atrium possess a strong topological variability between different patients. Therefore, a hybrid segmentation method was used for the LA that combined a model-based approach with a guided region growing. First, a shape model of the endocardial walls of all four chambers (without pulmonary veins) was adapted to the patient CT. Its approximate position was determined with a Generalized Hough Transformation. For segmentation of only the LA, a shape model of the LA was adapted using the Generalized Hough Transformation. In this simplified shape model, the PV regions with high variability were marked. This allowed to use a guided region growing in the next step to determine the number and shape of early branches of the PVs.

Based on this information, one of three precalculated mean shape models with different PV configurations was chosen and again adapted to the patient data. The different parts of the shape model were classified according to their position. The corresponding finite wall-thickness tetrahedron model was then registered to the endocardial model and represented the final segmented geometry.

In patients 1 to 3, the segmentation of only the LA was used for the simulations during CS stimulation. For simulations during NSR, the RA was manually segmented for patient 1, and the combined RA/LA segmentation was used in patients 2 and 3. In patient 4, a combined RA/LA model was used for all simulations.

The combined RA/LA model also contained information about electrophysiologically relevant structures such as Crista Terminalis and Bachmann's Bundle. However, for a first comparison between measurements and simulations, isotropic properties were assumed in the complete myocardium.

7.1.2 Creating Simulation Models

The cellular automaton requires cardiac anatomy to be stored as a voxel model. Therefore, the tetrahedron model from the automatic segmentation was voxelized with a resolution of 0.33 mm. Tissue class labels were converted to the notation used by the CA, and classes that were not included in the current simulations (such as

the pectinate muscles and the septum) were replaced by normal atrial myocardium. Finally, a closing filter was applied to smoothen spiky edges and to fill small holes. The global coordinate system of the voxelized model was further aligned with the CT coordinate system. For the solution of the forward problem, a new tetrahedron geometry of the atria surrounded by blood was created from the voxel model.

7.2 Extracting and Adapting Catheter Positions

For every segment, the catheter position from the EnSite data was used to place a virtual circular mapping catheter in the simulation model. However, the mapped positions usually had no wall contact in the simulation model due to localization inaccuracies. Therefore, the catheter was projected onto the model surface along its normal direction as described in section 6.4 and [130]. At the final position, metal electrodes with a radius of 1 mm were inserted in the tetrahedron geometry.

Localization errors for the catheter positions in patient 3 were even larger. Although the quality of the recorded electrograms suggested that there was good contact between catheter and the atrial wall, the mapped catheter positions were not parallel to the mapped endocardial surface. Therefore, the positions were rotated to be parallel to the surface before projection. To this end, the normal vector \mathbf{n}_c of the catheter and the normal vector \mathbf{n}_s of the closest surface region were determined. Then, the catheter was rotated around the rotation axis $\mathbf{n}_r = \mathbf{n}_c \times \mathbf{n}_s$ such that the catheter normal and the surface normal were parallel. Because the rotation axis was perpendicular to the catheter normal, the catheter was not rotated around its own axis. This minimized artificial offsets in the detected incidence directions.

The position of the CS stimuli was also determined from the recorded electrode positions of the CS catheter. For every segment, the position of the respective stimulating electrode pair was recorded for further use in the CA simulation.

For patients 1, 3, and 4, the mapped EnSite geometry had already been registered to the CT scan by a semi-automatic method in the EnSite system. Thus, mapped electrode positions could be transferred into the model coordinate system without further modification. This was not the case for patient 2, therefore, a transformation between EnSite coordinates and the segmented CT model was calculated using an iterative closest points method before further processing.

7.3 Electrogram Simulation and Analysis

Simulation of excitation conduction on the personalized anatomies was performed with the cellular automaton. For each patient and each measurement region (i.e. anterior/posterior/roof), a conduction velocity (CV) in the range of the measured values was used as input parameter for the CA.

Then, stimulations were applied at the same location as in the clinical measurements, i.e. at the position of the respective CS electrodes or in the sinus node. The resulting transmembrane voltage distributions were recorded every millisecond. They served as input data for the forward calculation in the respective tetrahedron geometry, in which the circular mapping catheter was modeled at the corresponding position. Finally, the electrograms at the electrodes of the circular catheter were extracted at the catheter centers.

These simulated electrograms were analyzed in the same way as the clinical signals, both with the cosine fit and (in case of wavefront collisions) with the RBF interpolation. Then, the resulting incidence directions were compared to those of the clinical measurements. The determined CVs from the simulated EGMs were further compared with the input CVs of the CA. It must be noted in advance that the comparison of simulated and measured incidence angles gives an idea of how well the simulated excitation pattern reflects the real excitation pattern in the patient for a given stimulus site. In contrast, the isotropic CV that is used to parametrize the CA does not influence the excitation pattern, it only makes it faster or slower. Therefore, the comparison of CV values determined from simulated EGMs to the input CV of the cellular automaton only gives an idea of possible errors in the CV measurement for a given catheter location and shape.

Part III

Results

Results: Adaptation of a Minimal Cell Model to Properties of Atrial Tissue

This chapter presents the adaptation results of the minimal model (MM) [50] to the cell model by Courtemanche, Ramirez, and Nattel (CRN) [47] as described in chapter 4. Section 8.1 presents the results for both the physiological and the remodeling case. Section 8.2 compares the minimal model and the CRN in a 2D patch for the remodeling case.

8.1 Adaptation Results

In the following, the adaptation results for the physiological and the remodeling case are described. The remodeling case is of special interest for simulations regarding atrial arrhythmias.

8.1.1 Physiological Case

Reference APs for the physiological case showed APD_{-73mV} values between approximately 320 ms for the longest and 290 ms for the shortest CLs. CV increased from 69 cm/s for the longest CLs to 70.5 cm/s at CLs of 500 ms, and then dropped to 62 cm/s for the shortest CL. The small CV increase at intermediate CLs is known as supernormal conduction [140].

The resulting parameter set is listed in Table 8.1 and the adaptation results are depicted in Figure 8.1. All curves for the MM that are shown were generated in a 1D patch as it was used for simulating the reference. The AP shapes show a good match between reference and minimal model. APD is around 5 ms higher in the MM. This is due to the fact that with the resulting MM parameter set, APD in the tissue patch was slightly higher than in the single cell simulations used for adaptation. The CV shows a very good fit between CRN reference and adapted MM. The wavelength (which was calculated as the product of ERP and CV) showed a good match, mainly due to the fact that ERP was somewhat shorter than APD.

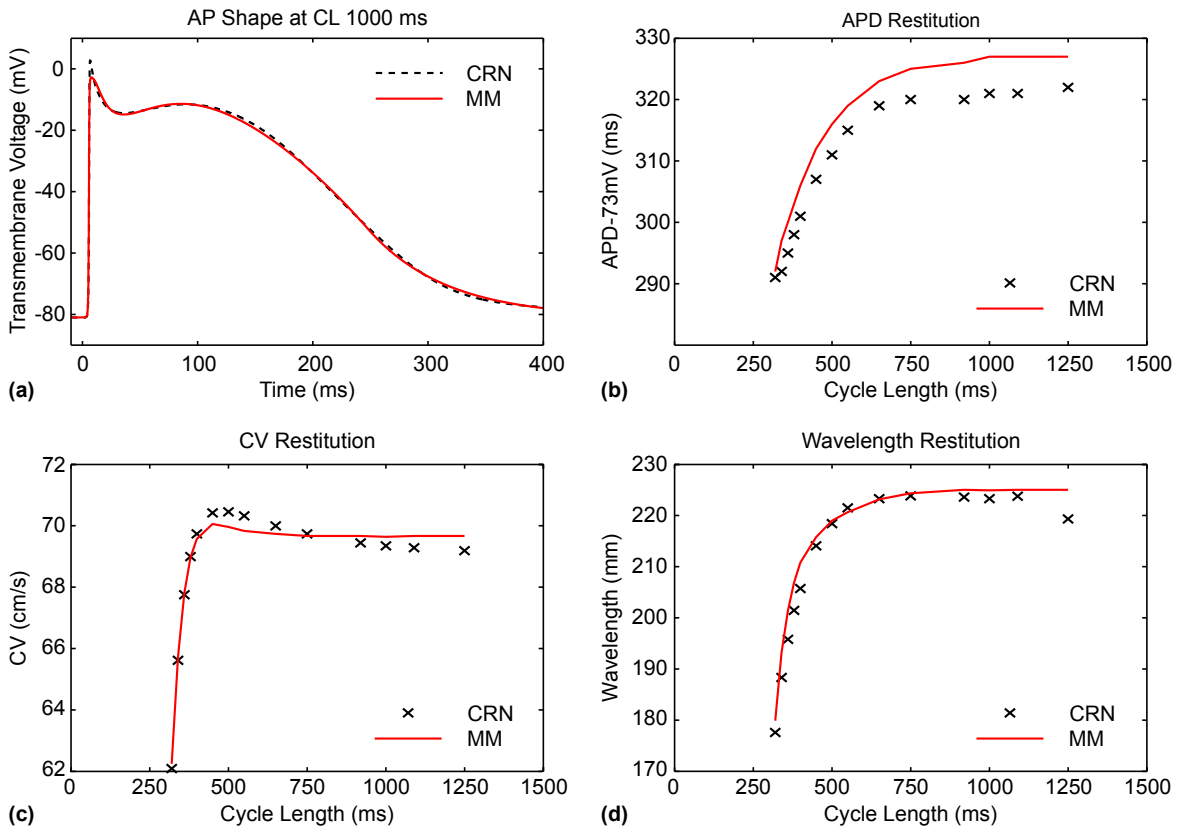


Fig. 8.1. Adaptation results for physiological case. (a) The AP shape at a CL of 1000 ms was well-reproduced by the MM. (b) The APD restitution curve of the MM was slightly shifted towards longer APDs compared to the CRN model. (c) CV restitution curves. (d) Wavelength restitution curves. Although the APD of the MM was longer than in the CRN model, the wavelength (calculated from ERP and CV) showed a good match between the models.

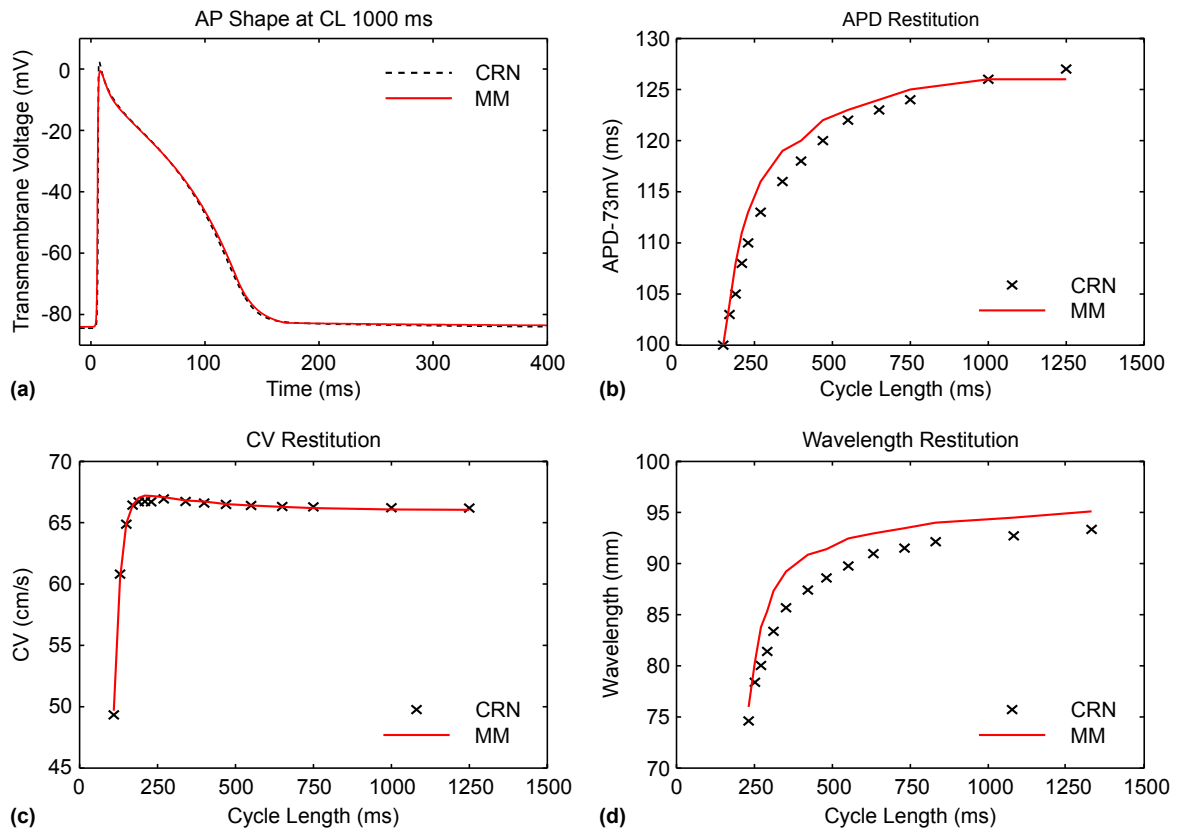
8.1.2 Remodeling Case

Implementation of the electrical remodeling shortened the APs by around 190 ms. Thus, resulting APDs were in the range of 127 to 100 ms. Because the APD was shortened, the point in the CV restitution curve at which CV started to strongly decrease was also shifted towards lower CLs. Thus, CV remained almost constant down to CLs of 170 ms, but then dropped of to 49 mm/s at a CL of 110 ms.

Table 8.1 also contains the parameter set for the remodeling case. Furthermore, Fig. 8.2 shows the corresponding adaptation results. The AP shape is well-reproduced, and both APD and CV restitution show a very good match between reference and adapted MM. For the remodeling case, there was no significant change between APD in single cell and patch simulations. However, ERP is some milliseconds longer than APD, resulting in a slightly increased wavelength compared to the CRN reference.

Table 8.1. Parameter sets for the MM after adaptation to the CRN model for physiological (Phys) and remodeling (Rem) case.

	u_o	u_u	θ_v	θ_w	θ_v^-	θ_o	τ_{v1}^-	τ_{v2}^-	τ_v^+	τ_{w1}^-
Phys	0	0.920	0.35	0.328	0.126	0.00005	41.857	1150	1.700	138.689
Rem	0	1.009	0.30	0.182	0.101	0.01547	16.300	1150	1.703	79.963
	τ_{w2}^-	k_w^-	u_w^-	τ_w^+	τ_{fi}	τ_{o1}	τ_{o2}	τ_{so1}	τ_{so2}	k_{so}
Phys	62.341	202.659	0.055	177.412	0.045	410.000	64.914	115.000	6.500	1.386
Rem	28.136	60.219	0.010	213.549	0.084	250.033	16.632	73.675	6.554	2.975
	u_{so}	τ_{s1}	τ_{s2}	k_s	u_s	τ_{si}	$\tau_{w\infty}$	w_{∞}^*	$V_{m,u}$	V_0
Phys	0.332	11.457	53.902	1.226	0.792	7.802	0.050	1.000	85.700	-80.960
Rem	0.592	9.876	4.204	2.227	0.816	10.699	0.223	0.902	85.700	-84.100

**Fig. 8.2.** Adaptation results for remodeling case. (a) Also the shortened AP of the remodeling case was well-reproduced by the MM. (b) The offset in APD restitution was lower than for the physiological case. (c) CV restitution matched well between the models. (d) Wavelength in the MM was slightly longer than in the CRN model.

8.2 Re-entry Simulations in a 2D Patch

The crossfield protocol described in section 4.5 successfully created a spiral wave (also called rotor) for both the CRN and the adapted MM under remodeling. First, a single rotor was present. Then, the single rotor could be split into two rotors by an ectopic beat 190 ms after the crossfield stimulus. The ectopic beat comprised 300×500

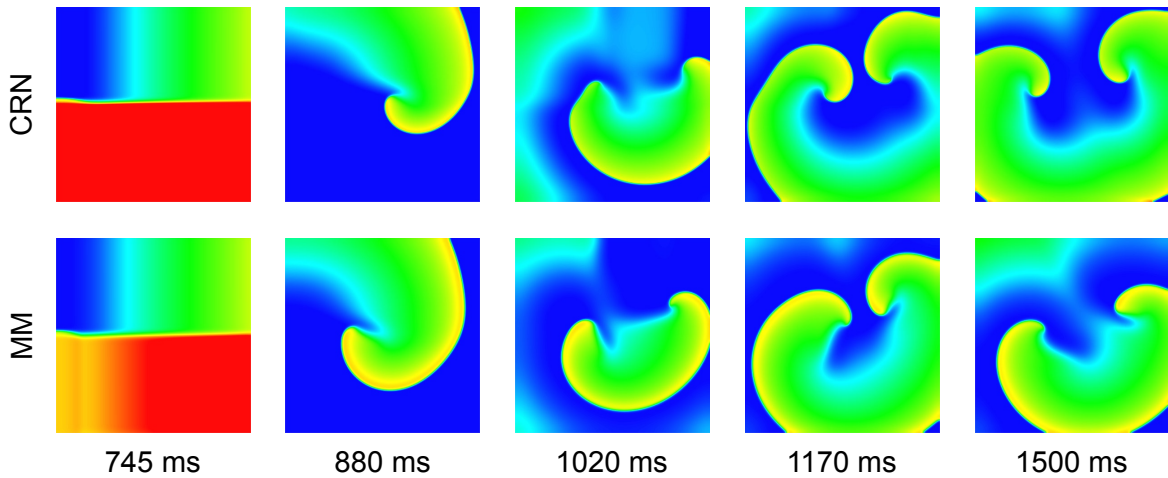


Fig. 8.3. 2D patch simulations for remodeling case. After 745 ms, the crossfield stimulus was applied and induced a spiral wave rotating clock-wise (shown at 880 ms). With a second stimulus, the single rotor was split into two rotors that formed a figure-of-eight re-entry. The re-entry pattern was stable for the remaining approximately 500 ms.

voxels and was placed in the back of the rotor. Example pictures of the rotor dynamics are shown in Figure 8.3. It can be seen that the dynamics of the minimal model were very similar to those of the CRN reference. However, the small wavelength difference also influenced dynamics in 2D. This can for example be seen in Figure 8.3 at $t = 1500$ ms, where the rotor tip was already moving downwards in the CRN simulation, whereas it was still moving to the right in the MM simulation.

8.3 Discussion

In this chapter, it was shown that with the proposed methods it was possible to adapt the parameters of the minimal model such that it reproduced excitation properties of the CRN model. Both the physiological and the remodeling case were considered, and one parameter configuration for each case was created. It was possible to use a limited subset of parameters for the different adaptation steps. Especially for the adaptation of the APD and CV restitution, it was sufficient to vary 6 or 3 parameters, respectively.

Small deviations occurred in the APD curve, because during the adaptation, APD was evaluated in the single-cell simulation for performance reasons. Curves in Figures 8.1 and 8.2, in contrast, were simulated in a more realistic patch environment. Especially for the physiological case, APDs in the patch were higher than in the single-cell simulations used during adaptation causing the observed deviation.

Although one-dimensional simulations can be used to ensure model agreement regarding basic properties, models should also be compared in 2D simulations. This ensures that the resulting wave dynamics are comparable, which is of high interest for the simulation of atrial arrhythmias. In such a 2D setup, the CRN and MM were compared for the remodeling case. It was demonstrated that basic wave dynamics were in good agreement. They only showed small deviations that probably resulted from the slight increase in wavelength for the MM. No 2D simulations were performed with the physiological models, because their wavelength was too high for stable rotors in realistic atrial dimensions.

Different best-guess parameter sets were used as start vectors to decrease the chance of finding local minima. However, there may always be a trade-off between the different adaptation steps, and performing more than two iterations might further improve the adaptation result. So the current parameter sets must be regarded as adaptations with a sufficient accuracy to demonstrate the feasibility of model adaptation. Furthermore, it is possible that different parameter sets may lead to very similar results. On the other hand, this is not a problem as long as the resulting model properties are satisfactory. Apart from that, further model comparisons in realistic 3D atrial geometries could be performed in addition to the 2D simulations.

When considering patient-specific simulations, the electrophysiological models need to be adapted to the patient's individual physiological parameters. Complex models such as the CRN model contain many parameters that were derived from ion channel measurements in humans and also in animals. Accurately determining these parameters for an individual patient is practically impossible in clinical routine. On the other hand, tuning some of the parameters to match measured properties is also challenging, because unwanted side-effects may appear. In contrast, a phenomenological model as the minimal model is less complex and thus more controllable. Still, it considers for example restitution behaviours that are not covered by the cellular automaton. It was sufficient to tune 6 or 3 parameters to adapt APD and CV restitution, respectively. Thus, the model can be adapted to patient-individual measurement data with less effort and without risking unwanted side-effects. It is therefore a promising approach for future patient-specific simulations of atrial arrhythmias.

Results: Influence of Tissue Conductivities on the ECG

This chapter presents the results of the two analyses regarding influences of tissue conductivities on the ECG or BSPM as described in chapter 5 as well as [90, 108]. Section 9.1 shows which tissue types had the strongest impact on the resulting signals for atrial simulations and analyses possible torso model simplifications. In section 9.2, the PCA method is evaluated which allows to efficiently estimate the signal changes resulting from tissue conductivity variations.

9.1 Tissue Ranking

To evaluate which tissues had the strongest impact on forward-calculated BSPMs, the conductivity values found in the literature for different tissues are presented first. Based on this compilation, the errors resulting from the sensitivity and uncertainty analysis are reported. Finally, errors resulting from possible torso model simplifications are analyzed.

9.1.1 Conductivity Values in the Literature

The maximum and minimum conductivities for each tissue as compiled from the literature are summarized in Table 9.1. These values were used as upper and lower boundaries for the uncertainty analysis. The table is sorted by the ratio of conductivity boundaries. \parallel and \perp indicate conductivities along and across muscle fibers. The lower boundary for intestine is taken from colon measurements, whereas the upper conductivity was measured on the small intestine. The values by Gabriel et al. at 10 Hz are indicated for comparison [60]. They were varied by $\pm 25\%$ in the sensitivity analysis. The resulting upper and lower conductivity boundaries for the sensitivity analysis are not explicitly stated in Table 9.1 but can easily be calculated from the given values. Values from Colli Franzone et al. [141] were used for the intracellular transverse conductivity of the heart muscle $\sigma_{i\perp}$ and the corresponding anisotropy

Table 9.1. Lower and upper tissue conductivity boundaries

Name	σ_{\min} (S/m)	GG (S/m)	σ_{\max} (S/m)	Ratio
Intestine	0.0122 [60]	0.278	0.511 [60]	41.9
Kidneys	0.0544 [60]	0.0544	0.9 [61]	16.5
Bone	0.005 [98]	0.02	0.06 [98]	12.0
Heart, rand.	0.0537 [60]	0.0537	0.483 [92]	9.0
Muscle aniso.	2.04 † [93]	-	15.3 † [95]	7.5
Liver	0.0277 [60]	0.0277	0.2 [98]	7.2
Spleen	0.0396 [60]	0.0396	0.24 [57]	6.1
Fat	0.0122 [60]	0.0377	0.0667 [91]	5.5
Muscle \perp	0.0435 [95]	0.202	0.213 [93]	4.9
Lungs	0.0389 [60]	0.0389	0.134 [92]	3.4
Muscle \parallel	0.33 [62]	-	0.8 [62]	2.4
Blood	0.435 [92]	0.7	1.0 [91]	2.3
Trunk	0.216 [95]	-	0.241 [93]	1.1

†The anisotropy ratios are dimensionless

ratio ($\sigma_{i\perp} = 0.031525$ S/m; anisotropy ratio: 9.516). Extracellular anisotropy ratios that are frequently used are e.g. 2.23 [95], 2.5 [142] or 4 [143]. For the uncertainty analysis, conductivity values for heart muscle at a random fiber orientation were chosen for the extracellular conductivity across the fiber. The anisotropy ratio was fixed at 3, this is in good agreement with the previously stated ratios.

9.1.2 Ranking for Atrial Signals

Tables 9.2 and 9.1.2 show the results of the atrial sensitivity and uncertainty analysis. Tissue types are sorted according to the RMSE calculated from the not-normalized signals. The numbers in parentheses correspond to the ranks in the respective $\text{RMSE}_{\text{norm}}$ or CC-sorted tables.

In both rankings, there was a group of more important organs that comprised muscle (including anisotropy), blood, lungs, fat, and the heart muscle. In contrast, liver, bone, spleen, and kidneys played a minor role in both rankings. When comparing the uncertainty with the sensitivity ranking, the main differences were an increase in heart and intestine importance and a decrease in blood and fat importance. The intestine was shifted upwards in the uncertainty ranking due to the large uncertainty caused by including values from both small and large intestine.

For some organs, the ranking based on the CC was different from the RMSE-sorted ranking. When looking at the CC in the sensitivity ranking, the main differences

compared to the RMSE-sorted ranking were the higher importance of lung and fat tissue and the significantly reduced importance of skeletal muscle conductivity. All other organs in the sensitivity ranking did not move more than one rank up or down. For the uncertainty ranking, skeletal muscle conductivity and anisotropy as well as blood were less important in a CC-sorted ranking, whereas heart, fat, and liver were more important.

Finally, the $\text{RMSE}_{\text{norm}}$ -sorted ranking was taken into account. The $\text{RMSE}_{\text{norm}}$ -sorted and CC-sorted rankings were compared because both criteria focus on signal morphology rather than amplitude scaling. In case of the sensitivity ranking, the skeletal muscle anisotropy and the heart muscle conductivity became less important for the $\text{RMSE}_{\text{norm}}$. Intestine and skeletal muscle conductivity, in contrast, became more important. For the uncertainty ranking, intestine ranked significantly higher whereas fat ranked lower in the $\text{RMSE}_{\text{norm}}$ -sorted table.

9.1.3 Ranking for Ventricular Signals

A similar analysis has been performed for ventricular input signals during the PhD thesis of David Keller, the results can be found in [90]. Rankings for the atrial and ventricular signals showed many common features, apart from the tendency that the lungs were more important for atrial signals and skeletal muscle as well as heart were more important for ventricular signals. Therefore, statements in the discussion hold for both types of signals.

Table 9.2. Results of the sensitivity analysis for atrial signals

Rank	Name	RMSE (μV)	$\text{RMSE}_{\text{norm}}$	1-CC
1	Muscle \perp	13.2	6.85E-3 (4)	2.88E-3 (6)
2	Blood	10.4	1.03E-2 (2)	7.89E-3 (1)
3	Muscle aniso.	9.0	6.59E-3 (6)	3.15E-3 (4)
4	Lungs	6.9	1.09E-2 (1)	7.80E-3 (2)
5	Fat	5.3	8.77E-3 (3)	6.14E-3 (3)
6	Heart	4.6	6.19E-3 (7)	3.12E-3 (5)
7	Intestine	4.1	6.82E-3 (5)	2.47E-3 (7)
8	Liver	2.2	3.59E-3 (8)	9.78E-4 (8)
9	Bone	1.6	2.49E-3 (9)	5.16E-4 (9)
10	Cartilage	0.55	9.33E-4 (10)	6.18E-5 (10)
11	Spleen	0.16	2.65E-4 (11)	5.82E-6 (11)
12	Kidneys	0.12	2.01E-4 (12)	2.19E-6 (12)

Table 9.3. Results of the uncertainty analysis for atrial signals

Rank	Name	RMSE (μV)	RMSE _{norm}	1-CC
1	Muscle \perp	46.1	2.12E-2 (7)	2.43E-2 (7)
2	Muscle aniso.	35.7	2.52E-2 (5)	4.49E-2 (5)
3	Heart	22.0	3.28E-2 (2)	7.62E-2 (1)
4	Lungs	20.9	3.25E-2 (3)	5.88E-2 (3)
5	Intestine	19.6	3.32E-2 (1)	5.32E-2 (4)
6	Blood	17.0	1.67E-2 (8)	2.06E-2 (8)
7	Fat	16.8	2.76E-2 (4)	6.29E-2 (2)
8	Liver	12.8	2.12E-2 (6)	3.40E-2 (6)
9	Bone	7.0	1.12E-2 (9)	1.03E-2 (9)
10	Kidneys	0.85	1.50E-3 (10)	1.24E-4 (10)
11	Spleen	0.61	9.95E-4 (11)	8.16E-5 (11)

Table 9.4. Error (RMSE or CC based) of possible torso simplifications

		$\bar{\sigma}_1$	$\bar{\sigma}_2$
RMSE	TOP7 _{RMSE}	6.0 μV	7.1 μV
	TOP5 _{RMSE}	11.2 μV	11.6 μV
	TOP3 _{RMSE}	15.3 μV	16.9 μV
	HOM _{RMSE}	89.3 μV	42.9 μV
1-CC	TOP7 _{1-CC}	7.8E-3	1.1E-2
	TOP5 _{1-CC}	2.4E-2	2.9E-2
	TOP3 _{1-CC}	5.0E-2	4.2E-2
	HOM _{1-CC}	1.3E-1	1.2E-1

9.1.4 Possible Torso Model Simplifications

Table 9.1.4 lists the evaluation of possible torso model simplifications. Organs that were not considered were replaced with one of two mean conductivities $\bar{\sigma}_1$ (weighted average over VM torso) or $\bar{\sigma}_2$ (derived from literature values). The more organs and structures were considered in the model, the better the BSPMs matched the reference data.

9.1.5 Discussion

In section 9.1, the influence of tissue conductivities on forward-calculated ECGs was ranked. A number of studies with similar aims has been performed before [67, 68, 144, 145]. However, the current results deliver additional and new insights because the approach is different regarding the underlying cardiac source distribution, the torso model and utilized conductivity comparison methods. The most important differences are:

1. To the knowledge of the author, this is the first study to systematically evaluate the role of torso inhomogeneities based on realistic cardiac simulations for atrial signals. Previous investigations were based on dipole [67, 144, 146] or double layer sources [147, 148], sources calculated from an inverse procedure [149] or epicardial recordings that were acquired from dog [145] or during open heart surgery on a human [68].
2. The details of the torso model significantly differ compared to previous studies. The eccentric spheres models used in [147] and [148] have been criticized by Bradley et al. [67] and van Oosterom et al. [149]. While the use of "tailored" geometries was favored, several older studies used only coarse torso models containing only a few hundred or thousands of nodes to reduce computation time [144, 146, 149]. Furthermore, even recent studies [67, 68] (and all studies before) evaluate only a limited subset of the organs and structures that were investigated here. In simple torso models that only consider a small number of inhomogeneities, the importance of one inhomogeneity might be increased or reduced if additional inhomogeneities would have been considered. Therefore, the importance of inhomogeneities is difficult to judge in such simple torso models, and the results from investigations that evaluated differently composed torso models are not necessarily directly comparable.
3. Conductivity values utilized for the different inhomogeneities and ratios between the conductivities of the various organs strongly differed between previous studies. However, they made no efforts to estimate the effects that such differences might have had on the results.

Within the current study it was therefore differentiated between a sensitivity and an uncertainty analysis. For the sensitivity analysis, fixed percental changes of a specific conductivity were used. In the uncertainty analysis, the impact of the existing uncertainty in frequently used conductivities was evaluated. To this end, published conductivity values were collected and forward calculations for each organ's minimum and maximum conductivity were conducted. With the RMSE as evaluation criterion, the atrial simulation was most sensitive to skeletal muscle, blood, heart, lungs, and fat conductivity as well as skeletal muscle anisotropy. For changes in signal morphology with the CC as a criterion, skeletal muscle had a much lower impact but fat on the other hand was more important.

It was explained above that a comparison of the presented findings with results of previous studies is difficult due to methodological differences, differences in the torso model and in the chosen conductivities. While keeping that in mind, the following

similarities and differences were observed: Previous reports stated that the lungs were both important [67, 68, 144, 147] and unimportant [149, 145]. Skeletal muscle conductivity showed a large [148], moderate [67, 147] or small [68] impact on torso potential, whereas skeletal muscle anisotropy was always found to be important [68, 145]. Heart tissue conductivity had a strong effect in [67] and [149], which is in accordance with presented results. Furthermore, the large effects reported here for blood agree with studies from Rudy et al. [147] and van Oosterom et al. [149]. However, they contradict earlier findings from Rudy et al. [148] in which blood was less important. In the current investigations, fat had moderate effects on signal amplitude but stronger effects on signal morphology. This contradicts findings from Bradley et al. [67] and Klepfer et al. [68], where large effects were seen, and a study by Rudy et al. [147] where only small effects were found. Investigations that considered the effects of spine and sternum found that they were of small importance [68, 144, 145]. Klepfer et al. [68] additionally evaluated the effect of bone but found no relevant influence on the forward solution. The current data included all major bony and cartilaginous structures but likewise found no significant impact. Intestine, liver, spleen, and kidneys were not included in previous studies. The presented results show that of these four structures, intestine was the most important one, followed by the liver. This was probably due to its large size (intestine: 6.3% vs. liver: 4.1% vs. kidneys 0.8% and spleen 0.5% of the torso volume). However, this group ranged at the lower end of most rankings.

When the uncertainty of the published conductivities was considered in the uncertainty ranking, the importance of heart tissue and intestine increased, whereas the impact of blood and fat decreased. The importance in the uncertainty ranking was directly related to the degree of uncertainty (Table 9.1): The higher the ratio between lower and upper conductivity value, the higher the ranking of the respective organ was in the uncertainty analysis. Especially for kidney, bone, liver, and spleen, which are rarely considered, but also for very important tissues (e.g. heart or skeletal muscle fiber anisotropy) there are significant differences that the measurement community should address.

No simple answer exists with respect to the level of detail to be incorporated into a torso model. As expected, solution quality increased with increasing number of inhomogeneities. This can be seen as the RMSE or 1-CC between the gold standard (completely inhomogeneous model) and the simplified setups decreased. Furthermore, removing inhomogeneities with conductivities close to the average conductivities $\bar{\sigma}_{1,2}$ had a comparatively small influence. However, for most applications, including the 5 most important inhomogeneities besides the heart should be sufficient. These are

skeletal muscle conductivity as well as anisotropy, blood, lungs, and fat. This list agrees with the suggestions from Bradley et al. [67], although their ranking was different and no effects of the intracavitary blood pool were evaluated. It is interesting to note that the errors caused by model simplifications also depended on the utilized mean conductivity $\bar{\sigma}_{1,2}$. It might therefore be possible to derive an optimized $\bar{\sigma}$ that minimizes the differences between simplified and completely inhomogeneous torso model for future studies.

Furthermore, the impact of the blood in the major vessels (superior and inferior vena cava, pulmonary arteries and veins, aorta) was evaluated as well as the impact of the fat layer around the heart. Because segmentation is time-consuming, these structures are rarely included in patient-specific geometries. In the Visible Man data set, they constituted a part of the total blood and fat volume, respectively. To rate their importance, they were isolated by assigning unique tissue classes, then a sensitivity analysis as described in section 5.1.3 was performed. In an RMSE-sorted ranking, the blood in the main vessels would rank on position 4, so that it should be included in torso models for atrial simulations. The fat around the heart, in contrast, ranked on position 8 and might therefore be negligible.

One may not forget that all evaluations of the BSPM sensitivity with respect to tissue conductivities inherently depend on the default conductivities and the utilized torso model. Using the same default conductivities in combination with different torso models or the opposite case of different default conductivities in combination with the same torso model are likely to produce different sensitivity rankings. Although this study quantified the effects of the present conductivity uncertainties on electrocardiographic simulations, the ideal solution would be to further narrow down the possible choices, which will be the task of the measurement community.

Bradley et al. [67] and Klepfer et al. [68] reported that different organs have slightly varying influences on the different ECG segments (P, QRS, T). This means that different excitation sequences will result in slightly different RMSE or CC values (but not necessarily different rankings). To validate the results, additional atrial simulations were performed with altered conduction velocities in the Crista Terminalis and Bachmann's Bundle (both set to 1400 mm/s). This different anisotropy setup produced minor ranking changes only, so that the conclusions drawn in this work are applicable to other physiological excitation sequences as well.

Furthermore, gender-specific differences concerning the composition of the torso model (i.e. skeletal muscle volume vs. fat volume) must be considered. The Visible Man data set has a very high body fat volume fraction (38% within the torso) and results will probably be different for slimmer models. Additionally, the Visible Man

Table 9.5. Ratio between first and second PCA eigenvalue λ_1/λ_2

	Blood	Muscle	Lung	Fat
Atria	232	181	299	77
Ventricles	652	106	489	31

data set includes fine structures with many details. From images recorded using current medical imaging techniques such as MRI or CT, such detailed models can not be generated. Therefore, conductivity sensitivities might be different in patient-specific models.

This study could be repeated with a larger set of differently composed torso models as soon as methods become available that allow for creation of skeletal muscle fiber orientation for patient-specific data sets. Such a study would take into account both inter-individual as well as gender-specific variations. Thus, it would allow a concluding evaluation of how different inhomogeneities impact on the BSPM.

9.2 BSPM Prediction for Varying Conductivities Based on Principal Component Analysis

In the previous section, tissue conductivities were shown to have a significant impact on the forward-calculated ECGs. In the following, it is evaluated how such signal changes can be efficiently addressed with the PCA method proposed in section 5.2. First, the ratios between the eigenvalues and the angles between different eigenvectors are shown to support the assumptions made when developing the method. Then, errors for signal reconstruction for variations of one and four tissue conductivities are evaluated. Finally, an exemplary ECG confidence interval is demonstrated.

9.2.1 Eigenvalue Ratios and Eigenvector Angles

Table 9.5 lists the ratios λ_1/λ_2 for the different tissues which were in the range of 31 to 652. This confirmed that the information content of the first principal component (PC) was much larger than that of the second PC for all organs. The assumption was used in the transformation from (5.5) to (5.6).

Pairwise angles between the first eigenvectors of the four tissues ranged between 45° and 124° for the atria and 57° and 143° for the ventricles. Thus, they were far from 0° or 180° .

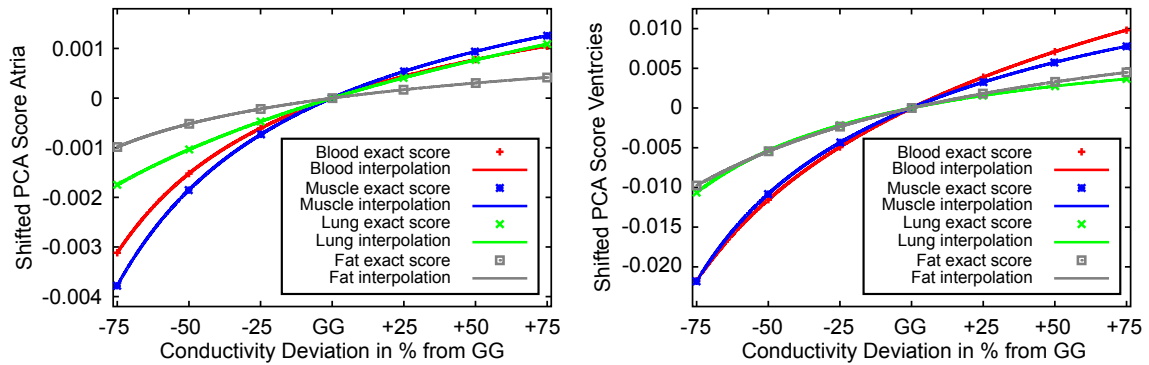


Fig. 9.1. Shifted PCA scores for first eigenvectors of atrial (left) and ventricular input data (right) [108]. The exact scores that were determined directly from the PCA are marked as data points. The solid lines show the results of the polynomial interpolation. The sensitivity of the forward problem to the respective conductivity variation is reflected by the difference between minimum and maximum score for a specific tissue.

9.2.2 Signal Reconstruction

The shifted PCA scores of the different tissues were monotonically dependent on the conductivity values for atrial and ventricular data (Fig. 9.1).

The upper part of Table 9.6 lists the RMSEs if the signal for a single tissue conductivity variation was reconstructed from the *exact* scores within $\pm 75\%$ of the Gabriel-Gabriel (GG) conductivity from the first eigenvector only. The maximum RMSE was approximately $2.6 \mu\text{V}$ for the atria and $12.6 \mu\text{V}$ for the ventricles. Thus, compared to the signal amplitudes in the millivolt range, the RMSE was at least two orders of magnitude smaller.

The lower part of Table 9.6 shows the RMSEs if the signal for a single tissue conductivity variation was reconstructed from the *interpolated* scores within $\pm 50\%$ of the GG conductivity. The maximum RMSE was around $1.8 \mu\text{V}$ for the atria and $8.5 \mu\text{V}$ for the ventricles. Thus, the maximum errors were comparable to the maximum errors for the exact scores (for variations of $\pm 50\%$).

The results for the combined variations of all four conductivity values are listed in Table 9.7. When each conductivity was varied by $\pm 25\%$, reconstruction of the atrial data resulted in an average RMSE of $1.6 \pm 0.4 \mu\text{V}$. For variations of $\pm 50\%$, the average RMSE was $6.3 \pm 2.9 \mu\text{V}$. In the ventricles, the average RMSE was $5.8 \pm 1.5 \mu\text{V}$ for variations of 25% and $19.0 \pm 5.6 \mu\text{V}$ for variations of 50% . An example of the reconstruction is shown in Fig. 9.2.

9.2.3 Confidence Intervals

The confidence intervals resulting from relative conductivity variations of $\pm 10\%$, $\pm 30\%$, and $\pm 50\%$ are shown in Fig. 9.3. As the relative uncertainty $\delta\sigma_{\text{rel}}$ becomes

Table 9.6. RMSE (μV) when using *exact* and *interpolated* scores

		RMSE exact scores				RMSE interpolated scores			
		Blood	Muscle	Lung	Fat	Blood	Muscle	Lung	Fat
Atria	$\sigma_{-75\%}$	1.910	2.612	1.389	1.200	—	—	—	—
	$\sigma_{-50\%}$	0.387	0.457	0.259	0.139	0.566	0.709	0.209	0.216
	$\sigma_{-25\%}$	0.422	0.097	0.588	0.207	0.441	0.609	0.114	0.219
	σ_{GG}	0.002	0.001	0.001	0.000	—	—	—	—
	$\sigma_{+25\%}$	0.597	0.832	0.307	0.328	0.598	0.831	0.296	0.324
	$\sigma_{+50\%}$	1.248	1.695	0.751	0.715	1.316	1.779	0.783	0.748
	$\sigma_{+75\%}$	1.903	2.557	1.274	1.120	—	—	—	—
Ventricles	$\sigma_{-75\%}$	5.782	12.597	2.868	12.120	—	—	—	—
	$\sigma_{-50\%}$	1.009	1.335	0.343	0.767	1.465	2.420	0.560	1.671
	$\sigma_{-25\%}$	1.071	2.492	0.516	1.945	1.151	2.591	0.547	2.081
	σ_{GG}	0.008	0.002	0.002	0.003	—	—	—	—
	$\sigma_{+25\%}$	1.586	3.884	0.866	3.166	1.585	3.862	0.864	3.113
	$\sigma_{+50\%}$	3.370	8.100	1.895	6.875	3.578	8.475	1.994	7.209
	$\sigma_{+75\%}$	5.215	12.434	2.975	10.713	—	—	—	—

larger, the gap between the GG signal and the respective minimal/maximal signal becomes wider. The real signal will lie somewhere within the gap. It can be seen that the effects of increasing conductivity uncertainty on the different phases of the cardiac cycle (P-wave, QRS complex, and T-wave) are very similar.

9.2.4 Discussion

A PCA-based method for prediction of forward-calculated BSPM signals for different tissue conductivities has been developed. It allows for predicting signals over a wide range of tissue conductivity values from few sample simulations only. The method was further validated for both atrial and ventricular signals.

The proposed PCA-method is based on the assumption that variation of a single tissue conductivity causes changes in the BSPM that can be expressed by the first eigenvector of a PCA decomposition. This assumption holds, because the first eigenvalue for all tissues was significantly higher than the second and all following eigenvalues with ratios larger than 30. Therefore, the first eigenvector described the major part of signal variation. This is further supported by the relatively small errors when reconstructing BSPM signals for single tissue conductivity variations based on the *exact* scores. These errors were due to considering only the first eigenvector. No higher

Table 9.7. RMSE (μV) for combined conductivity variations

Relative variation z	Atria		Ventricles	
	25%	50%	25%	50%
$\sigma_{B-z} \sigma_{M-z} \sigma_{L-z} \sigma_{F-z}$	2.1	11.3	7.2	22.6
$\sigma_{B-z} \sigma_{M-z} \sigma_{L-z} \sigma_{F+z}$	1.9	10.0	4.1	18.8
$\sigma_{B-z} \sigma_{M-z} \sigma_{L+z} \sigma_{F-z}$	2.7	13.6	8.4	27.7
$\sigma_{B-z} \sigma_{M-z} \sigma_{L+z} \sigma_{F+z}$	1.0	5.7	4.5	21.0
$\sigma_{B-z} \sigma_{M+z} \sigma_{L-z} \sigma_{F-z}$	1.7	6.7	5.0	18.1
$\sigma_{B-z} \sigma_{M+z} \sigma_{L-z} \sigma_{F+z}$	1.7	5.8	8.1	26.2
$\sigma_{B-z} \sigma_{M+z} \sigma_{L+z} \sigma_{F-z}$	1.3	5.4	4.3	15.0
$\sigma_{B-z} \sigma_{M+z} \sigma_{L+z} \sigma_{F+z}$	1.7	5.2	7.0	18.4
$\sigma_{B+z} \sigma_{M-z} \sigma_{L-z} \sigma_{F-z}$	1.2	4.3	6.0	16.6
$\sigma_{B+z} \sigma_{M-z} \sigma_{L-z} \sigma_{F+z}$	1.7	6.0	5.8	20.9
$\sigma_{B+z} \sigma_{M-z} \sigma_{L+z} \sigma_{F-z}$	1.4	5.0	7.9	26.5
$\sigma_{B+z} \sigma_{M-z} \sigma_{L+z} \sigma_{F+z}$	1.5	5.9	5.5	19.1
$\sigma_{B+z} \sigma_{M+z} \sigma_{L-z} \sigma_{F-z}$	1.3	3.7	6.0	20.8
$\sigma_{B+z} \sigma_{M+z} \sigma_{L-z} \sigma_{F+z}$	1.6	5.2	4.2	7.6
$\sigma_{B+z} \sigma_{M+z} \sigma_{L+z} \sigma_{F-z}$	1.2	3.6	4.8	15.9
$\sigma_{B+z} \sigma_{M+z} \sigma_{L+z} \sigma_{F+z}$	1.2	2.9	4.8	9.3
Average	1.6	6.3	5.8	19.0

eigenvectors were needed for the reconstruction, because the RMSE was small (max. $12.6 \mu V$) compared to the signal amplitude in the millivolt range. It was further evident that RMSEs for the ventricles were typically larger than for the atria, because the amplitude of the ventricular signal was higher.

It was sufficient to perform only seven sample simulations with different conductivities for each tissue. Then, signals for values in between could be derived by an interpolation of the PCA score curve. A leave-one-out validation with the $\pm 25\%$ and $\pm 50\%$ simulations was performed. It showed that RMSEs of reconstruction using *interpolated* scores were not significantly increased compared to the RMSEs from *exact* scores for equal conductivity variations. It should be noted that no leave-one-out validation was performed with the $\pm 75\%$ simulations, because the score curve is only interpolated between the minimal and maximal conductivity. Removing one simulation at the outer end of the curve, e.g. at $+75\%$, from the PCA input data means that the interpolation function would only be defined in the -75% to $+50\%$ region. Typically, there can be more than one tissue for which the conductivity is not exactly known. Therefore, it was shown that the PCA method can also predict effects

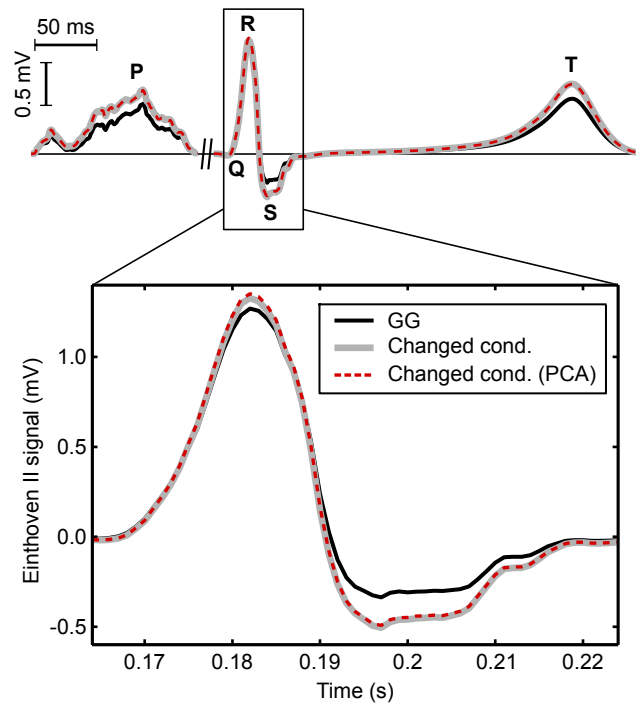


Fig. 9.2. Example for PCA reconstruction of signal changes caused by combined conductivity variations (here: blood and muscle decreased by 25%, lungs and fat increased by 25%) [108]. The bottom part magnifies the QRS complex shown above. The signal calculated using the standard Gabriel *et al.* (GG) conductivities significantly deviates compared to the signal with all four tissue conductivities varied. The presented PCA method could predict the effect of these combined variations in all sections (P-wave, QRS-T complex) with small errors only (P-wave amplitude 2x magnified for better visibility).

of combined conductivity variations on the BSPM. To this end, the coordinate systems of the different PCAs were aligned with the GG signal as a common origin. It was then assumed that the effects of combined conductivity variations can be expressed by a superposition of the effects caused by the respective single conductivity variations. Although previous reports noted that the combined effect of conductivity variations in two different organs was not necessarily additive [68, 150], Fig. 9.2 already demonstrates that the PCA method can reproduce most of the signal changes. The fact that the average RMSE for combined variations of $\pm 25\%$ amounted to only $1.6 \mu V$ in the atria and $5.8 \mu V$ in the ventricles further supported the validity of the superposition. Even when increasing the conductivity variations to $\pm 50\%$, the average RMSE only was $6.3 \mu V$ for the atria and $19.0 \mu V$ for the ventricles (for simplicity reasons equal variations were chosen here, generally however, the amount of conductivity variation may be different for different tissues). There are of course signal changes caused by combined conductivity variations that are not accounted for by the proposed PCA method, for example, amplification of changes or non-linear cancellation. It is therefore emphasized that the linearization applied here is only an

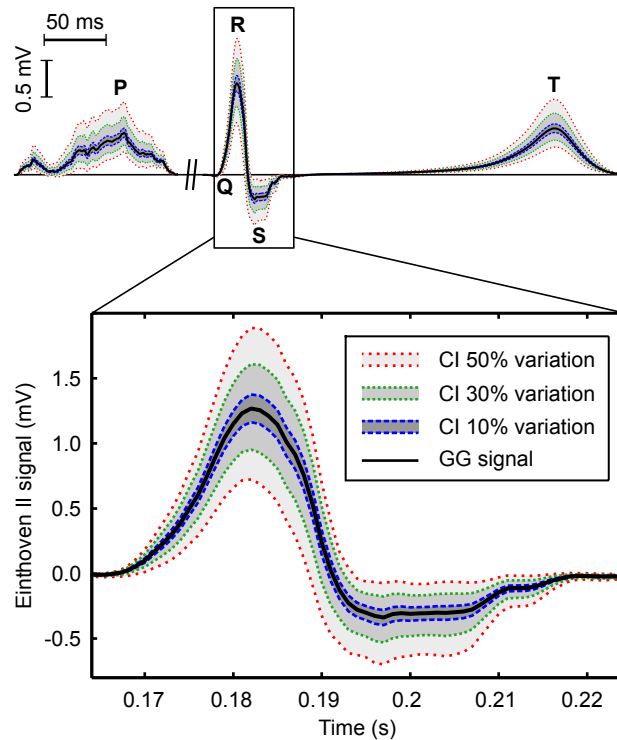


Fig. 9.3. ECG confidence intervals derived from PCA method [108]. Shown are the maximum and minimum Einthoven II signals at each time step that are possible for different conductivity uncertainties. Confidence intervals for simultaneous uncertainties of $\pm 10\%$, $\pm 30\%$, and $\pm 50\%$ in all four tissues were calculated. The P-wave amplitude was doubled for better visibility.

approximation. Such linear approximations are applicable to many problems, the key question is over which range they are feasible and how large the errors are. In the presented data, the RMSE values demonstrate that the PCA method provides a very good estimation of the real signal without the necessity to perform another time-consuming forward calculation that can take over one hour. In contrast, the PCA decomposition and BSPM reconstruction were completed within approximately 1 s (which includes program startup and data loading) on a single CPU of a standard desktop computer. Apart from reconstructing BSPM signals for different conductivity combinations, the presented PCA method allows for estimating an ECG confidence interval for various conductivity uncertainties without additional forward calculations. To this end, the minimum and maximum signal that could result from certain conductivity boundaries were calculated for every time step and electrode. Furthermore, it can determine the minimum and maximum signals in any set of *bipolar* leads. Because the problem is monotonic, only signals at the boundaries of the conductivity ranges needed to be evaluated. The minimal and maximal curve are shown in Fig. 9.3. However, they were normally not signals that resulted from one fixed conductivity setup. Instead,

different conductivity combinations produced the maximum signal at different time instants. Therefore, the confidence intervals corresponded to the range within which the ECG signal will certainly lie.

In future studies, a more advanced confidence interval could also be calculated by evaluating the *probability* for the signal to lie within certain boundaries, similar to [150]. The PCA method is able to efficiently predict the signals at finite conductivity steps between the boundaries. These signals could then be statistically analyzed in terms of the mean signal and the standard deviation. Compared to [150], such statistics give only limited insight into the underlying processes and are only calculated on the torso surface. On the other hand, they can be computed *a posteriori* with the advantage that the setup does not have to be changed. Furthermore, they can easily be computed for a 3D torso and at all time steps, whereas in [150], only 2D slices are analyzed at distinct time steps.

In theory, it might also be possible to apply the PCA method to the inverse problem of electrocardiography, which means locating the cardiac sources for a certain BSPM. To this end, the potentials on the heart surface could be calculated several times from a measured BSPM signal with different conductivities for a specific organ. Based on this data, the PCA could then be used to determine changes in the source distribution on the heart that result from conductivity variations.

In conclusion, an efficient PCA-based method to analyze BSPM signals was developed. The first eigenvector of a PCA decomposition quantitatively described the changes in body surface potential when a single tissue conductivity was varied. Superposing eigenvectors from PCAs for different tissues gave a good estimation of how combined conductivity variations changed the resulting BSPM. This way, the method could further calculate confidence intervals for arbitrary conductivity uncertainties within the initial conductivity boundaries. It must be noted that eigenvectors and PCA scores are calculated separately for every model, e.g. for different patients. Thus, they are tailored, which means that they consider patient-specific differences in thorax anatomy (like organ size and position), cardiac anatomy and electrophysiology. Therefore, the method is not limited to a certain setup and can also be applied to models resulting from anatomical and electrophysiological personalization. Hence, it is a promising approach to evaluate the impact of conductivity uncertainties on the outcome of clinically relevant personalized forward calculations.

Results:

Quantitative Analysis of Electrophysiological Data

In this chapter, the results of the quantitative analysis methods for intracardiac electrophysiological (EP) recordings are presented. The detailed methods can be found in chapter 6.

Section 10.1 discusses the validation of the cosine-fit analysis. In section 10.2, RBF test interpolations are outlined. In section 10.3, it is demonstrated how the cosine fit could be applied to simulated electrograms from a realistic atrial geometry. Section 10.4 then covers the analysis of patient data with the cosine-fit method and coronary sinus analysis techniques, including test applications of the RBF interpolation for special cases. Finally, in section 10.5, rate-dependent changes in conduction velocity are determined with the cosine-fit method.

10.1 Validation of the Cosine Fit

The cosine fit method estimates incidence direction and conduction velocity (CV) from a single wavefront passing a circular mapping catheter. It was validated in a patch simulation setup [120]. Fig. 6.2(b) on page 56 shows an example of the simulated patch signals for an incidence angle of 130° . It can be seen that activation times were shifted between different electrodes in a sinusoidal pattern altogether (Fig. 6.2(b) and (c)). As in the schematic drawing (Fig. 6.2(a)), the earliest activation was in channel 4-5 and the latest activation in channel 9-10. The activation pattern without artificial noise was quantitatively analyzed with the method described in section 6.1. For the example stimulus at 130° , the calculated incidence direction φ_0 was 132.6° (2.6° error). Simulated data from all 36 stimuli were analyzed with the cosine-fit method. The resulting mean error over all incidence directions with $\delta\gamma = 2^\circ$ and in the absence of artificial noise was 4.2° .

The stability analysis was performed to reveal how different conditions influenced the result quality. The average error of direction estimation for different combinations of

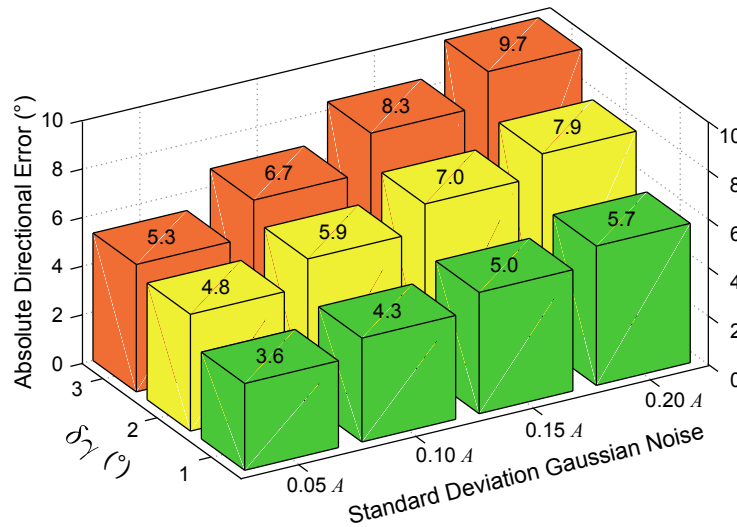


Fig. 10.1. Results of cosine fit stability analysis. Shown is the average directional error for different noise levels and qualities of the catheter geometry estimation. The error ranged between 3.6° (best-case combination with $\sigma = 0.05A$ and $\delta\gamma = 1^\circ$) and 9.7° (worst-case combination with $\sigma = 0.2A$ and $\delta\gamma = 3^\circ$).

σ and $\delta\gamma$ is depicted in Fig. 10.1. The minimum error was 3.6° (for the best-case scenario with $\sigma = 0.05A$ and $\delta\gamma = 1^\circ$), and the maximum error was 9.7° (for the worst-case scenario with $\sigma = 0.2A$ and $\delta\gamma = 3^\circ$). The corresponding 95-quantiles amounted to 8.2° and 21.6° , respectively. Thus, for 95% of all estimated incidence directions, the error was below 8.2° for the best-case parameters and 21.6° for the worst-case setup. It can be seen in Fig. 10.1 that the mean error increased both when noise was added and when the uncertainty in γ increased. However, it remained below 10° for all tested parameter combinations.

Conduction velocity (CV) and mean fit residual were not considerably influenced by $\delta\gamma$. Therefore, only the averages over all values of $\delta\gamma$ for increasing noise level ($\sigma = 0.05A, 0.1A, 0.15A, \text{ and } 0.2A$) are stated for CV and residual. The average CV errors for the respective noise levels were 2.0 cm/s, 3.0 cm/s, 4.1 cm/s, and 5.3 cm/s. The fit residuals amounted to $5 \pm 3 \text{ ms}^2$, $14 \pm 8 \text{ ms}^2$, $30 \pm 17 \text{ ms}^2$, $51 \pm 29 \text{ ms}^2$. The fit residual can be employed to determine the quality of the fit.

For the setup with two colliding waves from 0° and 210° , the cosine-fit calculated an incidence direction of 279° and a fit residual of 151 ms^2 . Comparing the residual to the mean residual of the single-wavefront data with highest noise level ($51 \pm 29 \text{ ms}^2$), the value from the invalid fit was more than three standard deviations higher. Therefore, the high residual is a warning sign that the model was not valid for this case.

10.2 RBF Interpolation

The analysis of simulated data with the RBF interpolation is presented in the following. The RBF interpolation was first applied to the patch simulations used for the cosine-fit validation. Furthermore, colliding wavefronts were separated and ectopic foci could be detected for more advanced catheter designs.

10.2.1 Validation

In order to validate the RBF interpolation method and to compare the results to those from the cosine fit algorithm, RBF interpolation was applied to the same simulated data with artificial noise used in section 10.1. The mean angle errors for increasing noise levels ($\sigma = 0.05A$, $0.1A$, $0.15A$, and $0.2A$) were 2.5° , 3.0° , 3.8° , 4.8° . These errors were around 1 to 1.5° lower than for the cosine-fit analysis with angle uncertainty $\delta\gamma = 1^\circ$. However, no angle uncertainty was assumed for the RBF analysis. If the angle errors for the cosine fit were extrapolated to $\delta\gamma = 0^\circ$, very similar results to those from the RBF interpolation could be expected.

Errors in estimated CV when using RBF interpolation were (for increasing noise level): 2.1, 3.3, 5.2, and 7.6 cm/s. These values were up to 2.5 cm/s higher than for the cosine fit. One source of error might be the occurrence of local extrema in the interpolated LAT field. Such extrema lead to very small numerical gradients and thus very high local CV values. To correct for such errors, data points with local CVs greater 200 cm/s were not included when calculating the mean CV of a single activation pattern. However, the decision which data points to include could further be optimized to reduce such errors.

An error source that has not been considered is the electrode position uncertainty that is present when clinical recordings are analyzed. For example, circular catheters may appear squeezed, i.e. elliptic, probably due to distortions in the localization field. Such errors may for example lead to an over- or underestimation of CV and should therefore be analyzed in future studies.

10.2.2 Detection of Two Colliding Wavefronts

The two colliding wavefronts that were simulated during validation of the cosine-fit method (section 10.1) were analyzed using RBF interpolation. The simulated incidence directions were 0° and 210° . The interpolation results are depicted in Figure 10.2. The RBF interpolation detected incidence directions of 347° and 218° , which corresponds to an error of 13° and 8° .

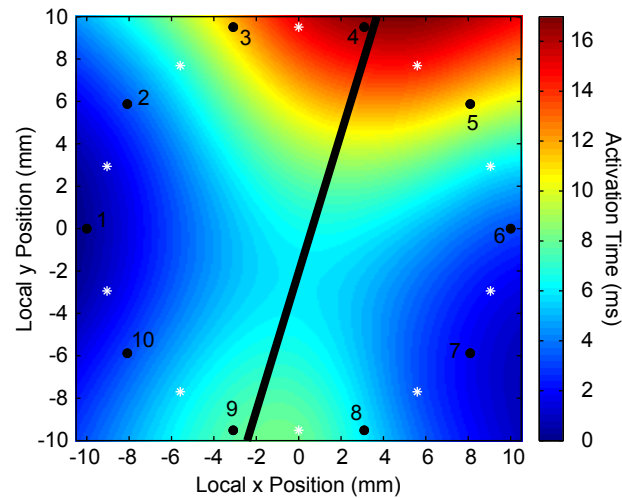


Fig. 10.2. Reconstruction of two colliding wave fronts from directions 0° and 210° (relative to electrode 1 on the left side). The RBF interpolation detects a split line. The incidence angles on the respective sides are 347° (13° offset) and 218° (8° offset). Black dots represent the catheter electrodes, and white dots mark the points between the electrodes that were used as RBF centers for the bipolar EGMs.

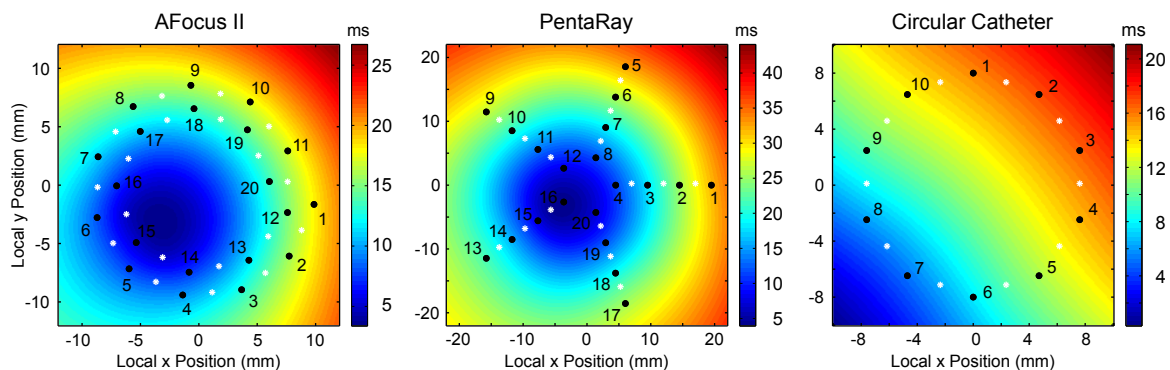


Fig. 10.3. Reconstruction of an ectopic focus using RBF interpolation. For the AFocusII spiral catheter and the PentaRay catheter, the earliest point of activation is reconstructed inside the catheter region at the focus position. In the circular catheter measurement, the ectopic activation cannot be reconstructed. Black dots represent the catheter electrodes, and white dots mark the points between the electrodes that were used as RBF centers for the bipolar EGMs.

10.2.3 Detection of Ectopic Foci

An activation time field for an ectopic focus inside the catheter region was reconstructed using RBF interpolation. Figure 10.2.3 shows the interpolated fields for the AFocusII spiral catheter, the PentaRay catheter, and a standard circular mapping catheter with 10 electrodes. For the AFocusII and the PentaRay, the earliest point of activation was reconstructed inside the catheter region at the focus position. In the circular mapping catheter, the ectopic activation could not be reconstructed. Instead, the result was a plane wave pattern. The advantage of the AFocusII and the PentaRay

Table 10.1. Cosine-fit results for simulated circular catheter on LA roof.

	LA roof						CS	
	t_c (ms)	A (ms)	γ ($^\circ$)	φ_0 ($^\circ$)	Res (ms^2)	CV (cm/s)	Slope ms	CC
Sinus	93.8	10.9	34.6	318	8.7	69	-5.0	-0.71
LSPV	53.0	10.2	36.3	64	4.5	73	15.5	1.0
LIPV	40.9	10.8	35.5	120	6.2	70	6.8	0.72
RIPV	38.9	10.7	37.9	219	2.7	70	-8.9	-0.94
RSPV	53.0	10.2	35.4	287	5.2	73	-7.0	-0.89

catheter is that they also measure radial information, which allows for detection of activation that spreads outwards from the catheter center.

10.3 Electrogram Simulation and Analysis in a Realistic Atrial Data Set

Fig. 10.4 depicts the simulated electrograms for stimulations in the VM atrial data set. Estimation results for the parameters are given in Table 10.1. Obviously, incidence directions significantly differed for stimuli in the LSPV (64°), LIPV (120°), RIPV (219°), and RSPV (287°) as well as in sinus rhythm (318°). The visualization of these directions in Fig. 10.4 shows that they point precisely into the direction of the corresponding stimulation points. The average CV amounted to 71 ± 2 cm/s, corresponding to an error of 1 cm/s compared to the simulated value of 70 cm/s (relative error 1.4%).

The activation times from the CS were characterized by a negative slope and a negative CC for stimuli originating at the right side (NSR, RIPV and RSPV). Thus, proximal electrodes with higher numbers were activated earlier. Stimuli from the left side (LSPV, LIPV), in contrast, showed a positive slope and CC.

10.4 Analysis of Patient Data

The clinical measurements were analyzed with the cosine-fit method and (for data without CS pacing) the CS analysis techniques. For measurements with colliding wavefronts and data from an AFocusII spiral catheter, RBF interpolation was applied. The results for the cosine-fit and the CS analysis are summarized in Tables 10.2 and 10.3 on pages 112/113. For the segments measured during incremental pacing, only the longest pacing cycle length was analyzed. Rate-dependent CV changes for

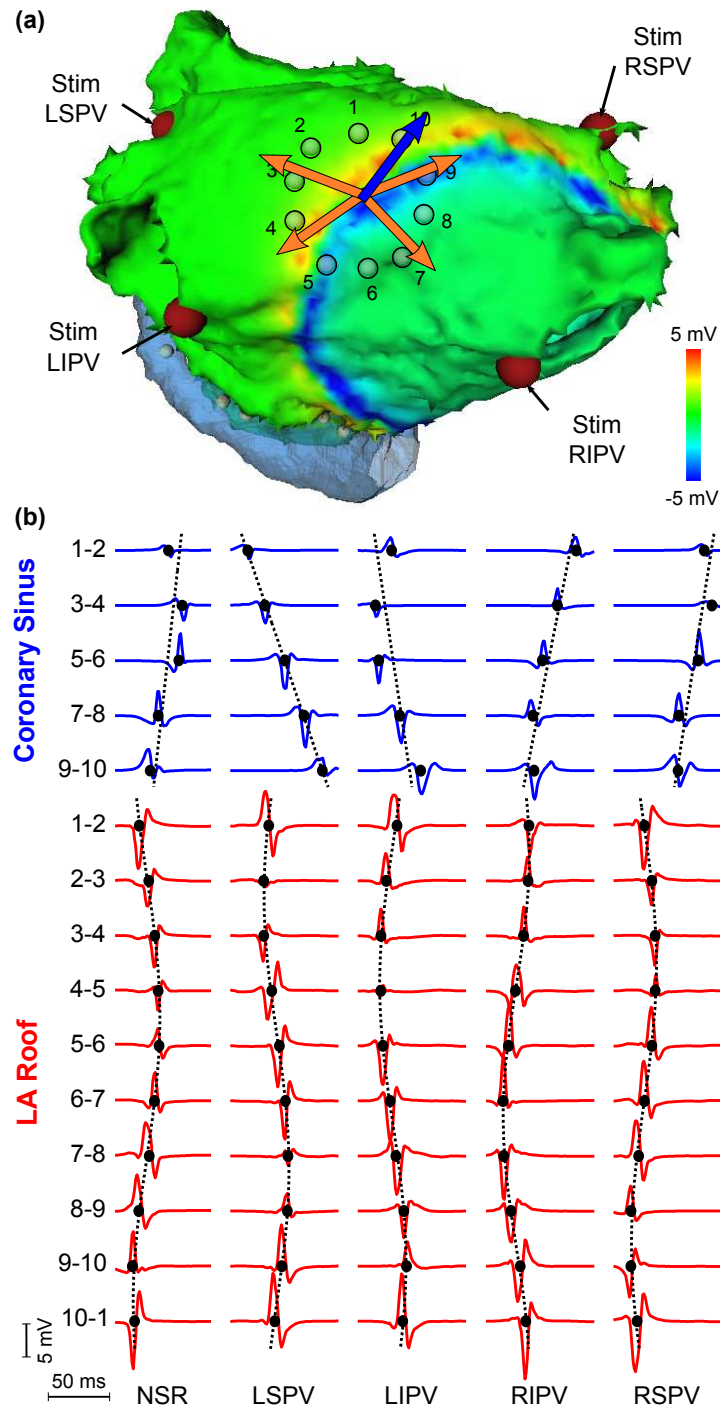


Fig. 10.4. Simulation of circular mapping catheter in the Visible Man LA roof with different PV stimuli [120]. (a) Anterior view of LA with overlaid extracellular potentials for wavefront from RIPV stimulus. The catheter is located on the inner wall of the atrium, but shown here from outside for better visualization. The incidence directions from the PV stimuli (orange) point towards the stimuli origins (red spheres). The blue arrow depicts the direction during NSR and points towards the RA. (b) Simulated electrograms in coronary sinus and circular mapping catheter. Black dots mark the activation times, dotted lines represent the cosine-fit results.

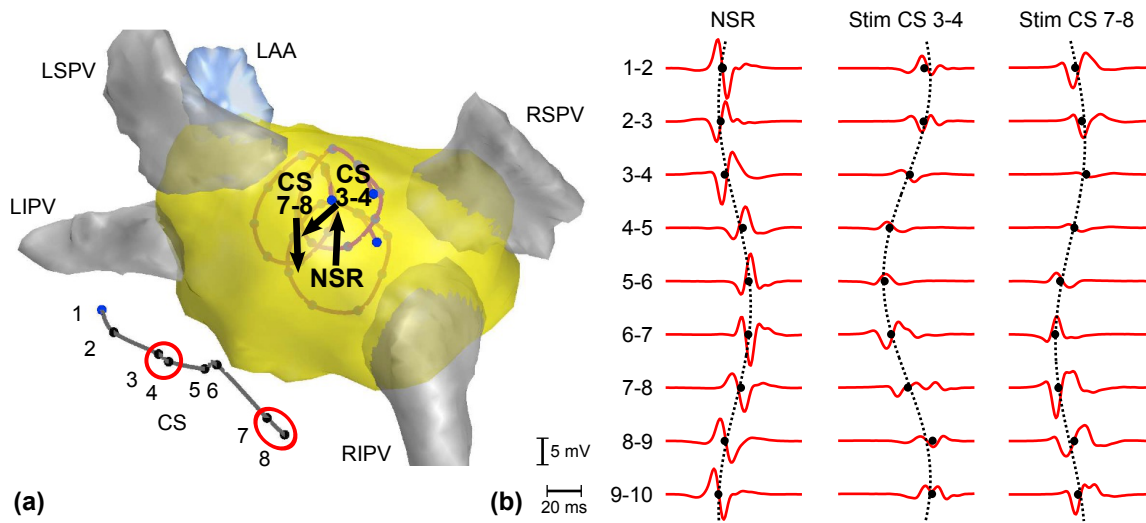


Fig. 10.5. Cosine fit analysis of data from patient 1, segments 1a and 1b [120]. (a) Mapped NavX geometry including catheter positions during NSR and CS stimulation. Electrode 1 is marked blue in each catheter. During NSR, the incidence direction pointed towards the RA where the sinus node is located. Incidence directions under stimulation were directed towards the stimulating CS electrode pairs 3-4 or 7-8. (b) Exemplary electrograms during NSR and pacing. The cosine data model gives a good description of the activation time pattern. The temporal amplitude A of the cosine fit during CS 3-4 pacing was higher compared to NSR and pacing from CS 7-8. This corresponded to a reduced CV.

patients 1 to 5 will be analyzed in detail in section 10.5. Generally, it must be noted that the calculated incidence direction φ_0 depends on the catheter position and orientation. Therefore, results from different patients or catheter positions cannot be directly compared to each other or to the simulated results above.

Patient 1

In patient 1, segment 1a contained six beats of stable sinus rhythm and 18 beats of stimulated excitation from CS electrodes 3-4 with a PCL of 500 ms. During sinus rhythm, the incidence direction was $\varphi_0 = 56 \pm 4^\circ$ and the conduction velocity $CV = 115 \pm 14 \text{ cm/s}$. Under pacing at 500 ms, the values amounted to $\varphi_0 = 211 \pm 4^\circ$ and $CV = 70 \pm 4 \text{ cm/s}$. The resulting directions and example signals are depicted in Fig. 10.5. The second recording, segment 1b, comprised 11 beats of sinus rhythm and 17 beats of stimulated excitation from CS 7-8. In sinus rhythm, the incidence direction was calculated to $\varphi_0 = 51 \pm 5^\circ$ and the CV to $CV = 108 \pm 2 \text{ cm/s}$. During stimulated excitation, the parameters were $\varphi_0 = 268 \pm 20^\circ$ and $CV = 109 \pm 8 \text{ cm/s}$. Incidence directions during NSR pointed towards the RA, whereas incidence directions for beats during pacing pointed towards the respective pacing electrodes (Fig. 10.5). Apart from that, it must be noted how the CV decreased from 115 cm/s for NSR to 70 cm/s for stimulation from CS 3-4. One possible explanation could be fiber orientation that causes a directional dependence of the CV. On the other hand,

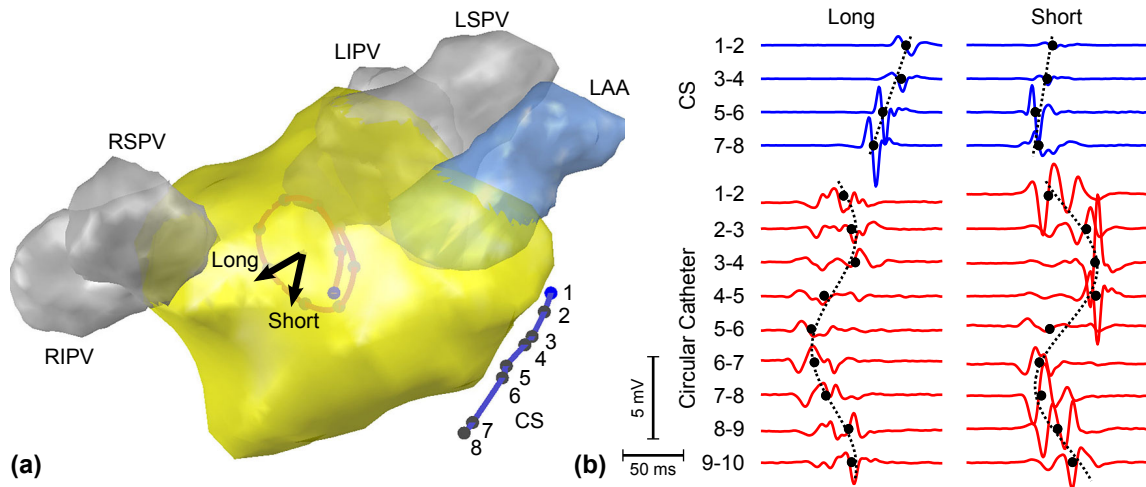


Fig. 10.6. Patient 2, segment 2a from LA anterior wall. (a) Incidence directions for the beats with long and short CLs. (b) Electrograms for beats with long CLs (left column) and short CLs (right column). Circular mapping catheter signals scaled by 3.

the results from [15] showed velocity deviations of more than 80% between stimulations even from opposite directions. This velocity drop will be further discussed in section 10.5.1 where CV changes for shorter CLs are analyzed.

Segments 1c to 1f contained recordings from the CS catheter. Pacing pulses were applied close to the different PVs using the ablation catheter, with one PV per segment. Like in the simulation, CC values were highest (i.e. highest positive or lowest negative values) for the LSPV (-0.27), followed by the LIPV (-0.35), the RSPV (-0.70), and the RIPV (-0.99). In contrast to the simulation results, even the CCs (and slopes from the linear fit) for stimuli on the left side were negative. This could be due to the fact that the clinical stimulation points in the PVs may have been located closer to the LA center, or because the location of the CS catheter may have been different.

Patient 2

Analysis of section 2a showed that there was an alternating conduction pattern. In this patient, an atrial bigeminy was present, i.e. the CLs in the circular mapping catheter alternated between around 1300 ms and 450 ms. When analyzing the segment as a whole, this resulted in a very high CL standard deviation of 432 ms. Therefore, beats with a long and short CL were analyzed separately. Incidence direction was different between the two CLs ($259 \pm 11^\circ$ for long CL vs. $312 \pm 13^\circ$ for short CL), as it is illustrated in Fig. 10.6(a). While the incidence direction for beats with long CL pointed towards the SN, it pointed more downwards for beats with short CL. Furthermore, the mean CC of the CS activation was -0.98 for beats with a long CL, corresponding to a typical right-to-left activation. For beats with a short CL, the mean CC was

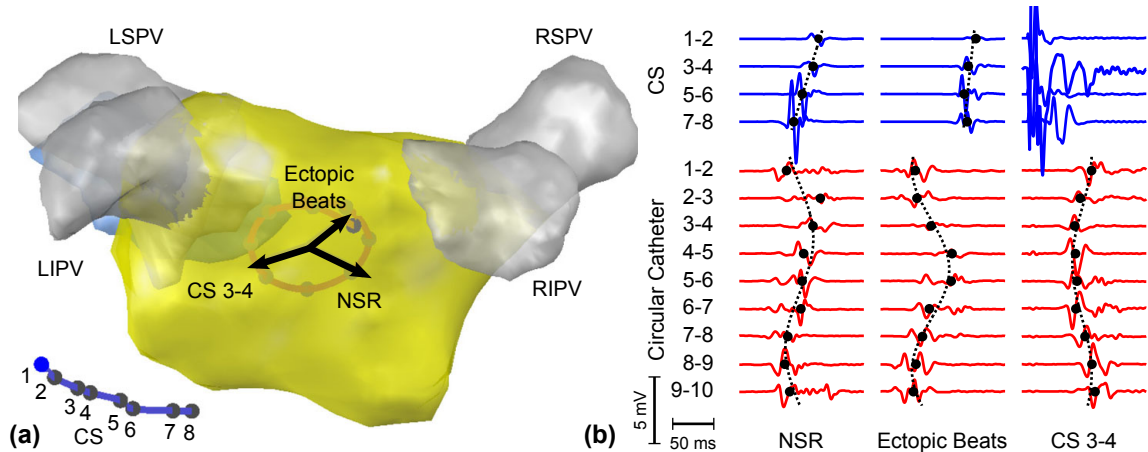


Fig. 10.7. Patient 2, segment 2c from LA posterior wall. (a) Incidence directions of sinus rhythm (NSR), ectopic beats, and during stimulation in the coronary sinus (CS 3-4). (b) Corresponding electrograms. In the CS electrograms during stimulation, large artifacts can be seen during and directly after stimulation. Therefore, no CS electrograms are shown during CS stimulation in all other figures of this work.

-0.62, i.e. the activation did not propagate linearly along the catheter in one direction. The corresponding electrograms are depicted in Fig. 10.6(b), where it can be seen that for beats with short CLs, the first activation typically occurred in channel CS 5-6. A third parameter that was calculated here was the delay between the center of activation in the circular catheter and in the CS catheter. For beats with a long CL, the delay was 49 ± 1 ms, i.e. activation in the CS catheter occurred later than in the circular catheter. For beats with short CL, in contrast, the delay was -9 ± 15 ms, which means that for many beats, activation in the CS catheter preceded the activation in the circular catheter. Therefore, it is likely that the beats with short CL were initiated in the LA. This would mean that every beat from the SN was followed by a premature beat from the LA 450 ms later. However, the question remains why the CL of the premature beat was relatively long compared to the atrial activation time of 100 to 150 ms, and why only one beat followed each sinus beat (there are only two events where a sinus beat was followed by two beats with short CL).

Segment 2b comprised 38 beats during pacing at a CL of 600 ms measured at the anterior LA wall. Several signals contained distortions due to contact between overlapping catheter electrodes. Therefore, one beat was not detected. This led to a doubled CL for the following beat and in its turn to the large standard deviation of 113 ms for the cycle length. Analysis of other beats did not seem to be affected, however. The resulting incidence direction of $336 \pm 23^\circ$ pointed downwards, which was in accordance with the pacing site in the CS.

Recordings in segment 2c were performed on the posterior LA wall. Measurements during NSR showed a very high residual value that was caused by high fractionation

of the electrograms. Example signals are shown in Fig. 10.7. It can be seen that the highest deviation between detected and fitted LAT occurs in the highly fractionated channel 2-3. However, the cosine line crosses the fractionated signal region in this channel, so the cosine can still be assumed to be a valid data model. The incidence direction of $315 \pm 23^\circ$ pointed towards the RA along a line below the RIPV. The recording further contained seven ectopic beats with CLs below 0.9 s, different incidence angles and CCs. Therefore, beats with long (≥ 0.9 s) and short (< 0.9 s) CLs were analyzed separately. The incidence direction for short CLs was $13 \pm 28^\circ$ and pointed into the superior direction towards the LA roof as can be seen in Fig. 10.7(a). Furthermore, the CC showed non-linear activation of the CS catheter with an average CC of -0.68. As can be seen in Fig. 10.7(b), CS 5-6 was the channel with the earliest activation for the ectopic beats. The delay between activation of the circular and the CS catheter was 10 ± 2 ms for beats with a long CL and 34 ± 12 ms for ectopic beats with a shorter CL. Thus, it is very likely that the beats with a shorter CL did not originate in the SN. Comparing these properties to the results from segment 2a for beats with a short CL, the question is if the ectopic beats in segment 2c had the same origin. The CC values were very similar (-0.62 vs. -0.68), which would support this hypothesis. This would then mean that the wavefront caused by the ectopic beat propagated across the LA anterior wall in the superior direction, then posteriorly across the LA roof and inferiorly at the posterior wall. On the other hand, it seems unlikely that such an ectopic focus would be detected in the CS more than 30 ms later than on the posterior wall. It might rather be conducted to the CS faster along the LA inferior wall. Therefore (and also due to the fact that no atrial bigeminy is present as it is the case in segment 2a), it is well possible that different foci were active in the respective segments.

Under pacing from CS 3-4 at a PCL of 500 ms, the incidence angle of $175 \pm 2^\circ$ pointed downwards to the origin of the stimulus. CV during pacing was higher than during NSR (83 vs. 56 cm/s), while at the same time the residual was decreased (205 vs. 609 ms^2). The incidence direction and example electrograms are included in Fig. 10.7.

Results for segment 2d were quite similar to those from segment 2c. Electrograms during NSR also contained one ectopic beat, however, no separate analysis was performed due to the limited overall number of ten beats.

Patient 3

Segments 3a and 3b were recorded at the LA anterior wall. Both segments contained recordings in NSR with an incidence direction pointing obliquely downwards between the SVC ostium and the inferior direction. CVs were 79 and 71 cm/s together

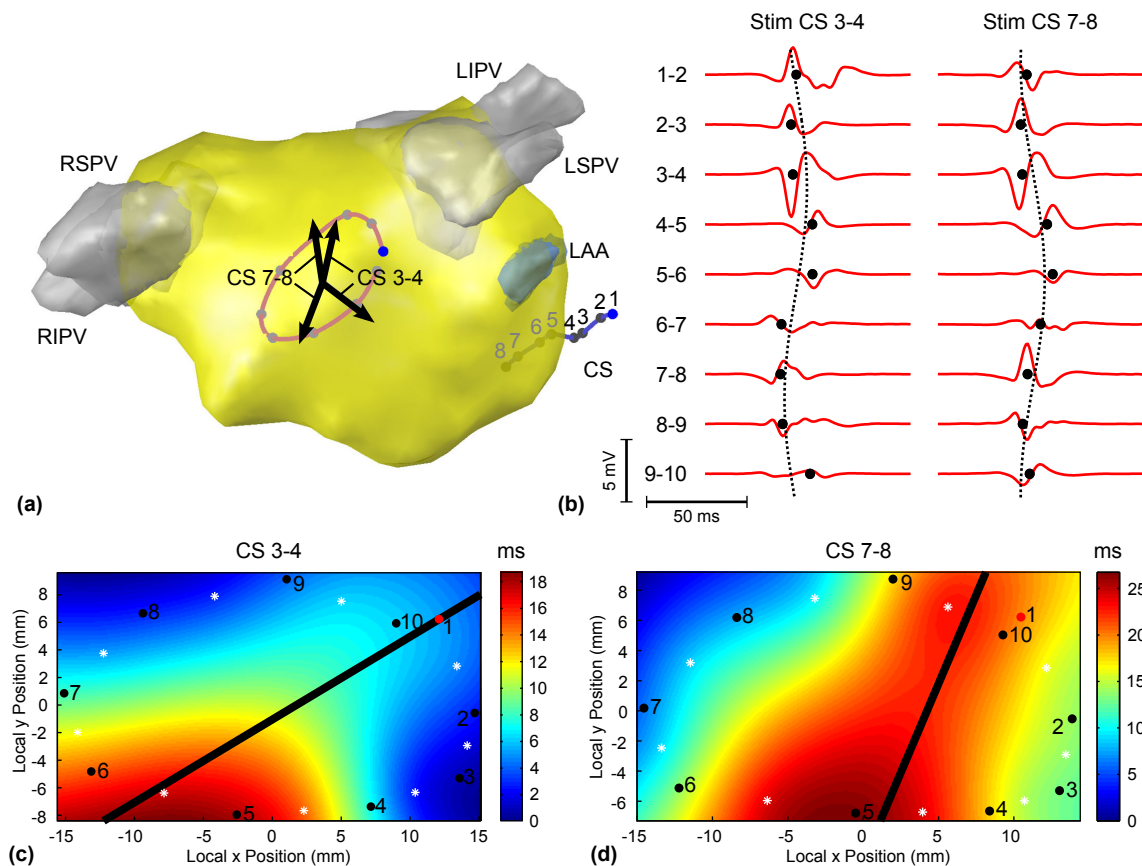


Fig. 10.8. Patient 3, segment 3b, colliding wave fronts were resolved using RBF interpolation. (a) Incidence directions of the two respective fronts during CS 3-4 and CS 7-8 stimulation (CS 3-4: 52° and 298° , CS 7-8: 74° and 224°). (b) Corresponding electrograms. (c,d) Interpolated LAT fields for stimuli from CS 3-4 and CS 7-8. The collision line is marked in black. Note that catheter electrodes are numbered clockwise (i.e. seen from inside the atrium). Thus, directions in the picture cannot be directly compared to (a).

with residuals of 33 and 36 ms^2 . During pacing from CS 3-4 and 7-8 in segment 3b, calculated CV values were strongly increased to 170 or 150 cm/s respectively, which appears unphysiologically high and suggests a detection error. Compared to the NSR measurements, the residual was strongly increased for CS 3-4 pacing (316 ms^2), but only moderately for CS 7-8 pacing (89 ms^2). However, when looking at the LATs, it seems very probable that the LAT pattern was caused by two colliding wavefronts for both pacing cases. Therefore, a smaller amplitude was obtained from the cosine fit that resulted in a falsely increased value for the CV. The patterns from these wavefronts were therefore analyzed with the RBF interpolation method to test the hypothesis of colliding wavefronts as described in section 6.2.4. As can be seen in Figure 10.8, two colliding wave fronts were indeed detected for each of the stimulations. The corresponding incidence directions were 52° and 298° for CS 3-4, and 74° and 224° for CS 7-8.

Segments 3c and 3d were recorded at the LA posterior wall. Segment 3d contained two pacing sequences, one from CS 3-4 and another one from CS 3-7. During NSR, incidence directions in both segments pointed across the LA roof towards the RA. The absolute incidence angles differed due to a different catheter position and orientation. For the second NSR section, the CV standard deviation from the CS electrograms was increased because during the last analyzed beat, pacing already started in the CS catheter and interfered with LAT detection. The incidence direction during the stimulations pointed downwards into the direction of the CS catheter.

Patient 4

Segment 4a was recorded on the anterior LA wall. It comprised 20 beats of NSR and 15 beats of pacing from CS 3-4 at a CL of 600 ms. Incidence directions pointed towards the SN during NSR and along a line probably above the mitral valve during pacing (Fig. 10.9). Segment 4b contained 41 beats measured at the LA anterior wall during pacing from CS 7-8. Here, the wave front may have passed *below* the mitral valve before detection in the catheter. This points out the role of the mitral valve as a geometrical obstacle.

The measurements in segments 4c, 4d, 4e, and 4f were performed at the LA roof. Analysis of segment 4c yielded an incidence direction of $91 \pm 9^\circ$ that pointed towards the stimulating CS 3-4 electrodes. Segment 4d contained recordings of NSR, in which the incidence direction pointed towards the RA. Results from the following stimulation sequence from CS 3-4 with a PCL of 600 ms were quite consistent with those from segment 4c with a PCL of 500 ms. Segment 4e (stimulation from CS 7-8) resulted in very similar incidence direction than those observed in 4c and 4d, i.e. pointing rather towards the CS 3-4 electrodes. However, it was confirmed by the recorded CS electrograms that pacing pulses were indeed applied in the CS 7-8 electrodes. Therefore it is likely that anisotropic conduction along the LA posterior wall led to a conduction path between pacing and recording site which did not correspond to the direct connection along the tissue surface. Segment 4f contained another recording during stimulation from CS 7-8 which produced similar results.

Patient 5

In patient 5, segment 5a from the RA lateral free wall contained six beats of stable sinus rhythm before pacing was initiated. The incidence direction was calculated to $\varphi_0 = 316 \pm 3^\circ$ and the CV to 79 ± 3 cm/s. Stimulation from the ablation catheter close to the sinus node yielded $\varphi_0 = 308 \pm 4^\circ$ and $CV = 76 \pm 4$ cm/s for the 13 recorded beats. Both directions pointed towards the sinus node.

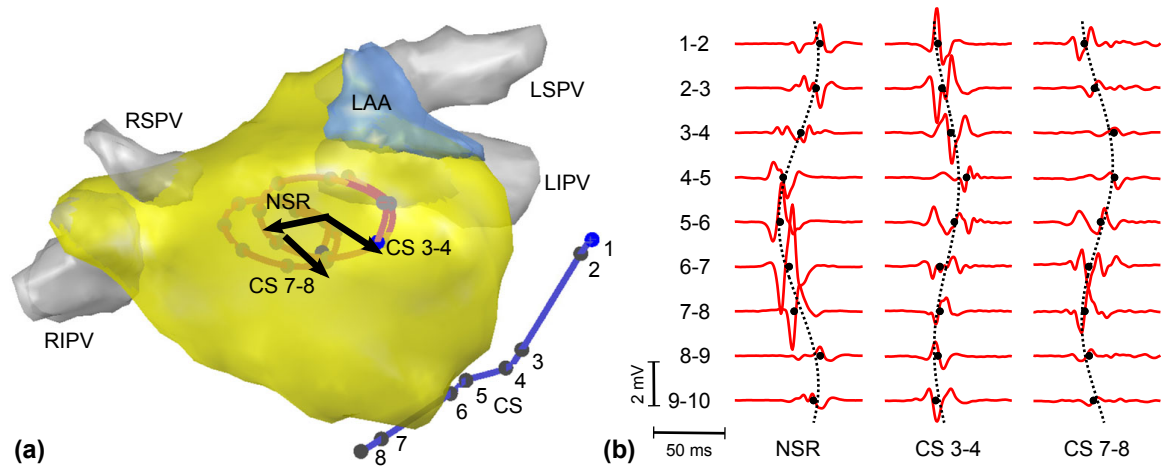


Fig. 10.9. Patient 4, segments 4a and 4b. (a) Incidence directions during NSR, CS 3-4 and CS 7-8 stimulation. (b) Corresponding electrograms (CS 7-8 scaled by 2).

Segment 5b from the posterior RA wall comprised 20 beats of stable sinus rhythm with $\varphi_0 = 10 \pm 8^\circ$ and $CV = 97 \pm 2$ cm/s. During stimulation from the CS, the incidence direction was shifted approximately 90° down towards the CS.

It is interesting to note that unlike in all other segments, the CC from the CS signals was very close to zero. This was due to the fact that activation in the distal electrode pair CS 7-8 was delayed.

Patient 6

Data from patient 6 contained 91 beats of stable sinus rhythm. The incidence direction was $\varphi_0 = 312 \pm 2^\circ$ and the conduction velocity $CV = 91 \pm 4$ cm/s. The incidence direction pointed towards the RA.

Patient 7

Data in patient 7 comprised 59 beats and was measured at the anterior LA wall with an AFocusII spiral catheter. It was therefore analyzed with the RBF interpolation method. The resulting incidence directions during NSR and CS 7-8 pacing were $276 \pm 2^\circ$ and $38 \pm 7^\circ$. They are shown in Figure 10.10 together with the corresponding electrograms and interpolated LAT fields. The average CV was 87 ± 5 cm/s during NSR and 65 ± 10 cm/s during CS 7-8 pacing.

Table 10.2. Results of patient data analysis (cosine fit and CS analysis) for patients 1 to 3

Seg	Comment	Len (s)	Beats	CL (s)		ϕ_0 (°)		CV (cm/s)		Res (ms ²)		CC CS		CS slope (ms)	
				Mean±Std	Std	Mean±Std	Std	Mean±Std	Std	Mean±Std	Std	Mean±Std	Std		
1a	NSR	6	6	1,088±0,032		56±4		115±14		12±4		-0,904±0,011		-0,0079±0,0003	
1a	PCL 500 ms	9	18	0,500±0,001		211±4		70±4		45±16		n/a		n/a	
1b	NSR	13	11	1,108±0,018		51±5		108±2		11±3		-0,920±0,013		-0,0078±0,0003	
1b	PCL 500 ms	8	17	0,501±0,002		268±20		109±8		28±11		n/a		n/a	
1c	Stim LSPV (CS only)	52	103	0,501±0,238		n/a		n/a		n/a		-0,265±0,176		-0,0014±0,0018	
1d	Stim LIPV (CS only)	54	116	0,462±0,199		n/a		n/a		n/a		-0,349±0,422		-0,0019±0,0025	
1e	Stim RIPV (CS only)	43	102	0,429±0,149		n/a		n/a		n/a		-0,989±0,028		-0,0090±0,0012	
1f	Stim RSPV (CS only)	40	98	0,403±0,080		n/a		n/a		n/a		-0,701±0,118		-0,0024±0,0006	
2a	Alternating pattern	68	78	0,861±0,432		286±29		44±9		358±239		-0,796±0,284		-0,0063±0,0038	
2a	long CL	0	38	1,307±0,019		259±11		49±2		157±72		-0,984±0,005		-0,0099±0,0003	
2a	short CL	0	40	0,449±0,010		312±13		39±11		550±175		-0,619±0,304		-0,0029±0,0017	
2b	PCL 600 ms	23	38	0,628±0,113		336±23		58±6		366±185		n/a		n/a	
2c	NSR and ectopic beats	91	95	0,956±0,091		315±23		56±6		609±207		-0,971±0,091		-0,0092±0,0019	
2c	NSR only		88	0,973±0,062		310±15		57±5		636±189		-0,995±0,003		-0,0097±0,0006	
2c	Ectopic beats only		7	0,735±0,110		13±28		49±7		274±124		-0,676±0,134		-0,0029±0,0012	
2c	PCL 500 ms	21	42	0,503±0,013		175±2		83±9		205±78		n/a		n/a	
2d	NSR	9	10	0,952±0,171		315±21		59±4		630±176		-0,978±0,042		-0,0090±0,0017	
2d	PCL 600 ms	17	29	0,601±0,004		177±2		75±4		172±53		n/a		n/a	
3a	NSR	35	29	1,178±0,031		230±11		79±5		33±14		-0,973±0,009		-0,0067±0,0004	
3b	NSR	9	8	1,095±0,027		234±4		71±3		36±9		-0,976±0,029		-0,0063±0,0007	
3b	CS 7-8	24	46	0,504±0,022		49±72		170±35		316±86		n/a		n/a	
3b	CS 3-4	20	38	0,512±0,068		29±11		150±26		89±26		n/a		n/a	
3c	NSR	28	24	1,168±0,022		227±7		125±7		25±4		-0,978±0,005		-0,0065±0,0003	
3d	NSR	8	6	1,255±0,020		167±14		130±15		40±21		-0,964±0,026		-0,0051±0,0005	
3d	PCL 600 ms CS 3-4	11	19	0,601±0,002		29±7		96±8		92±38		n/a		n/a	
3d	NSR	7	7	1,030±0,058		230±4		117±15		28±9		-0,896±0,268		-0,0056±0,0016	
3d	PCL 600 ms CS 7-8	16	26	0,604±0,017		18±15		103±4		58±8		n/a		n/a	

Table 10.3. Results of patient data analysis (cosine fit and CS analysis) for patients 4 to 6

Seg	Comment	Len		Beats		CL (s)		ϕ_0 ($^\circ$)		CV (cm/s)		Res (ms ²)		CC CS		CS slope (ms)	
		(s)		Mean \pm Std	Std	Mean \pm Std	Std	Mean \pm Std	Std	Mean \pm Std	Std	Mean \pm Std	Std	Mean \pm Std	Std	Mean \pm Std	Std
4a	NSR	20	20	1,036 \pm 0,023		218 \pm 3		49 \pm 1		102 \pm 7		-0,856 \pm 0,042		-0,0095 \pm 0,0006			
4a	PCL 600 ms	9	15	0,601 \pm 0,001		351 \pm 9		85 \pm 8		157 \pm 19		n/a		n/a			
4b	PCL 500 ms	21	41	0,501 \pm 0,004		345 \pm 7		64 \pm 6		156 \pm 137		n/a		n/a			
4c	PCL 500 ms	15	30	0,500 \pm 0,007		91 \pm 9		95 \pm 19		56 \pm 45		n/a		n/a			
4d	NSR	19	18	1,067 \pm 0,014		269 \pm 2		104 \pm 5		15 \pm 1		-0,941 \pm 0,012		-0,0124 \pm 0,0005			
4d	PCL 600 ms	16	26	0,601 \pm 0,004		103 \pm 9		93 \pm 8		51 \pm 17		n/a		n/a			
4e	NSR	11	11	1,038 \pm 0,016		271 \pm 1		100 \pm 8		15 \pm 6		-0,939 \pm 0,019		-0,0118 \pm 0,0009			
4e	PCL 500 ms	11	22	0,501 \pm 0,001		83 \pm 3		81 \pm 9		34 \pm 12		n/a		n/a			
4f	NSR	15	15	1,036 \pm 0,015		272 \pm 2		111 \pm 6		9 \pm 3		-0,949 \pm 0,006		-0,0126 \pm 0,0002			
4f	PCL 600 ms	10	16	0,601 \pm 0,002		88 \pm 5		85 \pm 7		31 \pm 9		n/a		n/a			
5a	NSR (IEEE range)	5	6	0,949 \pm 0,008		316 \pm 3		79 \pm 3		67 \pm 48		-0,049 \pm 0,093		-0,0002 \pm 0,0004			
5a	PCL 500 ms	6	13	0,499 \pm 0,007		308 \pm 4		76 \pm 4		50 \pm 21		n/a		n/a			
5b	NSR	17	20	0,878 \pm 0,076		10 \pm 8		97 \pm 2		63 \pm 21		-0,088 \pm 0,207		-0,0005 \pm 0,0013			
5b	PCL 500	5	10	0,501 \pm 0,003		98 \pm 8		70 \pm 7		321 \pm 95		n/a		n/a			
6a	NSR	70	91	0,773 \pm 0,003		312 \pm 2		91 \pm 4		19 \pm 8		-0,999 \pm 0,001		-0,0114 \pm 0,0003			

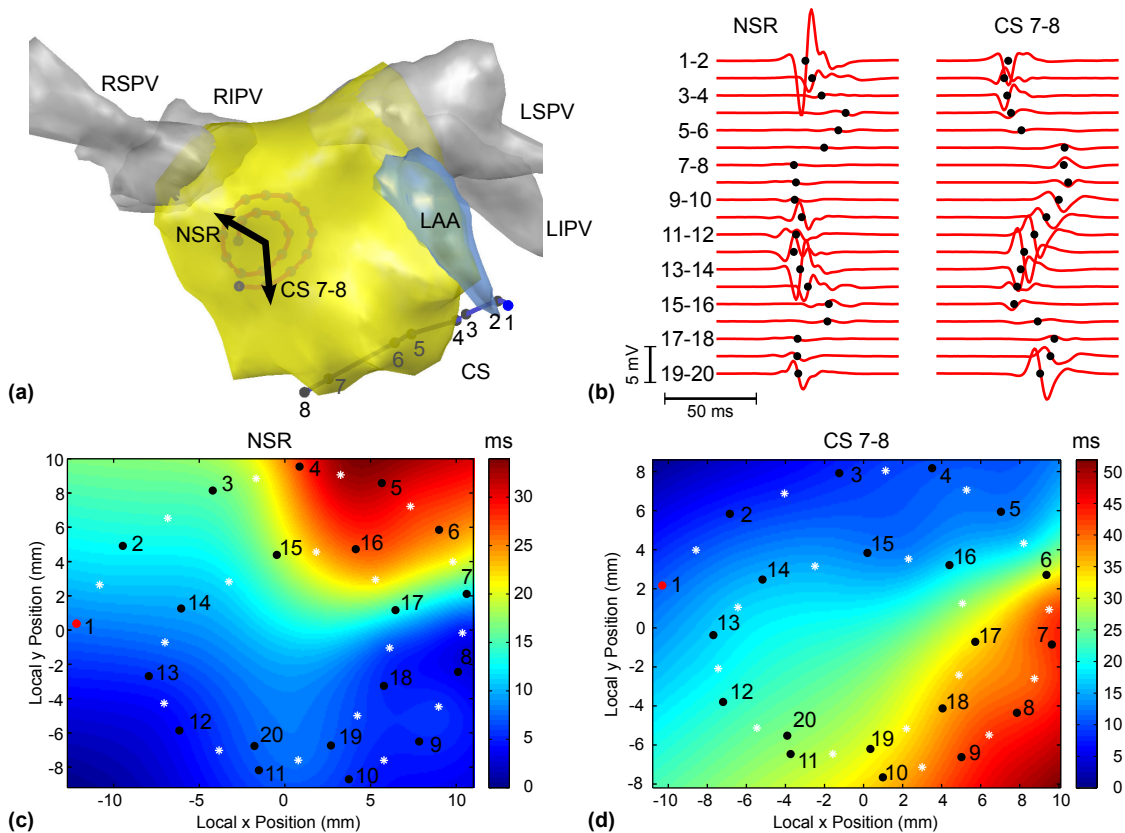


Fig. 10.10. Patient 7, segment 7a. (a) Incidence directions in the AFocusII catheter during NSR and CS 7-8 stimulation. (b) Corresponding electrograms. (c, d) Interpolated LAT fields for NSR and CS 7-8 stimulation. Note the arrangement of electrodes when comparing the field to the catheter position from (a).

10.5 CV Restitution Curves

Analysis of CV restitution was performed in patients 1 to 5, in which recordings from incremental pacing at the LA roof or LA posterior wall were available (segments 1a, 1b, 2d, 3d, 4e, 4f, and 5a).

Local CV typically decreased for shorter pacing cycle lengths. The mean local CV over the considered patients was 108 ± 14 cm/s during NSR, 86 ± 15 cm/s during pacing at 500 ms, and 77 ± 20 cm/s during pacing at 300 ms. In the LA, local CV values ranged between 104 and 120 cm/s during NSR, between 70 and 109 cm/s during pacing at 500 ms, and between 47 cm/s and 107 cm/s during pacing at 300 ms. In the RA measurement, local CV was 79 cm/s during NSR, 76 cm/s at a PCL of 500 ms and 70 cm/s at 300 ms. Table 10.5.1 summarizes absolute CV values and changes between pacing at a cycle length of 500 ms and 300 ms. Fig. 10.13 shows example restitution curves.

Table 10.4. CV restitution analysis results for different pacing sequences.

Pat	Meas Site	Stim Site	No Beats		Residual (ms ²)	Local CV (cm/s)			Local CV		Global CV	
			Incl	Excl		NSR	PCL 500	PCL 300	Rel	P	Rel	P
1	LA roof	CS 3-4	94	7	31± 25	113±10	70± 4	107±12	53%	<0.001	2%	n.s.
		CS 7-8	105	6	23± 13	108± 2	109± 9	101± 4	-7%	<0.01	7%	<0.001
2	LA post	CS 3-4	123	7	331±166	(n/a)	80± 7	47± 6	-42%	<0.001	-25%	<0.001
3	LA roof	CS 3-4	123	13	116± 83	120±11	84± 8	82±14	-2%	n.s.	-16%	<0.001
		CS 7-8	132	8	115± 81	120±16	108± 4	70±15	-35%	<0.001	-39%	<0.001
4	LA roof	CS 3-4	117	8	61± 73	104± 5	82±11	69*±17	-16%	<0.05	-6%	<0.05
		CS 7-8	137	9	64± 74	111± 8	76± 9	67±10	-12%	<0.01	-14%	<0.001
5	RA FW	SN	100	6	100± 59	79± 9	76± 4	70± 6	-8%	<0.001	-2%	<0.05

* value at PCL 350 ms.

10.5.1 Individual Results from Different Patients

In the following, results obtained from the different patients are explained in detail.

Patient 1

In contrast to the majority of measurements, patient 1 showed a remarkable CV change of inverse nature. Local CV during NSR was approximately 110 cm/s. After the start of pacing from CS 3-4, local CV directly dropped from around 110 cm/s during NSR to 70 cm/s. At shorter PCLs, however, the local CV then increased step by step (Fig. 10.12(a)). At the shortest PCL of 300 ms, the CV of 107 cm/s was again close to the value during NSR. This corresponded to an increase of 53% ($P<0.001$) between pacing at 500 and 300 ms. Global CV, in comparison, did not change significantly. During CS 7-8 pacing, local CV decreased by 7% ($P<0.01$) whereas global CV increased by 7% ($P<0.001$). Apart from that, the global CV showed a larger increase between 500 and 400 ms than between 500 and 300 ms for both pacing sites.

Patient 2

Patient 2 showed a strong decrease in both local and global CV between PCLs 500 and 300 ms as can be seen in Figure 10.12(b). Local CV decreased by 42% ($P<0.001$) and global CV by 25% ($P<0.001$). The local CV decrease of 42% was the highest decrease observed in the patients under study. It must be noted for patient 2 that the residual from the cosine fit ($331\pm 166\text{ ms}^2$) was considerably higher than in other measurements. This was mainly caused by a higher electrogram fractionation. As a result, electrograms were broadened and the detection uncertainty in the activation times was increased, which also increased the fit residual. However, despite the increased residual, it can be seen in Fig. 10.11 that the cosine data model still represented the activation pattern and therefore was a valid assumption.

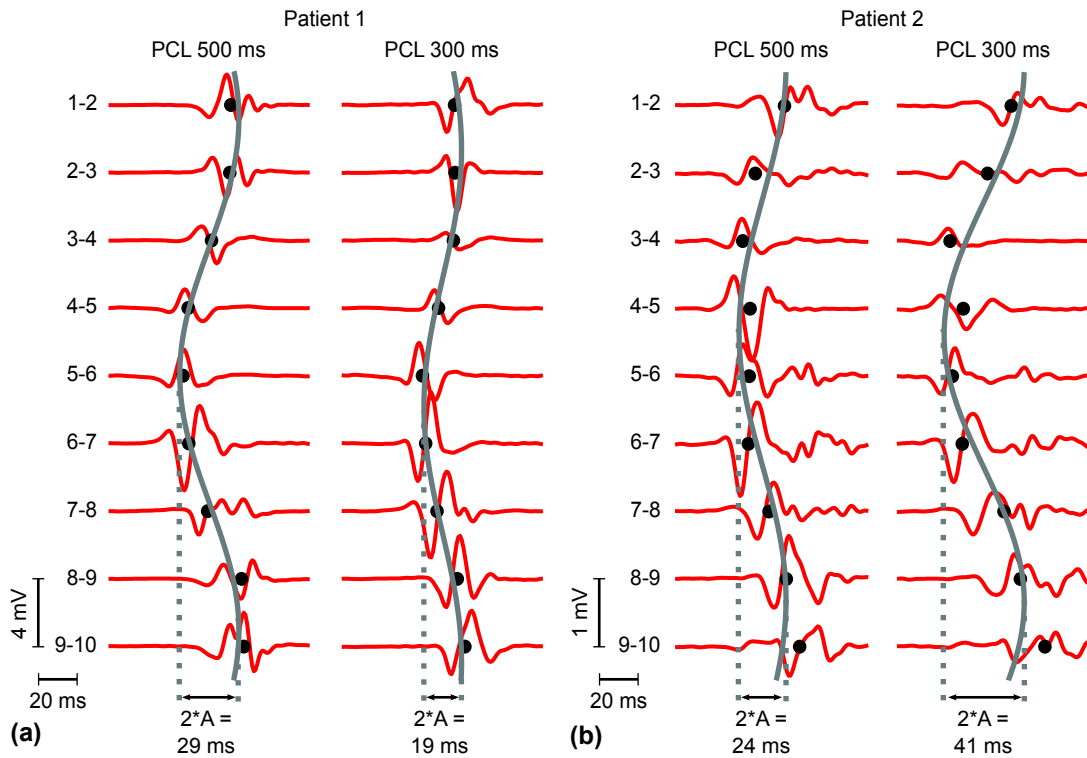


Fig. 10.11. Example electrograms for pacing at 500 and 300 ms with resulting cosine-fits. (a) Electrograms from patient 1 (CS 3-4). The strong and atypical increase in CV is reflected by the decrease in cosine amplitude A from 14.6 ms (at 500 ms PCL, left column) to 9.3 ms (at 300 ms pacing, right column). (b) Electrograms from patient 2. Due to conduction slowing, the time amplitude of the cosine increases from 12.0 ms to 20.5 ms. Fits in this patient had a high average residual of 331 ms² due to low signal amplitude and high electrogram fractionation, as can be seen by the lower voltage scale compared patient 1. However, the cosine is still a valid data model as it represents the general shape of the activation pattern.

Patient 3

For patient 3 during pacing from CS 3-4, the local CV change was not significant (84 ± 8 cm/s at 500 ms vs. 82 ± 14 cm/s at 300 ms). However, local CV changes showed a rather triphasic behaviour. The CV at 600 ms was 96 cm/s and decreased to about 85 cm/s at 500 and 450 ms. During faster pacing at 400 and 350 ms, it increased again to around 92 cm/s, and finally went down to 82 cm/s at 300 ms. Comparing local CVs between PCLs 600 ms (instead of 500 ms) and 300 ms, there was a significant decrease of 15% ($P < 0.001$). The global CV, in contrast, monotonically decreased by 15% ($P < 0.001$) not only compared to the value at 600 ms, but also compared to the value at 500 ms. An explanation might be that local variations might have cancelled each other out, for example, in regions of discordant alternans [132, 151]. During pacing from CS 7-8, both local and global CV were strongly decreased by 35% and 39% ($P < 0.001$). Fig. 10.13(a) shows the corresponding restitution curves that were quite similar to those from patient 2. Furthermore, as in patient 2, the CV at 500 ms

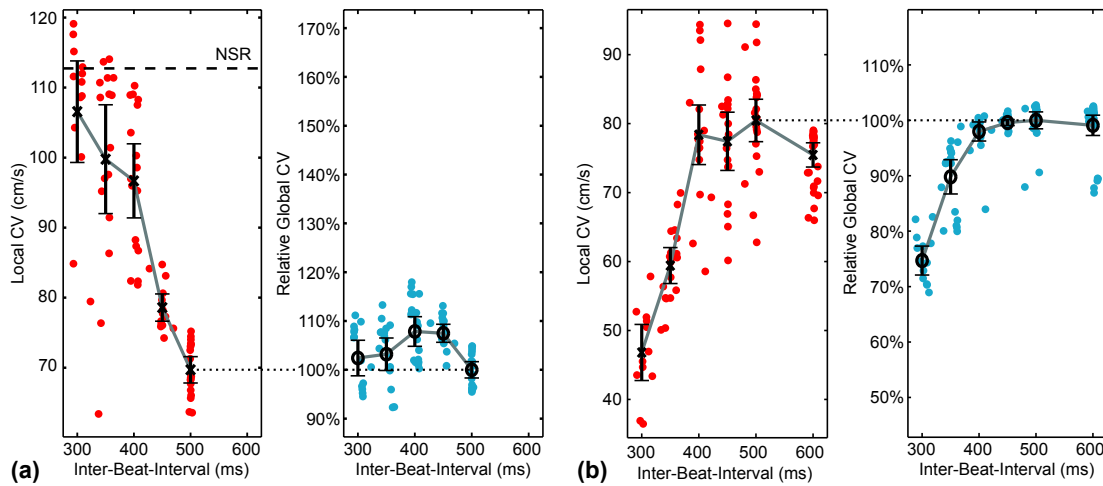


Fig. 10.12. Restitution curves for local and global CV. The y-axis of the global CV was aligned such that the 100% value of global CV was at the same level as the local CV at 500 ms (marked with dotted line). The global CV range matches the local CV range in relative units to make both plots comparable. The local CV at NSR is given by a dashed line for comparison. (a) CV restitution for patient 1 during pacing from CS 3-4. The local CV on the LA roof (left panel) showed a strong increase of 53% ($P < 0.001$), while the mean global CV (right panel) only increased slightly by 2% ($P = \text{n.s.}$). (b) Data for patient 2. Local CV on the LA posterior wall was reduced by 42% ($P < 0.001$) and global CV by 25% ($P < 0.001$).

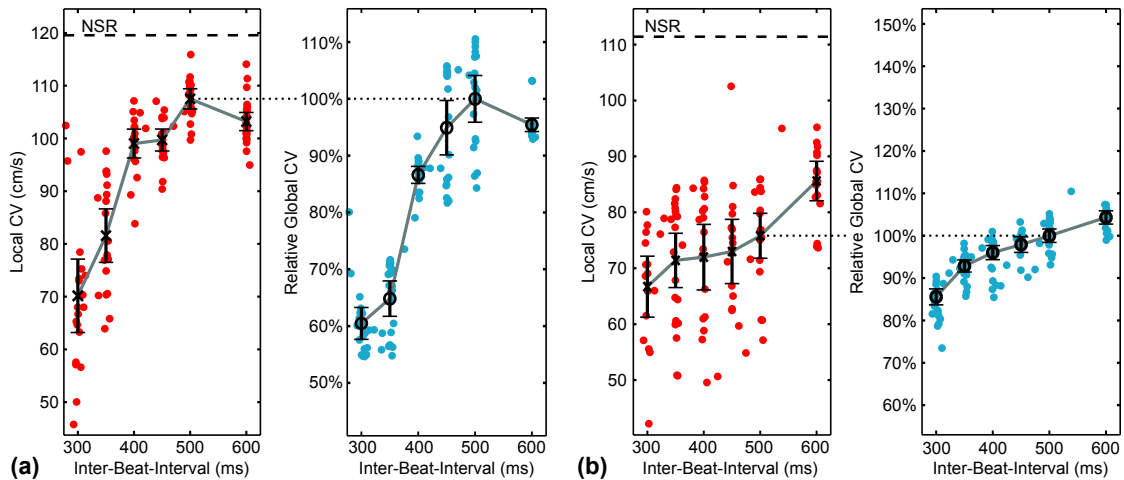


Fig. 10.13. CV restitution in patients 3 and 4. (a) Data from patient 3 under CS 7-8 pacing. Between pacing at 500 and 300 ms, local CV on the LA posterior wall was decreased by 35% ($P < 0.001$) and global CV by 39% ($P < 0.001$). (b) In patient 4 under CS 7-8 pacing, local CV on the LA roof was reduced by 12% ($P < 0.01$) and global CV by 14% ($P < 0.001$).

was slightly higher than at 600 ms. This phenomenon is referred to as supernormal conduction, i.e. increased CV for shorter pacing intervals.

Patient 4

In patient 4 (CS 3-4 pacing), the local CV decreased by 16% ($P < 0.05$) and the global CV by 6% ($P < 0.05$). During pacing at 300 ms, rhythm was no longer reg-

ular (whereas after termination of pacing, NSR was restored immediately). Therefore, data from PCL 300 ms were not considered, and statistics were calculated between 500 and 350 ms. During pacing from CS 7-8, the local CV decreased by 12% ($P < 0.01$) and the global CV by 14% ($P < 0.001$). Fig. 10.13(b) depicts the restitution curves.

Patient 5

In patient 5, local CV decreased by 8% ($P < 0.001$) and global CV by 2% ($P < 0.05$). These were rather small changes, but they still were significant. Furthermore, it is interesting to note that the global CV dropped by 4% between 500 and 400 ms, but increased again for shorter PCLs.

10.6 Discussion

In this chapter, intracardiac electrograms were simulated, and quantitative methods were presented to analyze data that is frequently acquired during routine EP studies. A cosine-fit method estimated the wave direction (represented by the incidence direction) and conduction velocity from intracardiac EGMs recorded with circular mapping catheters. An extension of the RBF interpolation method proposed in [84] for simulated data was used to interpolate local activation times in the catheter region from which incidence direction and CV were estimated. It can be applied to universal catheter geometries such as the PentaRay or AFocusII catheter. An analysis for activation of the CS catheter was proposed based on linear correlation between activation time and pair number or based on linear regression.

These methods are not based on activation time maps of the whole atrium, but are instead capable of single-shot analysis of individual wavefronts passing the catheter. Thus, they are able to capture singular events such as ectopic beats or limited numbers of wavefronts excited by stimulations. Repetitive measurements of stable patterns can of course reduce measurement uncertainties.

All methods have been demonstrated to be applicable for the analysis of measurement data from patients. Furthermore, rate dependent changes in CV were analyzed with the cosine-fit method.

10.6.1 Simulation and Analysis of Intracardiac Electrograms

Intracardiac electrograms could be simulated in three steps: calculating transmembrane voltage distributions, forward-calculating the extracellular potentials, and extracting the catheter signals at the center of the metal electrodes in the model. With

simulated electrograms from a tissue patch, the proposed analysis methods could be validated.

In the stability analysis, different levels of noise were added to the detected activation times. It must be emphasized that by adding noise directly to the activation times, all possible sources of noise were considered, regardless of the underlying mechanisms. As could be expected, the directional estimation of the cosine-fit was better for lower noise levels and more exactly determined catheter geometries. But even in the worst-case scenario, the average directional error was below 10° . This is an enormous improvement compared to just visually selecting the channel of earliest activation. In the latter case, a deviation of one channel already amounts to an error of 30° to 40° or even more, depending on the catheter geometry. CV estimation was almost independent of the catheter geometry parameter $\delta\gamma$. The average CV error only increased for higher noise levels, but was less than 5.4 cm/s even for the highest noise level. This corresponds to approximately 5% to 10% of typical CV values (50 to 100 cm/s). The setup with two wavefronts colliding under the catheter showed a significantly increased fit residual.

The cosine fit and the RBF interpolation showed similar estimation qualities. Angle errors were 1-1.5° smaller with the RBF interpolation, however, it assumed that the catheter geometry was exactly known (which was the case in the simulation). On the other hand, CV errors were up to 2.5 cm/s lower for the cosine fit.

A restriction of the cosine-fit is the assumption of a single wavefront passing over a circular mapping catheter. However, this assumption covers a large number of measurements, e.g., during atrial flutter and during mapping of patients suffering from paroxysmal AF who are measured during NSR. Circular mapping catheters are frequently used in clinical practice, therefore, the cosine model is applicable to a large amount of intracardiac EGMs.

For two colliding wavefronts or different catheter types, RBF interpolation can be used. It is a more general approach, because in theory, arbitrary catheter setups and excitation patterns can be reconstructed. However, this also makes the approach more error-prone. For example, if catheter positions recorded with electroanatomical mapping systems are used as interpolation centers, geometrical distortions of the electrode positions may lead to over- or underestimations of the CV. Such influences must be evaluated in future studies concerning the stability of the RBF interpolation. The cosine fit in contrast assumes a circular catheter shape. Fluoroscopic images of the circular catheters during the examinations were not analyzed systematically, however, when sporadically looking at such pictures, the real catheter geometry rather appeared to be circular. In such cases, the results of the cosine fit are more reliable

than those of the RBF interpolation. Therefore, clinical data were quantitatively analyzed with the cosine-fit method, and only in cases of wavefront collisions or for measurements with the AFocusII spiral catheter, RBF interpolation was applied.

It must be noted that incidence directions are measured in the local catheter coordinate system. If the catheter is rotated, the results change even if the activation pattern is the same. Therefore, the catheter position and orientation must be considered when comparing measurements from different sites. However, this is easily possible, because the local directions from different sites can be combined into a common geometric model. Furthermore, local incidence directions do not necessarily point towards the stimulation origin, e.g. if conduction is anisotropic due to fiber orientation. Also for spiral waves that can be present during atrial arrhythmias, incidence directions may not always point directly towards the spiral wave center.

Typical catheter diameters are in the range of 20 mm, therefore, only macroscopic wavefronts can be analyzed. Substrate changes such as microfibrosis may induce local micro-conduction phenomena and complex fractionated electrograms [78]. For the study of such micro-conduction, sensors with higher resolution have been used in tissue preparations [87].

Activation times in the *bipolar* electrograms were detected with the NLEO operator. To determine activation times in *unipolar* signals, the maximum negative derivative can be used. For bipolar signals like in this work, however, the NLEO appears to be a more suitable approach, because it is, e.g., independent of the sign of the signal. Furthermore, it allows to determine the signal center (instead of e.g. the onset). This is necessary because only the center of activation has a defined spatial connection with the point between the two electrodes. Generally, the proposed analysis techniques can be used with both uni- and bipolar signals.

A realistic anatomical model was used to simulate intracardiac EGMs for stimulations in all four PVs. The signals were quantitatively analyzed with the cosine-fit method. Then it was distinguished between the stimuli origins based on the local incidence direction. This shows how the analysis can extract clinically-relevant data from simulation models. Such data are useful to parametrize the electrophysiology of patient-specific models and to validate the simulation results.

10.6.2 Analysis of Clinical Measurements

From clinical intracardiac EGMs, the cosine-fit analysis reliably extracted incidence directions and conduction velocities. Detected incidence directions were in good agreement with expected values. Conduction velocities were mostly in the range re-

ported in [15]. Furthermore, rhythm features of clinical relevance were observed in the measurements, for example an atrial bigeminy and ectopic beats.

Cases of colliding wavefronts and measurements with an AFocusII spiral catheter could be analyzed with the RBF interpolation. The resulting incidence angles were also in good agreement with the expected directions.

Calculating the CC of the CS activation pattern was a simple but helpful method to determine the propagation direction along the CS. During NSR, CC values were typically between -0.9 and -1.0. For stimulations in the different PVs (segments 1c to 1f), the changes were similar to those observed in the Visible Man simulations. However, no positive values were observed in the clinical data, not even for stimuli in the left PVs. A possible reason is that stimulations may have been performed more at the side of the PV that was closer to the center of the atrium. Generally, the CC is easier to interpret than the slope of the linear fit, because the CC is normalized to a range from -1 to 1. In future studies, it is therefore probably sufficient to calculate the CC only.

Our evaluation of clinical data comprised a considerable number of measurements. The results show that the proposed methods are very promising techniques to efficiently extract patient-specific substrate parameters from intracardiac EGMs. The cosine-fit is based on data from frequently used circular mapping catheters. Therefore, additional requirements (e.g. to use special catheters) and additional examination time are minimized. The RBF interpolation method, in contrast, can be used for different catheter types. However, the method still needs to be systematically evaluated in terms of sensitivity to errors in clinical catheter positions.

The presented methods open up the possibility to systematically study larger patient groups with respect to the atrial activation sequence and conduction velocity. For example, analysis of the wave direction in atypical atrial flutter can quickly give an idea about the underlying arrhythmia pattern and can immediately analyze pattern changes. Thus, it could decrease examination times and reduce treatment costs. Systematic CV measurements after termination of paroxysmal AF could, for example, be compared to recidivism rates and thus help to better understand the mechanisms underlying AF.

Such data is further valuable for the integration into personalized simulation models that could assist the physician in ablation planning for atrial arrhythmias [69].

10.6.3 CV Restitution

Measured local CV values in the LA varied much stronger during pacing (range 47 to 107 cm/s at PCL 300 ms) than during NSR (range 104 to 120 cm/s). This implies that

individual responses to shorter pacing intervals show a high variability in patients suffering from atrial arrhythmias.

For seven out of eight analyzed pacing sequences, *local CV* significantly changed between a PCL of 500 ms on one hand and 300 ms on the other hand. Local CV decreased in six data sets, whereas in one sequence it increased. In the data sets with decreasing CV, the average decrease amounted to $-20 \pm 15\%$ (range -7% to -42%). In one sequence, local CV increased by 53%. For *global CV*, a significant change was observed in seven pacing sequences: six times it decreased and once it increased. For the sequences with decreasing global CV, the average decrease was $-17 \pm 13\%$ (range -2% to -39%).

Previous measurements in the human RA compared CVs at PCLs of 600 and 300 ms [9]. For patients with a history of atrial flutter, the average CV was reduced by 7%, for patients with no such history it was reduced by 5%. Changes in patient 5 in the RA were of comparable magnitude, but changes in the other patients in the LA were considerably higher. It is further interesting to note that in [9], CV changes in atrial flutter patients were statistically significant in three out of four measurement setups, but only in one setup for control patients. In another study in isolated rabbit atrium [152], relative CV changes of up to -40% have been reported between a basic cycle length of 500 ms and early premature beats, which is comparable to the results obtained here for the LA.

Several CV restitution curves observed in this study showed morphological features that have been reported previously in the literature. Regions of supernormal conduction (i.e. increased CV for shorter pacing intervals), for example, have been discussed in [140] and [153]. Triphasic restitution curves have further been documented for the ERP in the ventricles [154, 155]. At a fixed PCL, ERP restitution can also influence the DI and therefore local CV. This could possibly produce similar observations in the CV restitution curve as a function of the inter-beat-interval.

In contrast, changes such as the 53% increase in local CV in patient 1 during CS 3-4 pacing have not been observed yet to the knowledge of the author. As an explanation for such unexpected behaviour, a measurement error was very unlikely due to several reasons. First, the local CV increase was very large. Second, the fit residual was low, and Fig. 10.11 shows that the quality of the fit was good. Furthermore, because the data were recorded and analyzed as continuous signal, any accidental interchange of electrograms (i.e. in reverse order) can be precluded. There is no ready explanation for this phenomenon yet. However, in the global CV in Fig. 10.12(a) at PCL 300 ms, one can recognize an alternans effect: a group of points shows a somewhat increased IBI and reduced global CV, whereas another group has a decreased IBI and increased

global CV. These events appear in alternating order in the original data. Thus, this alternans may have influenced the development of the observed pattern. Generally, such unexpected behaviour shows that studying larger patient groups could gain valuable insights. Such studies might help to give better explanations and could reveal similar or other unexpected phenomena.

In future studies, it would also be interesting to compare electrogram morphologies for different PCLs. For example, the average amplitude and number of deflections might be an indicator for the rate-dependent level of fractionation. Apart from that, the average signal for a certain channel could be computed from all beats within one PCL. It could then be compared to the average signal from the same channel for different PCLs.

Furthermore, a question is if steady-state is already reached during the limited number of approximately 15 stimuli for each PCL. Observations in the ventricles showed that steady-state is typically reached after 2-3 minutes when the PCL is increased from 1000 to 600 ms [156]. As the ERP gradually adapts, CV restitution could be influenced by changes in diastolic interval. On the other hand, ERP measurements have been performed using pacing protocols with a comparable number of stimuli [17]. Furthermore, when looking at a certain PCL in our data, we found rather a statistical fluctuation in CV than, for example, a linear or exponential decrease. Therefore, also due to the comparably small PCL steps present in this work, the results should give a good approximation of the steady-state conditions.

Global CV was derived from the propagation time between pacing and detection. This time can be influenced by the coupling latency, i.e. the delay between stimulus application and start of wave propagation in the cardiac tissue [152]. However, the aim of calculating global CV restitution was to have a rough comparison to the values obtained from the proposed method to measure local CV restitution with a circular mapping catheter. In this context, rate-dependent changes of the latency time should be negligible. It should be mentioned here that an advantage of the local CV measurements is that such latency effects are eliminated.

In cardiac modeling studies, CV restitution often is an important parameter [131]. There, it is most often given as CV over DI. In the data presented here, ERP and DI could not be evaluated. ERP could possibly be determined from intracardiac EGMs by an estimation of action potential duration, which is however especially challenging to measure in the atria [157]. However, the presented method could also be applied to more complex S1-S2 pacing protocols, which are, for example, used to measure the effective refractory period [17]. The CV could additionally be measured with a circular mapping catheter in such studies. The diastolic interval could be estimated for

each PCL from the difference between PCL and ERP. This could enable in-vivo measurements of CV restitution curves over DI. Furthermore, combined measurements of CV and ERP restitution would allow to directly determine wavelength restitution in the human atria in-vivo. This is of special interest, because wavelength is a very important parameter for the maintenance of re-entrant excitations [19, 152, 131, 9]. In contrast, it may also be advantageous to analyze data from incremental pacing as presented here. The reason is that measurements can easily be included into clinical practice. The length of the analyzed data segments was typically around 60 s long, which corresponds to the time required for the measurements. This way, one could study large cohorts of patients with respect to rate-dependent CV changes during routine electrophysiological studies. With this method, it could even be possible to detect pro-arrhythmic substrate during sinus rhythm and thus decrease examination times during catheter ablation of atrial fibrillation.

Results: Comparison of Simulated and Clinical Data

As a first step towards the personalization of atrial models, simulated catheter measurements from patient-individual anatomical models were compared to clinical recordings. To this end, both the simulated and the clinical electrograms (EGMs) were analyzed with the cosine fit in terms of wavefront direction. Where colliding wavefronts were measured, the RBF interpolation method was used for analysis. The applied methods are described in detail in chapter 7.

11.1 Simulation Results

An overview of the simulated and clinical results is given in Table 11.1. The mean deviation in incidence angles was $28 \pm 15^\circ$. The relative error of the calculated conduction velocity (CV) compared to the value used as input parameter for the cellular automaton was $16 \pm 15\%$ on average. The results for the individual patients are discussed in more detail in the following.

Patient 1

In patient 1, the deviations between simulated and clinical incidence angles were smaller than average and ranged between 19° and 24° . Figure 11.1 shows the simulated wavefront during stimulation from CS 7-8. The deviation compared to the clinically measured angle was less than half an electrode spacing. The simulated electrograms show similar morphological features as the clinical signals.

Patient 2

In the anterior simulation for patient 2, the deviations between simulated and clinical incidence angles were 45° and 36° and thus rather large. However, the offsets between NSR and CS 3-4 stimulation are quite similar in both cases (77° vs. 68°). This implies that the simulated catheter may have been rotated with respect to the real position.

Table 11.1. Comparison between simulated values and clinical measurements.

Patient	Seg	Location	Stim Site	Incid. Dir. $\varphi_0(^{\circ})$			CV (cm/s)		
				Clinical	Sim	$\Delta\varphi_0$	Clinical	Sim	Rel Err
1	1b	Roof	NSR	51	32	19	110	108	2%
	1a		CS 3-4	211	235	24	110	119	8%
	1b		CS 7-8	268	248	20	110	106	4%
2	2a	Anterior	NSR	259	304	45	56	58	4%
	2b		CS 3-4	336	12 [†]	36	56	61 [†]	9%
	2c	Posterior	NSR	310	1	51	56	51	9%
	2c		CS 3-4	175	174	1	68	58	15%
3	3a	Anterior	NSR	230	221	9	87	76	13%
	3b		CS 3-4 (coll)	298 [†]	340	42	90	136	51%
	3b		CS 7-8 (coll)	224 [†]	284	60	90	112	24%
	3c	Roof	NSR	227	246	19	120	92	23%
	3d		CS 3-4	29	38	9	97	60	38%
	3d		CS 7-8	18	48	30	97	99	2%
4	4a	Anterior	NSR	218	192	26	68	56	18%
	4a		CS 3-4	351	19	28	68	61	10%
	4b		CS 7-8	345	303	42	68	100	47%
	4e	Roof	NSR	271	290	19	96	80	17%
	4c		CS 3-4	91	107	16	96	93	3%
	4e		CS 7-8	83	121	38	96	83	14%

[†] Derived using RBF Interpolation

Furthermore, it must be noted that in the simulation of CS 3-4 stimulation, two wave fronts collided in the catheter area. Therefore, RBF analysis was applied to separate the wavefronts, and the angle that was closer to the clinical measurement was used for comparison.

The posterior simulation in patient 2 showed a very good match for CS 3-4 stimulation (difference 1°), but a large deviation of 51° for NSR. In Figure 11.2 it can be seen that in the NSR simulation, a wavefront passing the LA roof was the first front to arrive at the catheter. However, a second front approached the catheter from the direction of the posterior septal region with some delay. The incidence direction of the second front matched quite well the clinical incidence direction. So it is possible that for adapted RA to LA conduction properties in the simulation, the front from the septal region would be the first one to pass the catheter. This would then result in a better match of simulation and clinical measurement.

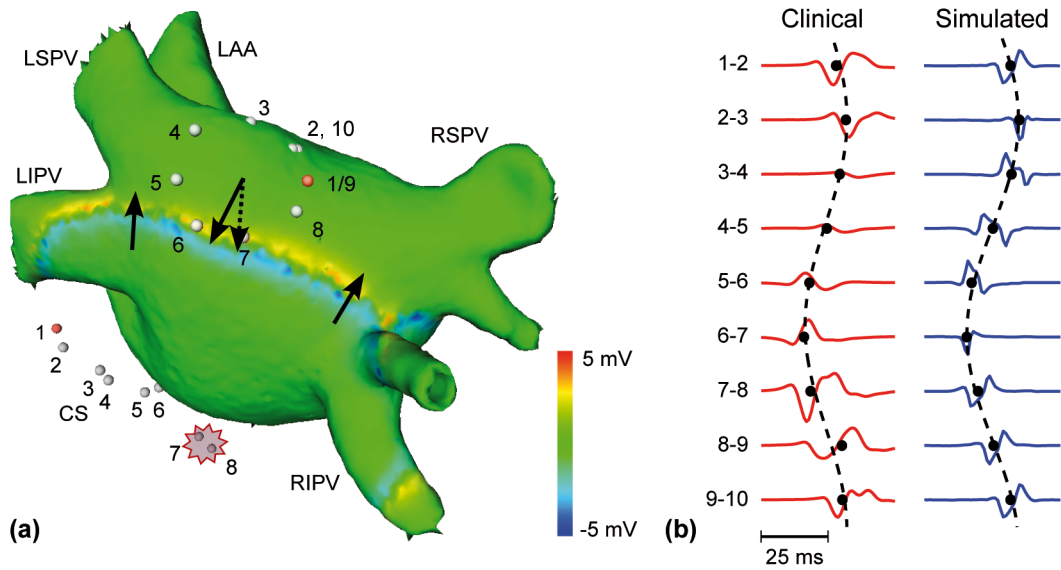


Fig. 11.1. Simulation for patient 1, stimulus in coronary sinus electrodes CS 7-8. (a) Excitation front (upward arrows) on the LA roof, the extracellular potential is shown. The catheter electrodes are located on the endocardium, but shown here on the epicardium for better visibility. Detected incidence directions are marked at the catheter center (solid arrow: simulated direction, dotted arrow: clinical measurement). Both directions point approximately towards the stimulus center in the CS 7-8 electrodes. (b) Clinical and simulated electrograms (EGMs). The activation pattern and resulting cosine-fit are very similar. Also EGM morphology is comparable. Adapted from [158].

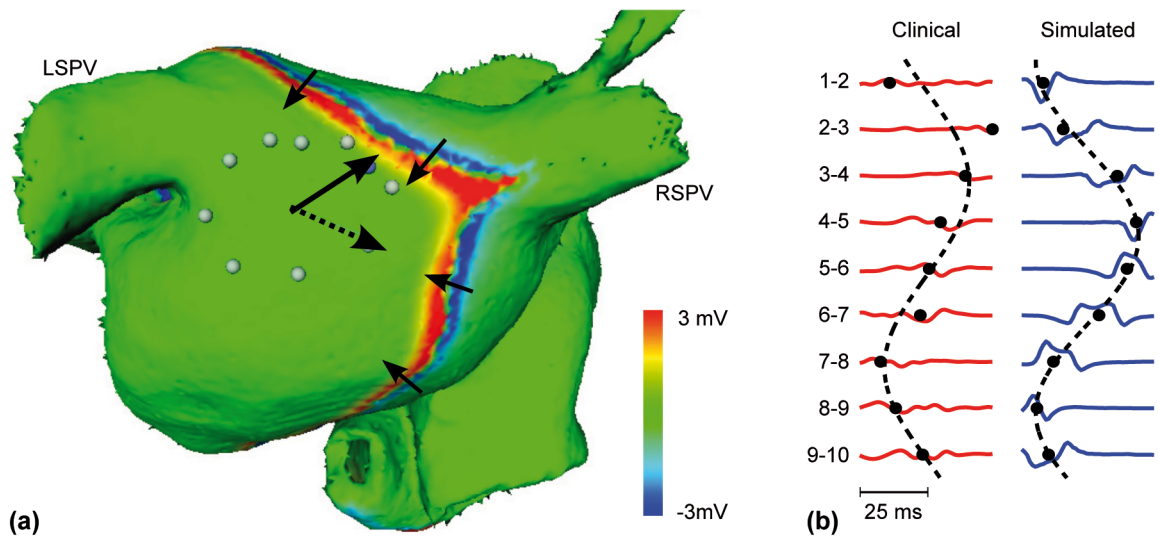


Fig. 11.2. Simulation for patient 2 during sinus rhythm. (a). Excitation front on the posterior LA wall (extracellular front). The catheter electrodes are located on the endocardium, but shown here on the epicardium for better visibility. Detected incidence directions are marked at the catheter center. The simulated direction (solid arrow) pointed towards the LA roof, while the clinical measurement (dotted arrow) pointed towards the posterior septal region. (b) Clinical and simulated electrograms (EGMs). The difference in incidence direction is also manifested in the activation pattern. (Clinical signals scaled by factor 4).

Patient 3

In patient 3, the anterior NSR simulation corresponded well to the clinical measurements, the deviation was 9° . During stimulation, two wavefronts collided under the

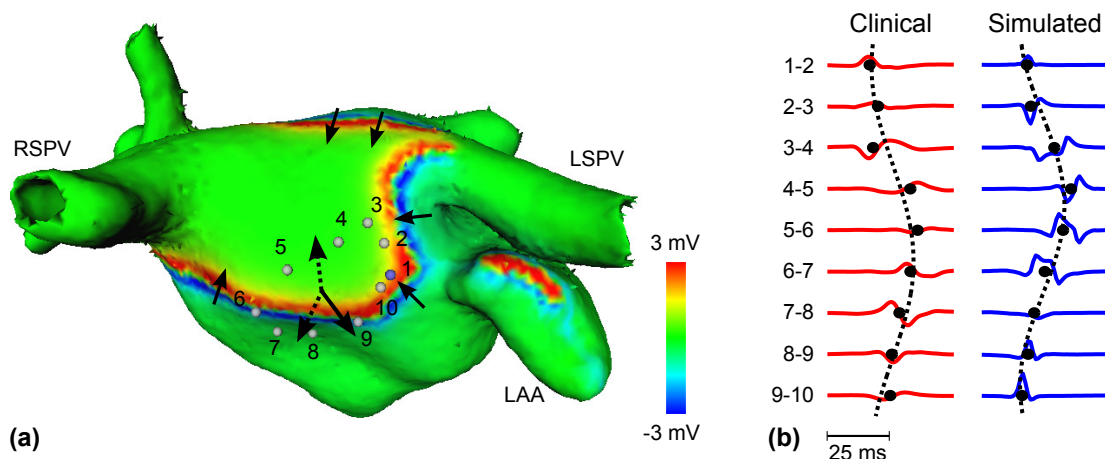


Fig. 11.3. Simulation for patient 3, stimulus in coronary sinus electrodes CS 3-4. (a) Excitation fronts (small arrows) on the anterior LA wall, the extracellular potential is shown. The catheter electrodes are located on the endocardium, but shown here on the epicardium for better visibility. Detected incidence directions are marked at the catheter center (solid arrow: simulated direction, dotted arrows: clinical results from RBF interpolation). The simulated direction is rotated counter-clockwise due to the wavefront components passing the LAA. A second front is approaching over the LA roof, its direction is similar to the second clinical incidence direction. (b) Clinical and simulated electrograms (EGMs).

catheter as demonstrated in Figure 10.8 on page 109. The simulation of the CS 3-4 pacing is shown in Figure 11.3. The deviation between simulated incidence direction and clinical measurements was rather large with 42° . In the simulation, there was no collision of wavefronts from opposite directions. However, there was a wave front from the left lateral side that rotated the determined incidence angle towards higher angles. A second wave front was approaching the catheter on the LA roof with an incidence direction similar to that of the second clinical direction. However, it arrived too late in the simulation. Errors in estimated CV were rather high. This may be due to the squeezed catheter geometry and the contribution of several wave fronts on the activation of the catheter. However, the influence of the other fronts does not seem to be high enough to use the RBF interpolation instead of the cosine fit.

Simulations in patient 3 on the LA roof showed moderate angle deviations between 9° and 30° . For these simulations, the original mapped catheter positions were rotated to be parallel to the surface. Obviously, no significant angle errors were introduced by this correction.

Patient 4

For the anterior simulations in patient 4, directional errors were above average (between 26° and 42°). Here, the mitral valve plays an important role as geometrical obstacle. The mitral valve splits wave fronts stimulated in the CS into an inferior and a superior part as can be seen in Figure 11.4 for the CS 3-4 stimulation. In this

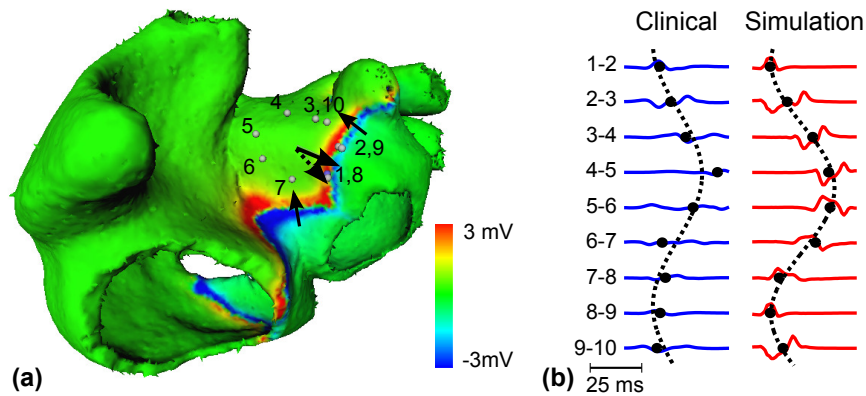


Fig. 11.4. Simulation for patient 4, stimulus in coronary sinus electrodes CS 3-4. (a) Excitation fronts (small arrows) on the anterior LA wall, the extracellular potential is shown. The catheter electrodes are located on the endocardium, but shown here on the epicardium for better visibility. Detected incidence directions are marked at the catheter center (solid arrow: simulated direction, dotted arrows: clinical results from RBF interpolation). The wave front passing the mitral valve superiorly mainly determines the incidence direction. (b) Clinical and simulated electrograms (EGMs).

case, mainly the front passing superior over the mitral valve activates the catheter region. In the CS 7-8 simulation, only the inferior part activates the circular mapping catheter, which leads to an incidence direction pointing downwards. In the clinical measurement, in contrast, the incidence direction for the CS 7-8 stimulation is similar to those from CS 3-4 stimulation (see Figure 10.9 on page 111). This leads to a high directional deviation of 42° between simulation and measurement for the CS 7-8 stimulation.

In the simulations in patient 4 with a catheter on the LA roof, the deviations between simulation and clinical measurements are moderate for NSR and CS 3-4 pacing (19° and 16°), but increased for CS 7-8 pacing (38°).

11.2 Discussion

A workflow was demonstrated to create personalized anatomical simulation models. It includes clinical catheter measurement positions and stimuli sites, simulated cardiac excitation and the resulting electrograms, and comparisons of the simulation to the clinical measurements based on quantitative electrogram analysis.

The average directional error was 28° and was thus smaller than the typical inter-electrode spacing (which would be around 36° for a 10-electrode catheter adjusted to cover a full circle). This directional error is a measure of how good the simulations agree with measured excitation propagation. For cases with high deviations it might be necessary to tune further model parameters. For example, conduction between RA and LA plays an important role [12, 13] and influences the activation sequence

of the LA. Furthermore, fast conducting pathways and fiber orientation can impact on excitation propagation [159, 160, 161]. Such properties could be included into the personalized model [99, 162] to test if this results in significant changes of excitation conduction and possibly even better correspondence between simulation and measurement.

The average relative error in CV estimation from the simulated EGMs was 16%. It only gives an idea how well a known reference CV used as simulation input parameter can be reproduced by the EGM analysis. A possible cause for deviations is that the cosine-fit method assumes that the catheter shape is perfectly circular. However, the mapped catheter positions often show a squeezed geometry, i.e. they have a rather elliptical shape. Although it has not been systematically evaluated, sporadic comparisons of the mapped positions and the positions in the fluoroscopic x-ray suggested that the real shape of the catheter was indeed rather circular than elliptic. The squeezing probably results from measurement limitations in the mapping systems, such as field inhomogeneities. For analysis of real clinical measurements, the cosine-fit analysis is therefore more stable. For the simulation in the patient-specific geometry, however, the mapped elliptic catheter shapes were inserted into the model. Now, the in-silico measurements were in fact performed with elliptic catheters. Therefore, the cosine-fit is likely to over- or underestimate CV, depending on the incidence direction. In future studies, catheter positions could therefore be corrected before inserting them into the model.

A big advantage of analyzing single wavefronts is that the required clinical measurements can be performed very quickly, even for different stimulation sites. This approach is therefore very promising for the adaptation and validation of personalized models during routine clinical workflows.

Conclusion

In this thesis, important aspects for personalizing atrial simulations have been investigated. First, a minimal electrophysiological cell model has been implemented. It was originally supplied only with parameter sets to reproduce ventricular excitation properties. In the course of this work, the model parameters have been adapted to reproduce atrial properties as given by the Courtemanche-Ramirez-Nattel model. Besides the physiological case, a parameter set for atrial remodeling during chronic AF has been created. This will allow for studying arrhythmic behaviour with this model in future. For the atrial simulations in the remaining part of this work, the cellular automaton was used, because no advanced excitation properties such as, for example, conduction velocity (CV) restitution were considered in these simulations. However, the adaptation framework allows for further adaptations of the minimal model with respect to patient-specific measurements. An important advantage compared to detailed ionic models is that the minimal model behavior can be adjusted on a phenomenological basis, using a very limited number of parameters only. As an example, the CV restitution curve of the model can in future be adapted to measured CV restitution curves as demonstrated in the analysis section of this work. If no patient-specific measurements for the effective refractory periods are available, literature values could be used as a first guess. This allows for including patient-specific excitation properties in the simulations.

Second, the influence of tissue conductivities on simulated electrocardiograms (ECGs) and body surface potential maps (BSPMs) has been evaluated. Although the question which torso inhomogeneities are more important than others has been addressed before, the current evaluation gives new insights. On one hand, to the knowledge of the author it is the first study to be based on simulated transmembrane voltage distributions. This is the relevant case for patient-specific computer simulations. On the other hand, it was investigated how the uncertainty in literature values for different conductivities influences the ECG. With the resulting ranking, patient-tailored torso

geometries can be simplified by including only the necessary level of detail. Apart from the description of important tissues and organs, an efficient prediction method for changes in BSPM due to conductivity variations was developed in this work. It is based on principal component analysis and can predict signal changes over a wide range of conductivities from few sample simulations. This is of great advantage in the personalization of torso models and the simulation of patient-individual ECGs.

A significant part of this thesis covered the quantitative analysis of intracardiac catheter measurements taken during electrophysiological studies. A cosine-fit method has been developed that estimates the incidence direction and conduction velocity of a single wavefront passing a circular mapping catheter. It allows to study excitation propagation on a single-beat level. Thus, it is for example possible to analyze the incidence direction of ectopic beats. Furthermore, conduction velocities can be determined as input parameters for personalized models. A considerable number of clinical measurements has been successfully analyzed in this thesis using the cosine-fit. An alternative method based on radial basis function interpolation was adapted and extended. It allows to analyze electrograms measured with different catheter shapes and more complex activation patterns such as colliding wavefronts. In a simulated test setup, it showed a comparable result quality as the cosine-fit. For clinical data, excitation measured with a spiral catheter and two colliding wavefronts measured with a circular catheter could be reconstructed. However, the method still needs to be systematically evaluated in terms of sensitivity to errors in clinical catheter positions. A third component analyzed propagation direction in the coronary sinus, which is a helpful supplemental analysis, e.g., for detecting ectopic beats. In future, the challenge will be to combine the strengths of these three methods for even more reliable and flexible analysis techniques. They could then also be implemented into electroanatomical mapping systems to give a quick quantitative feedback to the physician based on the measured electrograms and provide data of high diagnostic value.

The cosine-fit analysis has further been used to measure CV restitution curves in individual patients. Such data were very scarce so far, but are of great interest both for clinical considerations and atrial modeling. It was shown in this work that atrial CV was rate-dependent. Further studies with more patients can now be performed to confirm these findings. They may provide valuable insights into the underlying mechanisms of atrial arrhythmias and allow characterizing arrhythmogenic substrate during sinus rhythm. This way, regions of abnormal CV restitution could be identified as possible target regions for ablation. The cosine-fit and the coronary sinus analysis are also good examples of analysis techniques that were developed and validated *in silico*, i.e. based on simulations of the catheter measurement. The resulting

analysis methods, however, can be applied directly to clinical data without incorporating further modeling. This demonstrates the possibilities of cardiac modeling for the development of new quantitative analysis techniques.

Finally, patient specific simulations were performed. The simulation anatomy was tailored by using a segmentation workflow for CTs with contrast enhancement in the left atrium and the pulmonary veins. As an electrophysiological parameter, CV was determined from intracardiac recordings with the cosine-fit method. Then, the clinical excitation sequence was reproduced by stimulating the model at the sinus node or the catheter electrodes used in the clinical pacing protocol. For most cases, incidence directions showed a good correspondence between simulation and measurement. In some patients, larger angle deviations possibly resulted from delays between concurring wavefronts. Such comparisons are a valuable basis for further personalization. For example, they allow for investigating if fiber orientation in the model reduces the remaining directional errors. This shows that analysis and simulation of intracardiac electrograms can be used as an interface between clinical measurements and simulation models. On one hand electrophysiological parameters can be determined from frequently used clinical measurements, on the other hand, simulation results can be quantitatively compared to measured data.

In summary, it was shown that important limitations in the personalization of atrial models can be overcome with the presented methods. This opens up the possibility for studying atrial model personalization in larger groups of patients. Furthermore, the analysis methods developed for intracardiac electrograms can be directly applied to clinical measurements without additional modeling steps. These results will hopefully lead to a better understanding of the underlying mechanisms and an improvement of the treatment. This way, personalized models could reduce examination times, improve success rates and significantly reduce both the overall treatment costs and — most important — the patients' burden.

References

1. V. Fuster, L. Ryden, D. Cannom, H. Crijns, A. Curtis, K. Ellenbogen, J. Halperin, J.-Y. Le Heuzey, G. Kay, J. Lowe, S. Olsson, E. Prystowsky, J. Tamargo, S. Wann, S. Smith, A. Jacobs, C. Adams, J. Anderson, E. Antman, S. Hunt, R. Nishimura, J. Ornato, R. Page, B. Riegel, S. Priori, J.-J. Blanc, A. Budaj, A. Camm, V. Dean, J. Deckers, C. Despres, K. Dickstein, J. Lekakis, K. McGregor, M. Metra, J. Morais, A. Osterspey, J. Zamorano, and Heart Rhythm Society, “ACC/AHA/ESC 2006 Guidelines for the Management of Patients with Atrial Fibrillation: a report of the American College of Cardiology/American Heart Association Task Force on Practice Guidelines and the European Society of Cardiology Committee for Practice Guidelines (Writing Committee to Revise the 2001 Guidelines for the Management of Patients With Atrial Fibrillation): developed in collaboration with the European Heart Rhythm Association and the Heart Rhythm Society,” 2006.
2. F. H. Martini, *Fundamentals of Anatomy & Physiology*. Prentice Hall, Inc. Upper Saddle River, NJ: Pearson, Benjamin-Cummings Publishing Company, 2006.
3. K. Saladin, *Anatomy and Physiology : The Unity of Form and Function*. McGraw-Hill, 2003.
4. M. Burdumy, “Personalized Simulation and Analysis of Intracardiac Electrograms of the Left Atrium,” Diploma thesis, 2010.
5. G. Seemann, *Modeling of electrophysiology and tension development in the human heart*. PhD thesis, Universitätsverlag Karlsruhe, 2005.
6. R. Schmidt, *Physiologie kompakt*, ch. Erregungsphysiologie des Herzens, pp. 197–204. Berlin, Heidelberg, New York: Springer, 1999.
7. B. Hall, V. Jeevanantham, R. Simon, J. Filippone, G. Vorobiof, and J. Daubert, “Variation in left atrial transmural wall thickness at sites commonly targeted for ablation of atrial fibrillation,” *J Interv Card Electrophysiol*, vol. 17, pp. 127–132, 2006.
8. C. Schmitt, I. Deisenhofer, and B. Zrenner, eds., *Catheter Ablation of Cardiac Arrhythmias: A Practical Approach*. Springer, 2006.
9. G. K. Feld, M. Mollerus, U. Birgersdotter-Green, O. Fujimura, T. D. Bahnson, K. Boyce, and M. Rahme, “Conduction velocity in the tricuspid valve-inferior vena cava isthmus is slower in patients with type I atrial flutter compared to those without a history of atrial flutter,” *J Cardiovasc Electrophysiol*, vol. 8, pp. 1338–1348, 1997.
10. E. Marom, J. Herndon, Y. Kim, and H. McAdams, “Variations in pulmonary venous drainage to the left atrium: implications for radiofrequency ablation,” *Radiology*, vol. 230, pp. 824–829, 2004.
11. H. Nathan and M. Eliakim, “The junction between the left atrium and the pulmonary veins. An anatomic study of human hearts,” *Circulation*, vol. 34, pp. 412–422, 1966.

12. S. Ho and D. Sanchez-Quintana, "The importance of atrial structure and fibers," *Clin Anat*, vol. 22, pp. 52–63, 2009.
13. F. Roithinger, J. Cheng, A. SippensGroenewegen, R. Lee, L. Saxon, M. Scheinman, and M. Lesh, "Use of electroanatomic mapping to delineate transseptal atrial conduction in humans," *Circulation*, vol. 100, pp. 1791–1797, 1999.
14. M. Chauvin, D. Shah, M. Haissaguerre, L. Marcellin, and C. Brechenmacher, "The Anatomic Basis of Connections Between the Coronary Sinus Musculature and the Left Atrium in Humans," *Circulation*, vol. 101, pp. 647–652, 2000.
15. A. Hansson, M. Holm, P. Blomstrom, R. Johansson, C. Luhrs, J. Brandt, and S. Olsson, "Right atrial free wall conduction velocity and degree of anisotropy in patients with stable sinus rhythm studied during open heart surgery," *Eur Heart J*, vol. 19, pp. 293–300, 1998.
16. A. Hassankhani, B. Yao, and G. Feld, "Conduction velocity around the tricuspid valve annulus during type I atrial flutter: defining the location of areas of slow conduction by three-dimensional electroanatomical mapping," *J Interv Card Electrophysiol*, vol. 8, pp. 121–127, 2003.
17. T. Rostock, D. Steven, B. Lutomsky, H. Servatius, I. Drewitz, H. Klemm, K. Mullerleile, R. Ventura, T. Meinertz, and S. Willems, "Atrial fibrillation begets atrial fibrillation in the pulmonary veins: on the impact of atrial fibrillation on the electrophysiological properties of the pulmonary veins in humans," *J Am Coll Cardiol*, vol. 51, pp. 2153–2160, 2008.
18. C. Schneider, *Das EPU-Labor*. Steinkopff, 2005.
19. M. Allesie, F. Bonke, and F. Schopman, "Circus movement in rabbit atrial muscle as a mechanism of tachycardia. III. The "leading circle" concept: a new model of circus movement in cardiac tissue without the involvement of an anatomical obstacle," *Circ Res*, vol. 41, pp. 9–18, 1977.
20. M. Haissaguerre, P. Jais, D. C. Shah, A. Takahashi, M. Hocini, G. Quiniou, S. Garrigue, A. Le Mouroux, P. Le Metayer, and J. Clementy, "Spontaneous initiation of atrial fibrillation by ectopic beats originating in the pulmonary veins," *N Engl J Med*, vol. 339, pp. 659–666, 1998.
21. M. D. O'Neill, P. Jais, Y. Takahashi, A. Jonsson, F. Sacher, M. Hocini, P. Sanders, T. Rostock, M. Rotter, A. Pernet, J. Clementy, and M. Haissaguerre, "The stepwise ablation approach for chronic atrial fibrillation—evidence for a cumulative effect," *J Interv Card Electrophysiol*, vol. 16, pp. 153–167, 2006.
22. S. Nattel, "New ideas about atrial fibrillation 50 years on," *Nature*, vol. 415, pp. 219–226, 2002.
23. M. Wijffels, C. Kirchhof, R. Dorland, and M. Allesie, "Atrial Fibrillation Begets Atrial Fibrillation," *Circulation*, vol. 92, pp. 1954–1968, 1995.
24. M. Allesie, J. Ausma, and U. Schotten, "Electrical, contractile and structural remodeling during atrial fibrillation," *Cardiovasc Res*, vol. 54, pp. 230–246, 2002.
25. M. Courtemanche, R. Ramirez, and S. Nattel, "Ionic targets for drug therapy and atrial fibrillation-induced electrical remodeling: insights from a mathematical model," *Cardiovasc Res*, vol. 42, pp. 477–489, 1999.
26. H. van der Velden, J. Ausma, M. Rook, A. Hellemons, T. van Veen, M. Allesie, and H. Jongsma, "Gap junctional remodeling in relation to stabilization of atrial fibrillation in the goat," *Cardiovasc Res*, vol. 46, pp. 476–486, 2000.
27. L. Polontchouk, J. Haefliger, B. Ebelt, T. Schaefer, D. Stuhlmann, U. Mehlhorn, F. Kuhn-Regnier, E. De Vivie, and S. Dhein, "Effects of chronic atrial fibrillation on gap junction distribution in human and rat atria," *J Am Coll Cardiol*, vol. 38, pp. 883–891, 2001.
28. M. Wilhelm, W. Kirste, S. Kuly, K. Amann, W. Neuhuber, M. Weyand, W. Daniel, and C. Garlich, "Atrial distribution of connexin 40 and 43 in patients with intermittent, persistent, and postoperative

- atrial fibrillation,” *Heart Lung Circ*, vol. 15, pp. 30–37, 2006.
29. M. Bauer, “Simulation von chaotischen Erregungsmustern bei Vorhofflimmern mit einem minimalen Zellmodell,” Bachelor’s thesis, 2010.
 30. Y. Takahashi, M. Hocini, M. D. O’Neill, P. Sanders, M. Rotter, T. Rostock, A. Jonsson, F. Sacher, J. Clementy, P. Jais, and M. Haissaguerre, “Sites of focal atrial activity characterized by endocardial mapping during atrial fibrillation,” *J Am Coll Cardiol*, vol. 47, pp. 2005–2012, 2006.
 31. T. Rostock, M. Rotter, P. Sanders, Y. Takahashi, P. Jais, M. Hocini, L.-F. Hsu, F. Sacher, J. Clementy, and M. Haissaguerre, “High-density activation mapping of fractionated electrograms in the atria of patients with paroxysmal atrial fibrillation,” *Heart Rhythm*, vol. 3, pp. 27–34, 2006.
 32. S. A. Ben-Haim, D. Osadchy, I. Schuster, L. Gepstein, G. Hayam, and M. E. Josephson, “Nonfluoroscopic, in vivo navigation and mapping technology,” *Nature Medicine*, vol. 2, pp. 1393–1395, 1996.
 33. Y. Jiang, D. Farina, M. Bar-Tal, and O. Dössel, “An impedance based catheter positioning system for cardiac mapping and navigation,” *IEEE Trans Biomed Eng*, vol. 56, pp. 1963–1970, 2009.
 34. F. H. Wittkamp, E. F. Wever, R. Derksen, A. A. Wilde, H. Ramanna, R. N. Hauer, and E. O. Robles de Medina, “LocaLisa: new technique for real-time 3-dimensional localization of regular intracardiac electrodes,” *Circulation*, vol. 99, pp. 1312–1317, 1999.
 35. H. L. Estner, I. Deisenhofer, A. Luik, G. Ndrepepa, C. von Bary, B. Zrenner, and C. Schmitt, “Electrical isolation of pulmonary veins in patients with atrial fibrillation: reduction of fluoroscopy exposure and procedure duration by the use of a non-fluoroscopic navigation system (NavX),” *Europace*, vol. 8, pp. 583–587, 2006.
 36. M. Borggrefe, T. Budde, A. Podczeck, and G. Breithardt, “High frequency alternating current ablation of an accessory pathway in humans,” *J Am Coll Cardiol*, vol. 10, pp. 576–582, 1987.
 37. P. C. Gillette, M. M. Swindle, R. P. Thompson, and C. L. Case, “Transvenous cryoablation of the bundle of His,” *Pacing Clin Electrophysiol*, vol. 14, pp. 504–510, 1991.
 38. F. H. Wittkamp, T. A. Simmers, R. N. Hauer, and E. O. Robles de Medina, “Myocardial temperature response during radiofrequency catheter ablation,” *Pacing Clin Electrophysiol*, vol. 18, pp. 307–317, 1995.
 39. A. Luik, M. Merkel, D. Hoeren, T. Riexinger, M. Kieser, and C. Schmitt, “Rationale and design of the FreezeAF trial: a randomized controlled noninferiority trial comparing isolation of the pulmonary veins with the cryoballoon catheter versus open irrigated radiofrequency ablation in patients with paroxysmal atrial fibrillation,” *Am Heart J*, vol. 159, pp. 555–560.e1, 2010.
 40. M. P. Nguyen, C. Schilling, and O. Dössel, “A new approach for automated location of active segments in intracardiac electrograms,” in *IFMBE Proceedings World Congress on Medical Physics and Biomedical Engineering*, vol. 25/4, pp. 763–766, 2009.
 41. A. Luik, M. Merkel, T. Riexinger, R. Wondraschek, and C. Schmitt, “Persistent atrial fibrillation converts to common type atrial flutter during CFAE ablation,” *Pacing Clin Electrophysiol*, vol. 33, pp. 304–308, 2010.
 42. M. Ackerman, “Viewpoint: The Visible Human Project,” *J Biocommun*, vol. 18, p. 14, 1991.
 43. “Visible human project, national library of medicine, Bethesda, USA.”
 44. C. Lorenz and J. von Berg, “A comprehensive shape model of the heart,” *Med Image Anal*, vol. 10, pp. 657–670, 2006.
 45. G. Seemann, F. Sachse, M. Karl, D. Weiss, V. Heuveline, and O. Dössel, “Framework for modular, flexible and efficient solving the cardiac bidomain equation using PETSc,” *Progr Industr Math*, vol. 15, pp. 363–369, 2010.

46. A. Hodgkin and A. Huxley, "A quantitative description of membrane current and its application to conduction and excitation in nerve," *J Physiol*, vol. 177, pp. 500–544, 1952.
47. M. Courtemanche, R. J. Ramirez, and S. Nattel, "Ionic mechanisms underlying human atrial action potential properties: Insights from a mathematical model," *Am J Physiol*, vol. 275, pp. H301–H321, 1998.
48. A. van Oosterom and V. Jacquemet, "Ensuring stability in models of atrial kinetics," in *Proc Computers in Cardiology*, vol. 2009, pp. 69–72, 2009.
49. G. Seemann, P. Carrillo Bustamante, S. Ponto, M. Wilhelms, E. P. Scholz, and O. Dössel, "Atrial Fibrillation-based Electrical Remodeling in a Computer Model of the Human Atrium," in *Proc Computing in Cardiology*, vol. 37, 2010.
50. A. Bueno-Orovio, E. Cherry, and F. Fenton, "Minimal model for human ventricular action potentials in tissue," *Journal of Theoretical Biology*, vol. 253, pp. 544–560, 2008.
51. F. Fenton and A. Karma, "Vortex dynamics in three-dimensional continuous myocardium with fiber rotation: filament instability and fibrillation," *Chaos*, vol. 8, pp. 20–27, 1998.
52. F. Gasperini, C. Lamberti, and J. M. Ferrero, "Adaptation of an action potential minimal model to acute ischemia," in *Proc Computers in Cardiology*, pp. 73–76, 2009.
53. C. S. Henriquez, "Simulating the electrical behavior of cardiac tissue using the bidomain model," *Crit Rev Biomed Eng*, vol. 21, pp. 1–77, 1993.
54. A. J. Pullan, M. L. Buist, and L. K. Cheng, *Mathematically Modelling the Electrical Activity of the Heart: From Cell to Body Surface and Back Again*. Singapore: World Scientific, 2005.
55. C. D. Werner, F. B. Sachse, and O. Dössel, "Electrical Excitation Propagation in the Human Heart," *Int J Bioelectromagn*, vol. 2, 2000.
56. O. Skipa, *Linear inverse problem of electrocardiography: epicardial potentials and transmembrane voltages*. PhD thesis, 2004.
57. K. R. Foster and H. P. Schwan, "Dielectric properties of Tissues and Biological materials: A critical review," *Crit Rev Biomed Eng*, vol. 17, pp. 25–104, 1989.
58. S. Gabriel, R. W. Lau, and C. Gabriel, "The dielectric properties of biological tissues: II. Measurements in the frequency range 10 Hz to 20 GHz," *Phys Med Biol*, vol. 41, pp. 2251–2269, 1996.
59. T. J. C. Faes, H. A. van der Meij, J. C. de Munck, and R. M. Heethaar, "The electric resistivity of human tissues (100 Hz-10 MHz) a meta-analysis of review studies," *Physiol Meas*, vol. 20, p. 1, 1999.
60. S. Gabriel, R. W. Lau, and C. Gabriel, "The dielectric properties of biological tissues: III. Parametric models for the dielectric spectrum of tissues," *Phys Med Biol*, vol. 41, pp. 2271–2293, 1996.
61. F. A. Duck, *Physical properties of tissue: A comprehensive reference book*. Academic Press, London San Diego, 1990.
62. H. C. Burger and R. van Dongen, "Specific electric resistance of body tissues," *Phys Med Biol*, vol. 5, pp. 431–447, 1961.
63. L. A. Geddes and L. E. Baker, "The specific resistance of biological material-A compendium of data for the biomedical engineer and physiologist," *Med Biol Eng*, vol. 5, pp. 271–293, 1967.
64. E. Zheng, S. Shao, and J. G. Webster, "Impedance of skeletal muscle from 1 Hz to 1 MHz," *IEEE Trans Biomed Eng*, vol. BME-31, pp. 477–481, 1984.
65. Y. Rudy, R. Plonsey, and J. Liebman, "The effects of variations in conductivity and geometrical parameters on the electrocardiogram, using an eccentric spheres model," *Circ Res*, vol. 44, pp. 104–111, 1979.
66. A. van Oosterom, R. W. de Boer, and R. T. van Dam, "Intramural resistivity of cardiac tissue," *Med Biol Eng Comput*, vol. 17, pp. 337–343, 1979.

67. C. P. Bradley, A. J. Pullan, and P. J. Hunter, "Effects of material properties and geometry on electrocardiographic forward simulations," *Annals of Biomedical Engineering*, vol. 28, pp. 721–741, 2000.
68. R. N. Klepfer, C. R. Johnson, and R. S. MacLeod, "The Effects of Inhomogeneities and Anisotropies on Electrocardiographic Fields: A 3-D Finite-Element Study," *IEEE Trans Biomed Eng*, vol. 44, pp. 706–719, 1997.
69. V. Jacquemet, L. Kappenberger, and C. Henriquez, "Modeling Atrial Arrhythmias: Impact on Clinical Diagnosis and Therapies," *IEEE Rev Biomed Eng*, vol. 1, 2008.
70. O. Blanc, N. Virag, J. Vesin, and L. Kappenberger, "A computer model of human atria with reasonable computation load and realistic anatomical properties," *IEEE Trans Biomed Eng*, vol. 48, pp. 1229–1237, 2001.
71. E. J. Vigmond, R. Ruckdeschel, and N. Trayanova, "Reentry in a morphologically realistic atrial model," *J Cardiovasc Electrophysiol*, vol. 12, pp. 1046–1054, 2001.
72. N. Virag, V. Jacquemet, C. S. Henriquez, S. Zozor, O. Blanc, J. M. Vesin, E. Pruvot, and L. Kappenberger, "Study of atrial arrhythmias in a computer model based on magnetic resonance images of human atria," *Chaos*, vol. 12, pp. 754–763, 2002.
73. P. M. van Dam and A. van Oosterom, "Atrial excitation assuming uniform propagation," *J Cardiovasc Electrophysiol*, vol. 14, pp. S166–71, 2003.
74. D. M. Harrild and C. S. Henriquez, "A Computer Model of Normal Conduction in the Human Atria," *Circ Res*, vol. 87, p. 25, 2000.
75. A. Nygren, C. Fiset, L. Firek, J. Clark, D. Lindblad, R. Clark, and W. Giles, "Mathematical model of an adult human atrial cell: the role of K⁺ currents in repolarization," *Circ Res*, vol. 82, pp. 63–81, 1998.
76. G. Seemann, C. Höper, F. Sachse, O. Dössel, A. Holden, and H. Zhang, "Heterogeneous three-dimensional anatomical and electrophysiological model of human atria," *Phil Trans Roy Soc A*, vol. 364, pp. 1465–1481, 2006.
77. M. Reumann, J. Bohnert, G. Seemann, B. Osswald, and O. Dössel, "Preventive ablation strategies in a biophysical model of atrial fibrillation based on realistic anatomical data," *IEEE Trans Biomed Eng*, vol. 55, pp. 399–406, 2008.
78. V. Jacquemet and C. Henriquez, "Genesis of complex fractionated atrial electrograms in zones of slow conduction: a computer model of microfibrosis," *Heart Rhythm*, vol. 6, pp. 803–810, 2009.
79. P. Kojodjojo, P. Kanagaratnam, V. Markides, D. Davies, and N. Peters, "Age-related changes in human left and right atrial conduction," *J Cardiovasc Electrophysiol*, vol. 17, pp. 120–127, 2006.
80. A. Sawa, A. Shimizu, T. Ueyama, Y. Yoshiga, S. Suzuki, N. Sugi, M. Oono, T. Oomiya, and M. Matsuzaki, "Activation patterns and conduction velocity in posterolateral right atrium during typical atrial flutter using an electroanatomic mapping system," *Circ J*, vol. 72, pp. 384–391, 2008.
81. T. N. Fitzgerald, D. H. Brooks, and J. K. Triedman, "Identification of cardiac rhythm features by mathematical analysis of vector fields," *IEEE Trans Biomed Eng*, vol. 52, pp. 19–29, 2005.
82. P. V. Bayly, B. H. KenKnight, J. M. Rogers, R. E. Hillsley, R. E. Ideker, and W. M. Smith, "Estimation of conduction velocity vector fields from epicardial mapping data," *IEEE Trans Biomed Eng*, vol. 45, pp. 563–571, 1998.
83. A. R. Barnette, P. V. Bayly, S. Zhang, G. P. Walcott, R. E. Ideker, and W. M. Smith, "Estimation of 3-D conduction velocity vector fields from cardiac mapping data," *IEEE Trans Biomed Eng*, vol. 47, pp. 1027–1035, 2000.
84. M. Masè, M. Del Greco, M. Marini, and F. Ravelli, "Velocity Field Analysis of Activation Maps in Atrial Fibrillation - A Simulation Study," in *IFMBE Proceedings World Congress on Medical Physics*

- and Biomedical Engineering*, vol. 25/4, pp. 1014–1017, 2009.
85. V. Barbaro, P. Bartolini, G. Calcagnini, F. Censi, and A. Michelucci, “Measure of synchronisation of right atrial depolarisation wavefronts during atrial fibrillation,” *Med Biol Eng Comput*, vol. 40, pp. 56–62, 2002.
 86. V. Kremen, L. Lhotska, M. Macas, R. Cihak, V. Vancura, J. Kautzner, and D. Wichterle, “A new approach to automated assessment of fractionation of endocardial electrograms during atrial fibrillation,” *Physiol Meas*, vol. 29, pp. 1371–1381, 2008.
 87. E. Hofer, F. Keplinger, T. Thurner, T. Wiener, D. Sanchez-Quintana, V. Climent, and G. Plank, “A new floating sensor array to detect electric near fields of beating heart preparations,” *Biosens Bioelectron*, vol. 21, pp. 2232–2239, 2006.
 88. U. Richter, A. Bollmann, D. Husser, and M. Stridh, “Right atrial organization and wavefront analysis in atrial fibrillation,” *Med Biol Eng Comput*, vol. 47, pp. 1237–1246, 2009.
 89. J. Carlson, S. Santos, P. G. Platonov, O. K. Rasmussen, R. Johansson, and S. B. Olsson, “Left atrial conduction along the coronary sinus during ectopic atrial tachycardia and atrial fibrillation: a study using correlation function analysis,” *J Cardiovasc Electrophysiol*, vol. 14, pp. S148–53, 2003.
 90. D. U. J. Keller, F. M. Weber, G. Seemann, and O. Dössel, “Ranking the Influence of Tissue Conductivities on Forward-Calculated ECGs,” *IEEE Trans Biomed Eng*, vol. 57, pp. 1568–1576, 2010.
 91. C. F. Kay and H. P. Schwan, “Specific resistance of body tissues,” *Circ Res*, vol. 4, pp. 664–670, 1956.
 92. W. Kaufman and F. D. Johnston, “The electrical conductivity of the tissues near the heart and its bearing on the distribution of the cardiac action currents,” *Am Heart J*, vol. 26, pp. 42–54, 1943.
 93. H. C. Burger and J. B. van Milaan, “Measurements of the specific resistance of the human body to direct current,” *Acta Medica Scandinavica*, vol. 114, pp. 584–607, 1943.
 94. H. P. Schwan and C. F. Kay, “The conductivity of living tissues,” *Ann N Y Acad Sci*, vol. 65, pp. 1007–1013, 1957.
 95. S. Rush, J. A. Abildskov, and R. McFee, “Resistivity of body tissues at low frequencies,” *Circ Res*, vol. 12, pp. 40–50, 1963.
 96. B. R. Epstein and K. R. Foster, “Anisotropy in the dielectric properties of skeletal muscle,” *Med Biol Eng Comput*, vol. 21, pp. 51–55, 1983.
 97. R. Aaron, M. Huang, and C. A. Shiffman, “Anisotropy of human muscle via non-invasive impedance measurements,” *Phys Med Biol*, vol. 42, pp. 1245–1262, 1997.
 98. S. Grimnes and O. Martinsen, *Bioimpedance and bioelectricity basics*. San Diego, San Francisco, New York: Academic Press, 2008.
 99. M. W. Krueger, F. M. Weber, G. Seemann, and O. Dössel, “Semi-automatic segmentation of sinus node, Bachmann’s Bundle and Terminal Crest for patient specific atrial models,” in *IFMBE Proceedings World Congress on Medical Physics and Biomedical Engineering*, vol. 25/4, pp. 673–676, 2009.
 100. F. B. Sachse, M. Wolf, C. Werner, and K. Meyer-Waarden, “Extension of anatomical models of the human body: Three-dimensional interpolation of muscle fiber orientation based on restrictions,” *Journal of Computing and Information Technology*, vol. 6, pp. 95–101, 1998.
 101. I. Jolliffe, *Principal component analysis*. Berlin: Springer, 2002.
 102. Y. Zhang, D. H. Brooks, M. A. Franceschini, and D. A. Boas, “Eigenvector-based spatial filtering for reduction of physiological interference in diffuse optical imaging,” *J Biomed Opt*, vol. 10, p. 11014, 2005.
 103. R. L. Lux, A. K. Evans, M. J. Burgess, R. F. Wyatt, and J. A. Abildskov, “Redundancy reduction for improved display and analysis of body surface potential maps. I. Spatial compression,” *Circ Res*, vol. 49,

- pp. 186–196, 1981.
104. P. Langley, E. J. Bowers, and A. Murray, “Principal Component Analysis as a Tool for Analyzing Beat-to-Beat Changes in ECG Features: Application to ECG-Derived Respiration,” *IEEE Trans Biomed Eng*, vol. 57, pp. 821–829, 2010.
 105. V. Monasterio, P. Laguna, and J. P. Martinez, “Multilead analysis of T-wave alternans in the ECG using principal component analysis,” *IEEE Trans Biomed Eng*, vol. 56, pp. 1880–1890, 2009.
 106. S. Olmos, J. García, R. Jané, and P. Laguna, “ECG signal compression plus noise filtering with truncated orthogonal expansions,” *Signal Processing*, vol. 79, pp. 97–115, 1999.
 107. J. S. Paul, M. R. Reddy, and V. J. Kumar, “A transform domain SVD filter for suppression of muscle noise artefacts in exercise ECG’s,” *IEEE Trans Biomed Eng*, vol. 47, pp. 654–663, 2000.
 108. F. M. Weber, D. U. J. Keller, S. Bauer, G. Seemann, C. Lorenz, and O. Dössel, “Predicting Tissue Conductivity Influences on Body Surface Potentials - An Efficient Approach based on Principal Component Analysis,” *IEEE Trans Biomed Eng*, vol. 58, pp. 265–273, 2011.
 109. D. D. Streeter, *Handbook of Physiology: The Cardiovascular System*, vol. I, ch. Gross morphology and fiber geometry of the heart, pp. 61–112. American Physiology Society, 1979.
 110. K. H. W. J. ten Tusscher, D. Noble, P. J. Noble, and A. V. Panfilov, “A Model for Human Ventricular Tissue,” *Am J Physiol*, vol. 286, pp. H1573–H1589, 2004.
 111. S. Sicouri and C. Antzelevitch, “Distribution of M cells in the canine ventricle,” *J Cardiovasc Electrophysiol*, vol. 5, pp. 824–837, 1994.
 112. G. X. Yan, W. Shimizu, and C. Antzelevitch, “Characteristics and distribution of M cells in arterially perfused canine left ventricular wedge preparations,” *Circulation*, vol. 98, pp. 1921–1927, 1998.
 113. E. Drouin, F. Charpentier, C. Gauthier, K. Laurent, and H. L. Marec, “Electrophysiological characteristics of cells spanning the left ventricular wall of human heart: Evidence for the presence of M Cells,” *J Am Coll Cardiol*, vol. 26, pp. 185–192, 1995.
 114. N. Szentadrassy, T. Banyasz, T. Biro, G. Szabo, B. I. Toth, J. Magyar, J. Lazar, A. Varro, L. Kovacs, and P. P. Nanasi, “Apico-basal inhomogeneity in distribution of ion channels in canine and human ventricular myocardium,” *Cardiovasc Res*, vol. 65, pp. 851–860, 2005.
 115. P. Colli Franzone, L. F. Pavarino, S. Scacchi, and B. Taccardi, “Modeling ventricular repolarization: effects of transmural and apex-to-base heterogeneities in action potential durations,” *Math Biosci*, vol. 214, pp. 140–152, 2008.
 116. D. U. J. Keller, R. Kalayciyan, O. Dössel, and G. Seemann, “Fast Creation of Endocardial Stimulation Profiles for the Realistic Simulation of Body Surface ECGs,” in *IFMBE Proceedings World Congress on Medical Physics and Biomedical Engineering*, vol. 25/4, pp. 145–148, 2009.
 117. G. Golub and C. Reinsch, “Singular value decomposition and least squares solutions,” *Numerische Mathematik*, vol. 14, pp. 403–420, 1970.
 118. T. Chan, “An improved algorithm for computing the singular value decomposition,” *ACM Trans Math Softw*, vol. 8, pp. 84–88, 1982.
 119. <http://www.gnu.org/software/gsl/>.
 120. F. M. Weber, C. Schilling, G. Seemann, A. Luik, C. Schmitt, C. Lorenz, and O. Dössel, “Wave Direction and Conduction Velocity Analysis from Intracardiac Electrograms - A Single-Shot Technique,” *IEEE Trans Biomed Eng*, vol. 57, pp. 2394–2401, 2010.
 121. J. F. Kaiser, “On a simple algorithm to calculate the ‘energy’ of a signal,” *Acoustics, Speech, and Signal Processing, 1990. ICASSP-90., 1990 International Conference on*, pp. 381–384, 1990.

122. C. Schilling, M. P. Nguyen, A. Luik, C. Schmitt, and O. Dössel, "Non-Linear Energy Operator for the Analysis of Intracardiac Electrograms," in *IFMBE Proceedings World Congress on Medical Physics and Biomedical Engineering*, vol. 25/4, pp. 872–875, 2009.
123. H. Wendland, *Scattered data approximation*. Cambridge Univ Pr, 2005.
124. C. Chen, Y. Hon, and R. Schaback, "Scientific computing with radial basis functions," 2010.
125. G. Fasshauer, *Meshfree approximation methods with MATLAB*. Interdisciplinary mathematical sciences, New Jersey: World Scientific, 2007.
126. L. Murphy, "Linear feature detection and enhancement in noisy images via the Radon transform," *Pattern Recognit Lett*, vol. 4, no. 4, pp. 279–284, 1986.
127. Q. Zhang and I. Couloigner, "Accurate centerline detection and line width estimation of thick lines using the Radon transform," *IEEE Trans Image Process*, vol. 16, no. 2, pp. 310–316, 2007.
128. C. D. Werner, F. B. Sachse, and O. Dössel, "Applications of the Visible Man Dataset in Electrocardiology: Simulation of the Electrical Excitation Propagation," in *Proc. Second Users Conference of the National Library of Medicine's Visible Human Project*, pp. 69–79, 1998.
129. F. M. Weber, C. Schilling, D. Straub, G. Seemann, C. Lorenz, and O. Dössel, "Localizing ectopic foci in the pulmonary veins from intracardiac ECGs: a simulation study," in *IFMBE Proceedings World Congress on Medical Physics and Biomedical Engineering*, vol. 25/4, pp. 645–648, 2009.
130. F. M. Weber, C. Schilling, D. Straub, S. Gurm, G. Seemann, C. Lorenz, and O. Dössel, "Extracting clinically relevant circular mapping and coronary sinus catheter potentials from atrial simulations," in *Lecture Notes in Computer Science*, vol. 5528, pp. 30–38, 2009.
131. A. Kleber and Y. Rudy, "Basic mechanisms of cardiac impulse propagation and associated arrhythmias," *Physiol Rev*, vol. 84, pp. 431–488, 2004.
132. Y. Xie, A. Garfinkel, J. N. Weiss, and Z. Qu, "Cardiac alternans induced by fibroblast-myocyte coupling: mechanistic insights from computational models," *Am J Physiol Heart Circ Physiol*, vol. 297, pp. H775–84, 2009.
133. P. G. Postema, P. F. H. M. van Dessel, J. M. T. de Bakker, L. R. C. Dekker, A. C. Linnenbank, M. G. Hoogendijk, R. Coronel, J. G. P. Tijssen, A. A. M. Wilde, and H. L. Tan, "Slow and discontinuous conduction conspire in Brugada syndrome: a right ventricular mapping and stimulation study," *Circ Arrhythm Electrophysiol*, vol. 1, pp. 379–386, 2008.
134. E. de Lange and J. P. Kucera, "The transfer functions of cardiac tissue during stochastic pacing," *Biophys J*, vol. 96, pp. 294–311, 2009.
135. C. Weiß, *Basiswissen medizinische Statistik*. Springer-Lehrbuch, Heidelberg: Springer, 3rd ed., 2005.
136. J. Sachs, Lothar ; Hedderich, *Angewandte Statistik : Methodensammlung mit R*. Berlin: Springer, 13th ed., 2009.
137. J. Weese, J. Peters, I. Waechter, R. Kneser, H. Lehmann, O. Ecabert, H. Barschdorf, F. M. Weber, O. Doessel, and C. Lorenz, "The Generation of Patient-Specific Heart Models for Diagnosis and Interventions," in *Lecture Notes in Computer Science*, vol. 6364, pp. 25–35, 2010.
138. R. Hanna, "Model-based segmentation of the left atrium for electrophysiological simulations," Diploma thesis, 2009.
139. P. Neher, "Model-based segmentation of the right atrium for electrophysiological simulations," Diploma thesis, 2010.
140. A. S. Agha, C. A. Castillo, A. J. Castellanos, R. J. Myerburg, and M. P. Tessler, "Supernormal conduction in the human atria," *Circulation*, vol. 46, pp. 522–527, 1972.

141. P. Colli Franzone, L. F. Pavarino, and B. Taccardi, "Simulating patterns of excitation, repolarization and action potential duration with cardiac Bidomain and Monodomain models," *Math Biosci*, vol. 197, pp. 35–66, 2005.
142. B. J. Roth, "Electrical Conductivity Values Used with the Bidomain Model of Cardiac Tissue," *IEEE Trans Biomed Eng*, vol. 44, pp. 326–327, 1997.
143. R. Modre, M. Seger, G. Fischer, C. Hintermüller, D. Hayn, B. Pfeifer, F. Hanser, G. Schreier, and B. Tilg, "Cardiac Anisotropy: Is it Negligible Regarding Noninvasive Activation Time Imaging?," *IEEE Trans Biomed Eng*, vol. 53, pp. 569–580, 2006.
144. S. J. Walker and D. Kilpatrick, "Forward and inverse electrocardiographic calculations using resistor network models of the human torso," *Circ Res*, vol. 61, pp. 504–513, 1987.
145. P. C. Stanley, T. C. Pilkington, and M. N. Morrow, "The Effects of Thoracic Inhomogeneities on the Relationship Between Epicardial and Torso Potentials," *IEEE Trans Biomed Eng*, vol. Bme-33, pp. 273–284, 1986.
146. R. M. Gulrajani and G. E. Mailloux, "A simulation study of the effects of torso inhomogeneities on electrocardiographic potentials, using realistic heart and torso models," *Circ Res*, vol. 52, pp. 45–56, 1983.
147. Y. Rudy and R. Plonsey, "A comparison of volume conductor and source geometry effects on body surface and epicardial potentials," *Circ Res*, vol. 46, pp. 283–291, 1980.
148. Y. Rudy and R. Plonsey, "The eccentric spheres model as the basis for a study of the role of geometry and inhomogeneities in electrocardiography," *IEEE Trans Biomed Eng*, vol. 26, pp. 392–399, 1979.
149. A. van Oosterom and G. J. Huiskamp, "The effect of torso inhomogeneities on body surface potentials quantified using "tailored" geometry," *J Electrocardiol*, vol. 22, pp. 53–72, 1989.
150. S. Geneser, R. Kirby, and R. MacLeod, "Application of Stochastic Finite Element Methods to Study the Sensitivity of ECG Forward Modeling to Organ Conductivity," *IEEE Trans Biomed Eng*, vol. 55, pp. 31–40, 2008.
151. Z. Qu, A. Garfinkel, P. Chen, and J. Weiss, "Mechanisms of Discordant Alternans and Induction of Reentry in Simulated Cardiac Tissue," *Circulation*, vol. 102, pp. 1664–1670, 2000.
152. J. L. Smeets, M. A. Allesie, W. J. Lammers, F. I. Bonke, and J. Hollen, "The wavelength of the cardiac impulse and reentrant arrhythmias in isolated rabbit atrium. The role of heart rate, autonomic transmitters, temperature, and potassium," *Circ Res*, vol. 58, pp. 96–108, 1986.
153. E. de Lange and J. P. Kucera, "Alternans resonance and propagation block during supernormal conduction in cardiac tissue with decreased $[K(+)](o)$," *Biophys J*, vol. 98, pp. 1129–1138, 2010.
154. M. R. Franz, J. Schaefer, M. Schöttler, W. A. Seed, and M. I. M. Noble, "Electrical and mechanical restitution of the human heart at different rates of stimulation," *Circ Res*, vol. 53, pp. 815–822, 1983.
155. M. Franz, "The electrical restitution curve revisited: steep or flat slope - which is better?," *J Cardiovasc Electrophysiol*, vol. 14, p. 140, 2003.
156. E. Pueyo, Z. Husty, T. Hornyik, I. Baczko, P. Laguna, A. Varro, and B. Rodriguez, "Mechanisms of ventricular rate adaptation as a predictor of arrhythmic risk," *Am J Physiol Heart Circ Physiol*, vol. 298, pp. H1577–87, 2010.
157. E. J. Vigmond, V. Tsoi, Y. Yin, P. Page, and A. Vinet, "Estimating atrial action potential duration from electrograms," *IEEE Trans Biomed Eng*, vol. 56, pp. 1546–1555, 2009.
158. M. Burdumy, F. M. Weber, A. Luik, R. Hanna, M. W. Krueger, C. Schilling, H. Barschdorf, C. Lorenz, G. Seemann, C. Schmitt, and O. Dössel, "Comparing Measured and Simulated Incidence Directions in the Left Atrium - A Workflow for Model Personalization and Validation," in *Biomedizinische Technik /*

Biomedical Engineering (Proceedings BMT2010), vol. 55, pp. 50–53, 2010.

159. S. Ho, R. Anderson, and D. Sánchez-Quintana, “Atrial structure and fibres: morphologic based of atrial conduction,” *Cardiovasc Res*, vol. 54, pp. 325–336, 2002.
160. F. Saremi and S. Krishnan, “Cardiac conduction system: anatomic landmarks relevant to interventional electrophysiologic techniques demonstrated with 64-detector CT,” *Radiographics*, vol. 27, pp. 1539–65, 2007.
161. F. Saremi, S. Channal, S. Krishnan, S. Gurudevan, J. Narula, and A. Abolhoda, “Bachmann Bundle and its arterial supply: imaging with multidetector CT—implications for interatrial conduction abnormalities and arrhythmias,” *Radiology*, vol. 248, pp. 447–457, 2008.
162. M. W. Krueger, V. Schmidt, C. Tobón, F. M. Weber, C. Lorenz, D. U. J. Keller, H. Barschdorf, M. Burdumy, P. Neher, G. Plank, K. Rhode, G. Seemann, D. Sanchez-Quintana, J. Saiz, R. Razavi, and O. Dössel, “Modeling Atrial Fiber Orientation in Patient-Specific Geometries: A Semi-Automatic Rule-Based Approach,” *Lecture Notes in Computer Science (FIMH 2011) accepted*, 2011.

List of Figures

2.1	The human heart (posterior view).....	7
2.2	Cell membrane (simplified)	8
2.3	Action potential and time-dependent conductivities of ion channels ...	9
2.4	Standard ECG (P, QRS, T)	10
2.5	Body Surface Potential Map acquisition	11
2.6	Interatrial bridges between right and left atrium	12
2.7	Mechanisms of macroscopic reentries	13
2.8	Mechanisms of AF initiation and maintenance	14
2.9	Mechanisms of atrial remodeling	15
2.10	Intracardiac mapping catheters: Inquiry Optima, Pentaray and AFocus	16
2.11	Example of complex fractionated electrogram.....	17
3.1	Visible Man (VM) data set.	20
3.2	Heart segmentation with active-shape approach	21
3.3	Hodgkin-Huxley and Courtemanche-Ramirez-Nattel cell models	22
3.4	Currents and time-course of Minimal Model	24
3.5	Principle function of a cellular automaton	27
4.1	Parameters for fast inward current (Na) in Minimal Model	34
4.2	Parameters for slow outward current (K) in Minimal Model	34
4.3	Parameters for slow inward current (Ca) in Minimal Model	35
4.4	Patch simulation with crossfield stimulus (schematic)	38
5.1	Tetrahedron model of the VM torso with BSPM electrode locations ..	41
5.2	Example for shifted PCA scores in conductivity analysis.....	48
5.3	PCA reconstruction and validation for single tissue conductivities	50
6.1	Intracardiac data analysis (non-linear energy operator / cosine-pattern)	54

6.2	Simulation and analysis of intracardiac EGMs in a tissue patch	56
6.3	Analysis techniques for CS signals	63
8.1	Minimal Model adaptation results for physiological case	80
8.2	Minimal Model adaptation results for remodeling case	81
8.3	2D patch simulations for remodeling case with spiral wave evolution	82
9.1	Shifted PCA scores for first eigenvectors of atrial and ventricular input data	93
9.2	Example for PCA reconstruction of combined conductivity variations	96
9.3	ECG confidence intervals derived from PCA method	97
10.1	Results of cosine fit stability analysis	100
10.2	Reconstruction of two colliding wave fronts (simulated) using RBF interpolation	102
10.3	Reconstruction of an ectopic focus using RBF interpolation	102
10.4	Simulation of circular mapping catheter in the Visible Man LA roof with different PV stimuli	104
10.5	Cosine fit analysis of data from patient 1, segments 1a and 1b	105
10.6	Cosine fit analysis of data from patient 2, segments 2a (alternating pattern)	106
10.7	Cosine fit analysis of data from patient 2, segments 2c (ectopic foci)	107
10.8	RBF analysis of data from patient 3, segment 3b (wavefront collisions)	109
10.9	Cosine fit analysis of data from patient 4, segments 4a and 4b	111
10.10	RBF analysis of data from patient 7, segment 7a (AFocusII measurements)	114
10.11	CV restitution analysis: Example electrograms for pacing at 500 and 300 ms	116
10.12	Restitution curves for local and global CV from patients 1 and 2	117
10.13	Restitution curves for local and global CV from patients 3 and 4	117
11.1	Personalized simulation for patient 1	127
11.2	Personalized simulation for patient 2	127
11.3	Personalized simulation for patient 3	128
11.4	Personalized simulation for patient 4	129

List of Tables

3.1	Parameter sets for the MM for ventricular cells as supplied in [50].	23
6.1	Common radial basis functions and their properties [124].	58
6.2	Overview over patient data	69
8.1	Parameter sets for the MM after adaptation to the CRN model for physiological (Phys) and remodeling (Rem) case.	81
9.1	Lower and upper tissue conductivity boundaries	86
9.2	Results of the conductivity sensitivity analysis for atrial signals	87
9.3	Results of the conductivity uncertainty analysis for atrial signals	88
9.4	Error (RMSE or CC based) of possible torso simplifications	88
9.5	Ratio between first and second PCA eigenvalue	92
9.6	RMSE (μV) of PCA reconstruction when using <i>exact</i> and <i>interpolated</i> scores	94
9.7	RMSE (μV) of PCA reconstruction for combined conductivity variations	95
10.1	Cosine-fit results for simulated circular catheter on LA roof.	103
10.2	Results of patient data analysis (cosine fit and CS analysis) for patients 1 to 3.	112
10.3	Results of patient data analysis (cosine fit and CS analysis) for patients 4 to 6.	113
10.4	CV restitution analysis results for different pacing sequences.	115
11.1	Comparison between simulated values and clinical measurements.	126

List of Publications and Supervised Theses

Journal Papers

1. **F. M. Weber**, C. Schilling, G. Seemann, A. Luik, C. Schmitt, C. Lorenz, and O. Dössel, “Wave Direction and Conduction Velocity Analysis from Intracardiac Electrograms - A Single-Shot Technique,” *IEEE Transactions on Biomedical Engineering*, vol. 57, pp. 2394–2401, 2010.
2. **F. M. Weber**, D. U. J. Keller, S. Bauer, G. Seemann, C. Lorenz, and O. Dössel, “Predicting Tissue Conductivity Influences on Body Surface Potentials - An Efficient Approach based on Principal Component Analysis,” *IEEE Transactions on Biomedical Engineering*, vol. 58, pp. 265–273, 2011.
3. **F. M. Weber**, A. Luik, C. Schilling, G. Seemann, M. W. Krueger, C. Lorenz, C. Schmitt, and O. Dössel, “Conduction Velocity Restitution of the Human Atrium in Patients with Atrial Fibrillation,” *in preparation*.
4. D. U. J. Keller, **F. M. Weber**, G. Seemann, and O. Dössel, “Ranking the Influence of Tissue Conductivities on Forward-Calculated ECGs,” *IEEE Transactions on Biomedical Engineering*, vol. 57, pp. 1568–1576, 2010.
5. G. Seemann, D. U. J. Keller, M. W. Krueger, **F. M. Weber**, M. Wilhelms, and O. Dössel, “Electrophysiological modeling for cardiology: methods and potential applications,” *Information Technology*, vol. 52, pp. 242–249, 2010.
6. M. W. Krueger, S. Severi, K. Rhode, S. Genovesi, **F. M. Weber**, A. Vincenti, P. Fabbrini, G. Seemann, R. Razavi, and O. Dössel, “Alterations of Atrial Electrophysiology related to Hemodialysis Session: Insights from a Multi-Scale Computer Model,” *Journal of Electrocardiology*, vol. 44, pp. 176–183, 2011.

Conference Contributions

1. **F. M. Weber**, C. Schilling, A. Luik, M. W. Krueger, G. Seemann, C. Lorenz, C. Schmitt, and O. Dössel, “Quantitative determination of wave direction and conduction velocity in the human atrium from intracardiac electrograms,” in *Journal of Electrocardiology (Proc. ICE 2010)*, vol. 44, p. e14, 2011. *Young Investigators Award Finalist*.
2. **F. M. Weber**, C. Schilling, D. Straub, S. Gurm, G. Seemann, C. Lorenz, and O. Dössel, “Extracting clinically relevant circular mapping and coronary sinus catheter potentials from atrial simulations,” in *Lecture Notes in Computer Science*, vol. 5528, pp. 30–38, 2009.
3. **F. M. Weber**, C. Schilling, D. Straub, G. Seemann, C. Lorenz, and O. Dössel, “Localizing ectopic foci in the pulmonary veins from intracardiac ECGs: a simulation study,” in *IFMBE Proceedings World Congress on Medical Physics and Biomedical Engineering*, vol. 25/4, pp. 645–648, 2009.
4. **F. M. Weber**, S. Lurz, D. U. J. Keller, D. L. Weiss, G. Seemann, C. Lorenz, and O. Dössel, “Adaptation of a minimal four-state cell model for reproducing atrial excitation properties,” in *Proc. Computers in Cardiology*, pp. 61–64, 2008.
5. M. Burdumy, **F. M. Weber**, A. Luik, R. Hanna, M. W. Krueger, C. Schilling, H. Barschdorf, C. Lorenz, G. Seemann, C. Schmitt, and O. Dössel, “Comparing Measured and Simulated Incidence Directions in the Left Atrium - A Workflow for Model Personalization and Validation,” in *Biomedizinische Technik / Biomedical Engineering (Proceedings BMT 2010)*, vol. 55 (s1), pp. 50–53, 2010. *8th prize in student competition out of over 100 participants*.
6. S. Bauer, D. U. J. Keller, **F. M. Weber**, P. Tri Dung, G. Seemann, and O. Dössel, “How do tissue conductivities impact on forward-calculated ECGs? An efficient prediction based on principal component analysis,” in *IFMBE Proceedings World Congress on Medical Physics and Biomedical Engineering*, vol. 25/4, pp. 641–644, 2009.
7. M. W. Krueger, **F. M. Weber**, G. Seemann, and O. Dössel, “Semi-automatic segmentation of sinus node, Bachmann’s Bundle and Terminal Crest for patient specific atrial models,” in *IFMBE Proceedings World Congress on Medical Physics and Biomedical Engineering*, vol. 25/4, pp. 673–676, 2009.
8. M. W. Krueger, K. Rhode, **F. M. Weber**, D. U. J. Keller, D. Caulfield, G. Seemann, B. R. Knowles, R. Razavi, and O. Dössel, “Patient-Specific Volumetric Atrial Models with Electrophysiological Components: A Comparison of Simula-

-
- tions and Measurements,” in *Biomedizinische Technik / Biomedical Engineering (Proceedings BMT2010)*, vol. 55 (s1), pp. 54–57, 2010.
9. W. H. W. Schulze, M. W. Krueger, Y. Jiang, K. Rhode, **F. M. Weber**, D. Caulfield, B. R. Knowles, R. Razavi, and O. Dössel, “Localization of the Atrial Excitation Origin by Reconstruction of Time-Integrated Transmembrane Voltages,” in *Biomedizinische Technik / Biomedical Engineering (Proceedings BMT2010)*, vol. 55 (s1), pp. 54–57, 2010.
 10. M. W. Krueger, S. Severi, G. Seemann, **F. M. Weber**, S. Genovesi, A. Vincenti, P. Fabbrini, and O. Dössel, “Alterations of atrial electrophysiology after hemodialysis session: a simulation study in volumetric atrial tissues,” in *Proceedings International Congress on Electrocardiology 2010*, p. 4, 2010.
 11. J. Weese, J. Peters, I. Waechter, R. Kneser, H. Lehmann, O. Ecabert, H. Barschdorf, **F. M. Weber**, O. Dössel, and C. Lorenz, “The Generation of Patient-Specific Heart Models for Diagnosis and Interventions,” in *Lecture Notes in Computer Science*, vol. 6364, pp. 25–35, 2010.
 12. P. Neher, H. Barschdorf, S. Dries, **F. M. Weber**, M. W. Krueger, O. Dössel, and C. Lorenz, “Automatic Segmentation of Cardiac CTs - Personalized Atrial Models Augmented with Electrophysiological Structures,” in *Lecture Notes in Computer Sciences (FIMH 2011)*, *accepted*, 2011.
 13. R. Hanna, H. Barschdorf, T. Klinder, **F. M. Weber**, M. W. Krueger, O. Dössel, C. Lorenz, “A Hybrid Method for Automatic Anatomical Variant Detection and Segmentation,” in *Lecture Notes in Computer Sciences (FIMH 2011)*, *accepted*, 2011.
 14. M. W. Krueger, V. Schmidt, C. Tobón, **F. M. Weber**, C. Lorenz, D. U. J. Keller, H. Barschdorf, M. Burdumy, P. Neher, G. Plank, K. Rhode, G. Seemann, D. Sanchez-Quintana, J. Saiz, R. Razavi, and O. Dössel, “Modeling Atrial Fiber Orientation in Patient-Specific Geometries: A Semi-Automatic Rule-Based Approach,” *Lecture Notes in Computer Science (FIMH 2011)*, *accepted*, 2011.

Supervised Theses

1. Michael Burdumy, “Personalized Simulation and Analysis of Intracardiac Electrograms of the Left Atrium”, Diploma thesis, 2010
2. Martin Bauer, “Simulation von chaotischen Erregungsmustern bei Vorhofflimmern mit einem minimalen Zellmodell”, Bachelor’s thesis, 2010
3. Martin Bauer, “Erstellung einer Anpassungsumgebung zur Angleichung des Minimal Models an verschiedene Zellmodelle”, Student project, 2010
4. Stefan Bauer, “Efficient Reconstruction of BSPMs and Optimization of Multiple Tissue Conductivities”, Diploma thesis, 2009
5. Dorothee Straub, “Simulation abgeleiteter Potentiale auf der Körper- und Herzoberfläche bei variierten Modellparametern”, Student project (Studienarbeit), 2008
6. Sandeep Gurm, “Simulation of Intracardiac Potentials under Atrial Flutter and Fibrillation”, Student project, 2008
7. Pham Tri Dung, “The impact of distinctive organ conductivities on the solution of the forward problem of electrocardiography”, Master’s thesis, 2008
8. Peter Neher, “Model-based Segmentation of the Right Atrium for Electrophysiological Simulations”, Diploma thesis (external), 2010

Karlsruhe Transactions on Biomedical Engineering (ISSN 1864-5933)

Karlsruhe Institute of Technology / Institute of Biomedical Engineering (Ed.)

Die Bände sind unter www.ksp.kit.edu als PDF frei verfügbar oder als Druckausgabe bestellbar.

- Band 2** Matthias Reumann
Computer assisted optimisation on non-pharmacological treatment of congestive heart failure and supraventricular arrhythmia. 2007
ISBN 978-3-86644-122-4
- Band 3** Antoun Khawaja
Automatic ECG analysis using principal component analysis and wavelet transformation. 2007
ISBN 978-3-86644-132-3
- Band 4** Dmytro Farina
Forward and inverse problems of electrocardiography : clinical investigations. 2008
ISBN 978-3-86644-219-1
- Band 5** Jörn Thiele
Optische und mechanische Messungen von elektrophysiologischen Vorgängen im Myokardgewebe. 2008
ISBN 978-3-86644-240-5
- Band 6** Raz Miri
Computer assisted optimization of cardiac resynchronization therapy. 2009
ISBN 978-3-86644-360-0
- Band 7** Frank Kreuder
2D-3D-Registrierung mit Parameterentkopplung für die Patiententlagerung in der Strahlentherapie. 2009
ISBN 978-3-86644-376-1
- Band 8** Daniel Unholtz
Optische Oberflächensignalmessung mit Mikrolinsen-Detektoren für die Kleintierbildgebung. 2009
ISBN 978-3-86644-423-2
- Band 9** Yuan Jiang
Solving the inverse problem of electrocardiography in a realistic environment. 2010
ISBN 978-3-86644-486-7

Karlsruhe Transactions on Biomedical Engineering (ISSN 1864-5933)

- Band 10** Sebastian Seitz
Magnetic Resonance Imaging on Patients with Implanted Cardiac Pacemakers. 2011
ISBN 978-3-86644-610-6
- Band 11** Tobias Voigt
Quantitative MR Imaging of the Electric Properties and Local SAR based on Improved RF Transmit Field Mapping. 2011
ISBN 978-3-86644-598-7
- Band 12** Frank Michael Weber
Personalizing Simulations of the Human Atria: Intracardiac Measurements, Tissue Conductivities, and Cellular Electrophysiology. 2011
ISBN 978-3-86644-646-5

Can computer models of the heart be personalized to gain better understanding of atrial arrhythmias? For example, they might then improve treatment of atrial fibrillation, the most common cardiac arrhythmia.

This thesis addresses major challenges of heart model personalization. Analysis techniques for clinical intracardiac electrograms are developed. They determine wave direction and conduction velocity from single beats. Then, electrophysiological measurements are reproduced in the simulation (in-silico) to compare excitation conduction and validate the models.

Further investigations describe how to deal with uncertainties in tissue conductivities within the torso, which impact on simulated surface ECGs. Finally, a minimal model of single cardiac myocytes is adapted to atrial properties.

The presented results make personalized cardiac models a promising technique to improve understanding and treatment of atrial arrhythmias.

